UNIVERSITY OF TWENTE.

Design and fabrication of a bulk micromachined accelerometer for geophysical applications

HARMEN DROOGENDIJK BSC

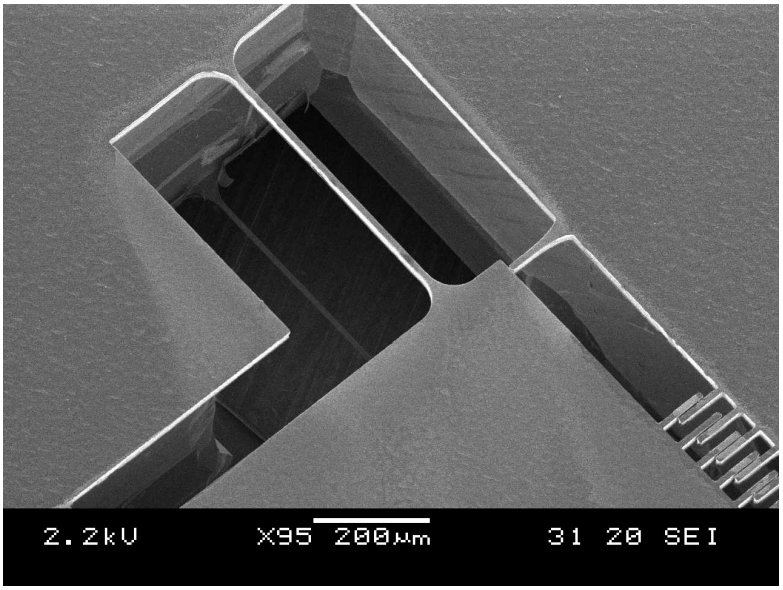

Electrical Engineering – Master Thesis Project (121121)

Graduation committee

dr. ir. R.J. Wiegerink (supervisor)
prof. dr. ir. G.J.M. Krijnen
dr. ir. J. Flokstra
ing. J.W. Berenschot
dr. ir. M. Dijkstra

Enschede, September 16th 2009

Abstract

Using gravitational acceleration (gravity) or its gradient, geophysicists are capable of determining the presence of gas and oil. These gravitational effects are often very small compared to earth's gravity (typically less than 1:100.000), making measurements rather difficult.

Although nowadays measurement systems are present for gravity (gradient) sensing, the use of MEMS (Micro Electro Mechanical Systems) is quite rare within this field. Realization of such a sensor in MEMS would offer various benefits. These possibilities are investigated, resulting in the design and fabrication of a bulk micromachined accelerometer for geophysical applications.

Before designing this accelerometer, first gravity and its gradient itself are investigated. Most commonly used measurement techniques are determined, resolutions are researched and the applicability within MEMS is summarized.

From these results a very sensitive MEMS accelerometer is designed and several effects, restraints, read-out mechanisms and optimization methods are investigated. Using bulk micromachining and sidewall coating technology, a process is developed to fabricate such a sensor. Several sensors for geophysical applications are fabricated, leading to important information regarding the fabrication process.

Despite the fabrication of the sensors, the process is not robust enough for characterization of the devices. However, using numerical analysis combined with computer simulations, several predictions about the performance of such a MEMS sensor is given, which gives important results regarding the use and opportunities of MEMS in the gravitational field.

Acknowledgments

"The best way to measure gravity is to drop an object in space and watch its trajectory." – Dr. Michael Watkins (NASA)

The present report is the result of my master thesis project, which I carried out at the chair for Transducers Science and Technology (TST), department of Electrical Engineering at the University of Twente. TST is a chair where research is done focused on the design and fabrication of Micro Electro Mechanical Systems (MEMS).

For eight months a lot of work has been done, designs were made and investigated, practical work in the MESA$^+$ cleanroom has been carried out and more for the design and fabrication of a bulk micromachined accelerometer for geophysical applications. Therefore, I pay gratitude to some people for their support, aid and knowledge for the past time.

First, I would like to thank my supervisor Remco Wiegerink, who came to me with the assignment about MEMS in the gravitational field. Thanks for the fruitful discussions, conversations and advises on several fronts.

Second, thanks to Erwin Berenschot and Meint de Boer, who are both cleanroom technicians at the TST chair. With their experience and knowledge it was possible to determine a feasible solution for the designed accelerometer and making it also possible to fabricate it in the MESA$^+$ cleanroom.

Next, thanks to Jaap Flokstra of the Low Temperature Division chair from the department of Applied Physics. Every Wednesday we had a meeting about the 'big' gravitational project, where my research was part of. This lead to interesting ideas and a useful visit to Shell and Fugro, for future (commercial) interest regarding the proposed MEMS sensor.

Gratitude is also given to Gijs Krijnen and Marcel Dijkstra. Both are members of the graduation committee and the results from the meetings with them were useful and enriching the product of research.

I would also like to thank my colleagues (especially Robert Brookhuis and Hylco de Boer) for the pleasant corporation, their involvement and their advises with respect to me and my work.

Finally, I should thank my wife Klaske for her attention during my master thesis project and for stimulating me every time to make the most out of it.

Enschede, September 2009

Harmen Droogendijk BSc

Contents

List of Symbols

a	acceleration (m/s^2)
D	diameter (m)
E	Young's modulus (Pa)
E	energy (J)
F	force (N)
f	frequency (Hz)
G	gravitational constant (Nm^2/kg^2)
g	gravitational acceleration (m/s^2)
I	moment of inertia ($kg{\cdot}m^2$)
I	second moment of inertia (m^4)
K	spring constant (N/m)
L	length (m)
M	moment (N·m)
m	mass (kg)
r	radius (m)
t	time (t)
u	voltage (V)
v	velocity (m)
x	Cartesian coordinate (m)
y	Cartesian coordinate (m)
z	Cartesian coordinate (m)

Greek letters

Γ	gravitational potential (m^2/s^2)
γ	viscous damping coefficient (kg/s)
δ	deflection (m)
ϵ	strain (m/m)
λ	curvature shortening (m)
ν	Poisson's ratio
σ	stress (Pa)
ω	angular frequency (rad/s)

Glossary

ADC	Analog-to-Digital Converter
CAD	Computer-Aided Design
DAC	Digital-to-Analog Converter
DRIE	Deep Reactive Ion Etching
DSP	Double Side Polished
FEM	Finite Element Method
FoM	Figure of Merit
IC	Integrated Circuit
LOCOS	Local Oxidation of Silicon
LPCVD	Low Pressure Chemical Vapor Deposition
MEMS	Micro Electro Mechanical System
OSP	One Side Polished
PWM	Pulse Width Modulation
SEM	Scanning Electron Microscope
SiRN	Silicon Rich Nitride
SNR	Signal-to-Noise Ratio
TEOS	TetraEthyl OrthoSilicate
TMAH	TetraMethylAmmonium Hydroxide
TNEA	Total Noise Equivalent Acceleration

Chapter 1

Introduction

Before starting with the design and fabrication of a bulk micromachined accelerometer for geophysical applications, first an introduction is given about this work. A brief summary is given about gravity (gradient) measurements and the need for a Micro Electro Mechanical System (MEMS) is explained. Next, the objectives and approach are given, together with a short outline of the thesis.

1.1 Geophysical applications

In the world of geophysics gravitational[1] acceleration (the acceleration due to the gravitational attraction of massive bodies) is often used to characterize properties for the interest of geologists. Especially when the change in gravitational acceleration over a unit distance is used, also called gravity gradiometry, the presence of oil and gas can be detected, by determining the density of a specific spot on a certain distance [1].

The technique of gravity gradiometry was previously used by the U.S. Navy for bathymetry (measurement of ocean depth) and to determine whether there were submerged units in their neighborhood by measuring differences in density within a water column [2].

These gravitational effects are typically very small compared to earth's gravity, making it difficult to measure them.

1.2 Problem definition

Although today several (commercial) gravity (gradient) sensors are available, most of them are either expensive, weigh a lot and/or are very large. Especially the more accurate sensors have sizes of several cubic decimeter and are quite expensive.

When a sensor for gravity gradient measurements could be designed and fabricated using Micro Electro Mechanical Systems (MEMS) technology, the resulting sensor would not only be (very) small and low-weight, but also relative cheap when a lot of them are produced simultaneously. Till today no such a MEMS sensor has been realized.

[1] *Gravitation* is a general term describing the phenomenon of attracting forces between bodies, *gravity* is normally considered as earth's gravity with acceleration g (9.81 m/s^2).

Therefore, when such a MEMS device can be realized yielding comparable resolutions with respect to available systems for gravity (gradient) sensing, this would be a breakthrough in miniaturization of gravity (gradient) measurement systems.

1.3 Introduction to MEMS

A Micro-Electro-Mechanical System (MEMS) is the integration of mechanical elements, sensors, actuators, and electronics on a common silicon substrate through microfabrication technology. Though microfabrication is used a lot for integrated circuit (IC) technology, it can be also used for fabrication of interesting miniature devices like accelerometers (see figure 1.1), micromirrors and lab-on-a-chip systems. Using microfabrication technology for MEMS purposes is also called micromachining, since it mainly consists of creating mechanical and electromechanical devices.

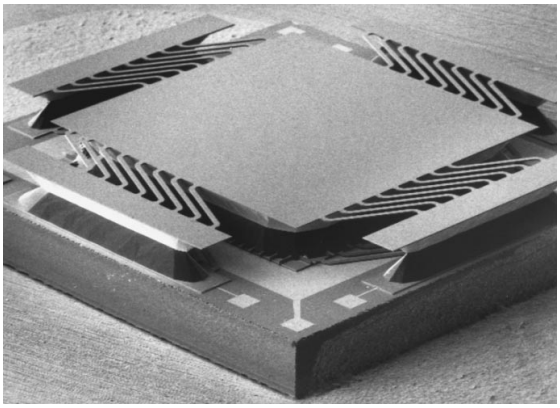

Figure 1.1: *Example of a MEMS accelerometer [3].*

1.4 Objective

The objective of this work was to design and fabricate a highly sensitive MEMS accelerometer for geophysical applications. Because in MEMS it is common to measure accelerations with a mass-spring system, this principle will be used as starting point for the design. But, since gravitational accelerations are very small compared to the range which is common for existing MEMS accelerometers [4], it is a challenge to realize such a sensor within MEMS.

Because performance of MEMS sensors for use within the gravitational field is slightly known, the capabilities of MEMS as a technology for this field will be investigated, to determine which aspects might limit the use of this technology.

1.4.1 Requirements

Since a very sensitive MEMS accelerometer requires proper designing, requirements are necessary to develop a proper sensor for use within the gravitational field, which are given in table 1.1. More detail about these requirements is given later on.

Table 1.1: *Requirements for the MEMS accelerometer.*

Quantity	Specification
Field of operation	Earth
Sensitivity	1 nm/mgal
Read-out	Capacitive
Force feedback	Optional
Design symmetry	Over three axes

1.5 Approach

First, all existing techniques for measuring gravity and/or its gradient are investigated, in order to determine if there are also other techniques available for gravity measurements using MEMS technology. Next, a design should be made with the best possible specifications, within the limits of fabrication.

The sensor itself should be realized within the MESA$^+$ cleanroom, in order to prove that such a sensor can be fabricated using the chosen technology.

In addition, also aspects like robustness, restraints, read-out mechanisms, characterization setup and using feedback are investigated to get a good view about designing a sensor with a geophysical purpose.

1.6 Outline

In chapter 2 the known techniques within the field of gravity (gradient) measurements are treated. Each method is explained and the advantages and disadvantages are given. The most suitable method is determined in chapter 3. There, also the analysis of the proposed system is performed and several important effects are investigated.

The associated expected behavior of the system and finite element simulations are given in chapter 4, in order to get also a good quantitative understanding of the design. The chosen technology and fabrication process are discussed in chapter 5.

Results from the fabrication are given in chapter 6. Finally, conclusions are drawn and recommendations are given in chapter 7.

References

[1] W. Jacoby and P. L. Smilde. *Gravity Interpretation*. Springer Verlag, Berlin, 2009.

[2] M. Nabighian, M. Anders, V. Grauch, R. Hansen, R. LaFehr, Y. Li, W. Pearson, J. Peirce, J. Phillips, and M. Ruder. "Historical development of the gravity method in exploration". *Geophysics*, **70**(6):63–86, 2005. 75th Anniversary.

[3] J. Bernstein, R. Miller, W. Kelley, and P. Ward. "Low-noise MEMS vibration sensor for geophysical applications". *Journal of Microelectromechanical Systems*, **8**(4):433–438, December 1999.

[4] X. Jiang, F. Wang, M. Kraft, and B. E. Boser. "An Integrated Surface Micromachined Capacitive Lateral Accelerometer with $2\mu G/\sqrt{Hz}$ Resolution". In *Solid-State Sensor, Actuator and Microsystems Workshop*, Hilton Head Island, South Carolina, June 2–6 2002.

Chapter 2

Gravitation

Before a gravity (gradient) sensor with MEMS technology can be designed and fabricated, first gravity itself has to be investigated. Using Newton's law and looking at the gravitational field, gravity can be understood and which quantities of it can be measured. Further on, several techniques for measuring this gravity and/or its gradient will be discussed.

2.1 Introduction

From basic physics every mass is attracting other masses and is also attracted by other masses, which is illustrated in figure 2.1. This phenomenon is described with Newton's law of universal gravitation, wherein F_1 and F_2 are the forces exerted on the masses m_1 and m_2, G is the gravitational constant ($6.673 \cdot 10^{-11}$ Nm^2/kg^2) and r is the distance between the two masses [1].

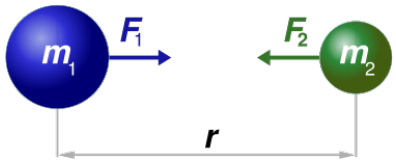

Figure 2.1: *Newton's law of universal gravitation.*

$$|\boldsymbol{F_1}| = |\boldsymbol{F_2}| = G\frac{m_1 m_2}{|\boldsymbol{r}|^2} \tag{2.1}$$

When this equation is applied on earth and a mass m_t on its surface, the expression can be arranged to

$$|\boldsymbol{F_e}| = |\boldsymbol{F_t}| = G\frac{m_e m_t}{|\boldsymbol{r_e}|^2} \tag{2.2}$$

where m_e is the mass of the earth ($5.9736 \cdot 10^{24}$ kg), r_e is the inner radius of the earth (6371 km). Using Newton's second law of motion, an expression for the gravitational

acceleration g can be determined. As might be expected, the value of g on earth's surface is about 9.81 m/s^2.

$$|\boldsymbol{F_t}| = m_t|\boldsymbol{g}| \tag{2.3}$$

which yields

$$|\boldsymbol{g}| = G\frac{m_e}{|\boldsymbol{r_e}|^2} \approx 9.81 \text{ m/s}^2 \tag{2.4}$$

As can be seen in equation 2.3, this is just a simple representation of two point masses. In reality the universe consists of nearly infinite (very small) point masses. Therefore, the gravitational potential field Γ is introduced, which describes universal gravitation using vector representation for the gravitational acceleration $\boldsymbol{g}$ for a mass m with a force $\boldsymbol{F}$ exerted on it.

$$\boldsymbol{g} = \frac{\boldsymbol{F}}{m} \tag{2.5}$$

When the gravitational field $\mathbf{g}$ is expanded into cartesian coordinates with associated components, the following equation is obtained, where Γ is the gravitational potential.

$$\boldsymbol{g} = -\nabla\Gamma = \begin{bmatrix} g_x \\ g_y \\ g_z \end{bmatrix} \tag{2.6}$$

With this expression the gravitational acceleration $\mathbf{g}$ on a certain position can be determined. When one would like to know how the gravity field changes, a gravity gradient tensor can be used (also called Eötvös tensor) [2].

$$-\nabla\boldsymbol{g} = \begin{bmatrix} \Gamma_{xx} & \Gamma_{xy} & \Gamma_{xz} \\ \Gamma_{yx} & \Gamma_{yy} & \Gamma_{yz} \\ \Gamma_{zx} & \Gamma_{zy} & \Gamma_{zz} \end{bmatrix} \tag{2.7}$$

In free space, this tensor consists eventually of five independent elements, since in that case Laplace's equation holds

$$\nabla^2\Gamma = \Gamma_{xx} + \Gamma_{yy} + \Gamma_{zz} = 0 \tag{2.8}$$

and three pairs of the nine elements are symmetrically equal, by Clairaut's theorem [3].

$$\Gamma_{xy} = \Gamma_{yx} \qquad \Gamma_{xz} = \Gamma_{zx} \qquad \Gamma_{yz} = \Gamma_{zy} \tag{2.9}$$

2.2 Gravimetry

More than eighty years ago exploration of the Earth using gravity techniques began. In the beginning this was mainly done for oil and gas exploration [4], but nowadays the techniques are also used for various other geophysical purposes. When talking about measuring

gravity, or measuring the gravitational field, mostly gravity anomalies are treated. Measuring these anomalies, which often are smaller than 1 mgal[1], can be done using several gravimeters. For example, the gravimeter of Romberg and LaCoste is capable of measuring gravity with a resolution of about 1 μgal [5].

For measurements below Earth's surface, in a borehole for example, one should determine the gravity in z-direction (towards the centre of the Earth). This can be explained using Gauss' law for gravity [6], because gravitational forces can be treated analogeous to electrical forces.

Taking a closed volume, there are gravitational forces present instead of electrical forces and instead of considering point charges point masses are used. This will lead to the expression for the gravitational (instead of electrical) field in equation 2.10, where $\boldsymbol{g}$ is the gravitational acceleration, G is the gravitational constant and M is the enclosed mass by a surface S.

$$\iint_S \boldsymbol{g} \cdot d\boldsymbol{S} = -4\pi GM \tag{2.10}$$

Also the differential form of it can be derived, where ρ is the density of the material.

$$\nabla \cdot \boldsymbol{g} = \operatorname{div} \boldsymbol{g} = -4\pi G\rho \tag{2.11}$$

Notice that in this case Laplace's equation (2.8) does not hold. Instead, Poisson's equation is needed, because it is no free space anymore.

$$\nabla^2 \Gamma = \operatorname{div} \nabla \Gamma = \Gamma_{xx} + \Gamma_{yy} + \Gamma_{zz} = 4\pi G\rho \tag{2.12}$$

When an infinite slab with small thickness is considered, an expression for the gravity g_z in the z-direction can be derived [5]. Considering Gauss' law, it seems that in this case only a gradient can occur in the z-direction, so

$$\frac{\partial g_z}{\partial z} = -4\pi G\rho \tag{2.13}$$

For small thicknesses this can be approximated for the change in gravity Δg_z over the slab.

$$\Delta g_z = -4\pi G\rho \Delta z \tag{2.14}$$

This expression can be used for density measurements, since rearranging this expression gives

$$\rho = \frac{-1}{4\pi G} \frac{\Delta g_z}{\Delta z} \tag{2.15}$$

Since geophysicists are eventually interested in the density ρ, this technique is used often for geophysical purposes. Using density, or the change in it, they can give statements about the composition of the soil.

[1] 1 gal = 1 cm/s^2.

Although it looks like that a gradient is measured in equation 2.15, in practice a gravimeter is used, measuring the gravity g_z on two different depths, resulting in a change in gravity Δg_z due to a change in depth Δz.

2.3 Gravity gradiometry

In addition of measuring the value of gravitation at a certain position, it is also possible to look at the *change* of gravitation at a certain position. In other words, it is interesting to determine the gravity gradient Γ. Current systems use the approximation of the gradient by measuring the gravity at two positions with accelerometers, which are close together on a baseline. By mounting several accelerometers on three rotating disks, it is possible to measure all nine gravity gradient elements on a certain position [2].

From equation 2.14 it can be seen that gravity gradient can be approximated by a first order expression. Here, the smaller the mutual distance of the accelerometers, the better the gradient is approximated. However, for small distances the difference in gravity will become extremely small and, as a consequence, difficult to measure.

$$\Gamma_{zz} = \frac{\partial g_z}{\partial z} \approx \frac{\Delta g_z}{\Delta z} \tag{2.16}$$

Note that the indices zz are arbitrary, since the gravity gradient tensor consists of nine elements.

2.4 Measurement techniques

Since it is now known which quantities can be measured considering gravitation, the next step is to investigate which measurement techniques are available for acquiring the information about gravity and/or gradients in gravity. Some techniques can be used only for gravimetry (relative and/or absolute), and other techniques only for determining gradient(s) in gravity. However, some gravimeters can be used to approximate the gravity gradient, as described in section 2.3.

2.4.1 Pendulum based

A method for determining the value of the vertical component g_z of the gravity field can be done using a pendulum. When considering a simple gravity pendulum [7], the oscillating frequency f is given by

$$f = \frac{1}{2\pi}\sqrt{\frac{g_z}{L}} \tag{2.17}$$

where L is length of the pendulum. Since this length L will be constant, the oscillating period can be linked to the value of gravity g_z, as given in equation 2.18.

$$g_z = 4\pi^2 f^2 L \tag{2.18}$$

Adding and applying several techniques to this simple idea, like the reversible pendulum by Helmert [8], measurement sensitivities for the change in (relative) gravity have been obtained in the order of 1 mgal.

2.4.2 Free-fall based

Another possibility to determine the value of the vertical component of the gravity field on Earth g_z is to use a free-fall gravimeter. This is a system consisting of a long vertical tube with a movable mass inside. On this mass the gravity component g_z is acting, resulting in a certain velocity v_z of the mass in the z-direction.

$$v = \int g_z dt = g_z t + v_0 \tag{2.19}$$

Integrating this expression again with respect to time t, the position of the free-falling proof mass is found.

$$z = \int v dt = \int g_z t + v_0 dt = \frac{1}{2} g_z t^2 + v_0 t + z_0 \tag{2.20}$$

The value of g_z can be determined by measuring the time t it takes for the proof mass to travel through the tube over a distance z. Taking this distance z equal to the length of the tube L, and zero start velocity v_0 and similar zero position z_0, equation 2.20 simplifies to

$$L = \frac{1}{2} g_z t^2 \tag{2.21}$$

Measuring the time t yields the value of g_z, since the length of the tube L is constant.

$$g_z = \frac{2L}{t^2} \tag{2.22}$$

Todays commercial gravimeters based on the free-fall principle are capable of measuring gravity with a resolution of about 1 μgal, which is about 1 billionth of Earth's gravitational acceleration of 9.81 m/s^2 [9].

2.4.3 Torsion balance

In the year 1798 Henry Cavendish introduced a measurement system for determining the gravitational constant G from Newton's law on universal gravitation. Therefore, he invented the torsion balance, consisting of a wire (fiber) with a small rod mounted below. On the edges of this rod two *small* proof masses are attached (see figure 2.2). According to Newton's law on universal gravitation (equation 2.1), the proof masses will be attracted by the other *big* masses in their neighborhood.

By putting a mass on an equal distance from each proof mass, the wire will twist a little bit due to the gravitational forces acting on the proof masses. Although the resulting rotation is quite small, it is possible to make the twist visible by placing a mirror onto the wire and use it for reflecting a beam of light on a wall. The shift of the light on the wall

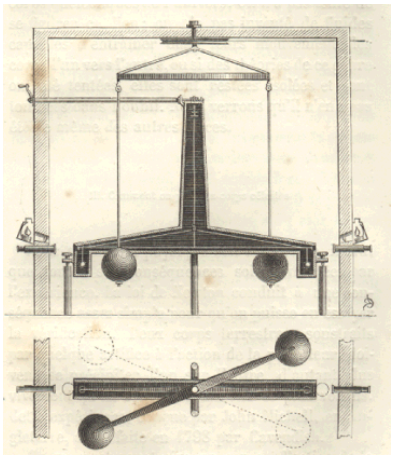

Figure 2.2: *Torsion balance of Cavendish.*

is then a measure for the amount of twist, thus the gravitational forces acting on the proof masses [10].

To eventually determine the value of the gravitational constant G there are (at least) three techniques. One could look at the final deflection of the system, where the system will come to rest after several hours. Another possibility is to determine the equilibrium position of the system by looking at its harmonic behavior, since it will show a damped oscillation. It is also possible to look at the acceleration of the small proof masses, by changing the big masses quickly to another position, and thus changing the force equilibrium [11].

In addition of determining the gravitational constant G, it is also possible to use the device for measuring the gravity gradient components without z-dependency, since the proof masses are on the same level. By rotating the device over specific angles, one can determine these components. Note however that the changes in x and y are quite small, making it difficult to do accurate measurements.

Eötvös torsion balance

A seemingly insignificant modification of the Cavendish torsional balance by Roland Eötvös in the year 1896 resulted in a system capable of measuring gravity gradient [12]. The modification he made was lowering one of the small proof masses using a wire, as can be seen in figure 2.3.

Doing so, the proof masses are not on the same level anymore, implicating that the gravitational effect on the first mass is different in all three directions x, y and z with respect to the second mass. With the use of azimuths (rotating the devices consequently over a specific angle) and associated mathematics, it is possible to determine the desired components of the gravity gradient tensor Γ (instead of the gravitational constant G). Especially for the gradients Γ_{xz} and Γ_{yz} the Eötvös torsion balance shows good results, since the difference in the z-direction is quite large compared to the changes in x- and y-direction.

Making this small modification, Roland Eötvös actually developed world's first gravity gradiometer. Therefore, and also by the relative low changes in gravity over a certain

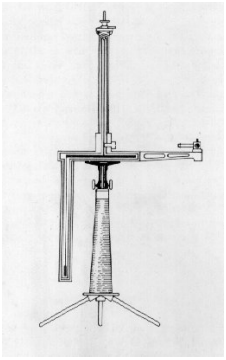

Figure 2.3: *Torsion balance of Eötvös.*

distance, the typical unit used in gravity gradiometry is E(ötvös)[2]. The usefulness of the torsion balance by Eötvös in the 'real world' became clear when it resulted in the discovery of hundreds of oil fields in the 1920's and 1930's [13].

The instruments accuracy was specified at about 1–3 E [4]. Although the instrument is quite accurate, measuring takes a while. Doing just one measurement takes (at least) one hour, since the system needs a long time to stabilize.

2.4.4 Mass-spring system

From mechanics it is known that also a mass-spring system can be used to measure acceleration [14]. In such a system (see figure 2.4) a mass is being accelerated by a force, in this case the gravitational force F_g, and its movement is limited by a spring and damping.

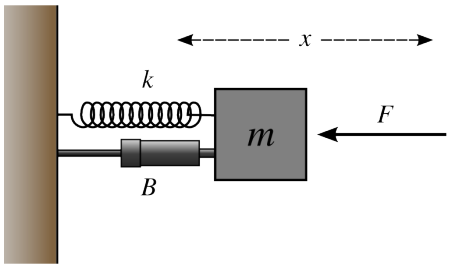

Figure 2.4: *A second order damped mass-spring system.*

The displacement of the mass m is described by a second order differential equation, which is given in equation 2.23. Here, γ is the damping coefficient (in figure 2.4 given by B), K is the spring constant and x is the displacement.

$$m\frac{d^2x}{dt^2} + \gamma\frac{dx}{dt} + Kx = F_g \tag{2.23}$$

[2] $1\ \mathrm{E} = 10^{-9}\ \mathrm{s}^{-2}$.

For gravitational forces below the resonance frequency ω_r of the system

$$\omega_r = \sqrt{\frac{K}{m}} \tag{2.24}$$

the displacement x of the mass is equal to

$$x = \frac{F_g}{K} = g\frac{m}{K} \tag{2.25}$$

which is simply the equation of a spring. Note that this can be also expressed in terms of gravity g, which is eventually of most interest.

Rotating-disk

Although one accelerometer shows limits concerning its (dynamical) range and noise floor, it is possible to improve system performance by using multiple accelerometers. Doing so, it is even possible to measure elements of the gravity gradient tensor.

Another advantage by doing measurements with multiple accelerometers is the reduction of the common mode acceleration, like the acceleration and/or vibration of the platform where the system is mounted on, and the decrease in measurement error [15].

Bell Geospace developed such a system in 1998, capable of determining all nine elements of Γ within a resolution of about 5 E [2]. The basic idea (see figure 2.5) is that there are three disks present, each rotating over an axis (x, y and z).

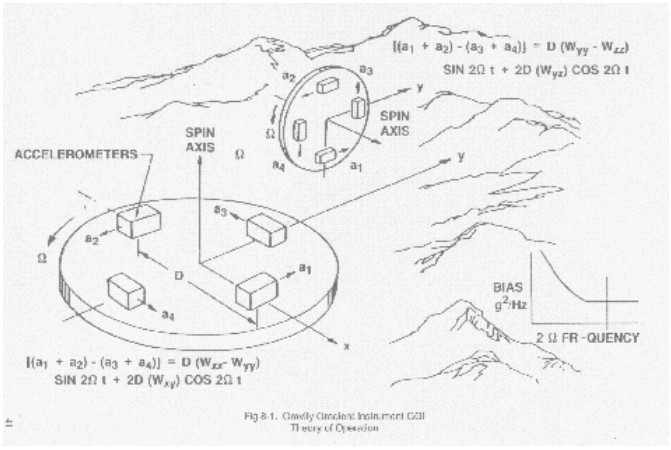

Figure 2.5: *Airborne Gravity Gradiometer by Bell Geospace.*

On each rotating disk four accelerometers are mounted. From the output of all four accelerometers a, the relationship of equation 2.26 can be obtained, where D is the distance between the two accelerometers [16] and ω is the angular velocity of the rotating disk.

$$a_1 + a_2 - a_3 - a_4 = D(\Gamma_{xx} - \Gamma_{yy})\sin(2\omega t) + 2D\Gamma_{xy}\cos(2\omega t) \tag{2.26}$$

With the aid of synchronous detection and demodulation it is possible to determine both Γ_{xy}=Γ_{yx} and (Γ_{xx}-Γ_{yy})/2. A similar approach can be made for the other two rotating

disks, making it eventually possible to determine the values of all nine elements of the gravity gradient tensor Γ.

Zero-length spring

Although the described mass-spring system from figure 2.4 is useful for doing gravity measurements, it requires either a very weak spring and/or a very large mass. To overcome this, LaCoste [17] designed a system which is based on a mass-spring system, but shows infinite displacement when the system is proper balanced for a certain value of gravity. This type of systems is capable of performing measurements in the order of about 1 μgal [5].

In figure 2.6 a schematic view is given of the gravimeter (model G&D) by LaCoste and Romberg [18]. The idea is that using the nulling dial the system is configured in such a way that it becomes unstable when (the vertical component of) the spring force is equal to the (vertical) gravitational force, as will be explained later on. Doing so, very small changes in gravity will result in large displacements of the proof mass, making them measurable quite well.

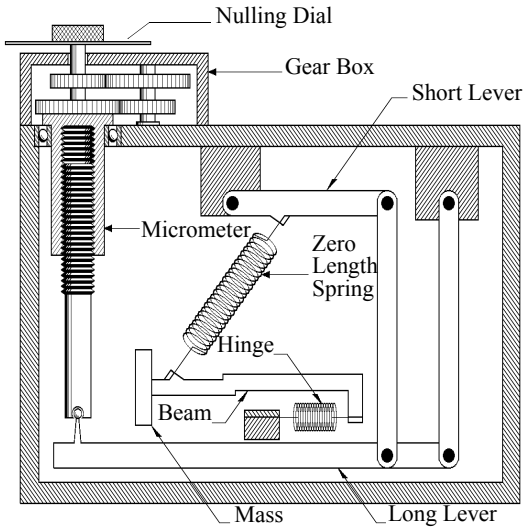

Figure 2.6: *Gravimeter of LaCoste and Romberg (Model G&D).*

To understand the working principle of the system,a schematic view of the mass-spring part of the system is used, as is visualized in figure 2.7.

The basic idea behind the sensor is that it should become a pendulum in vertical direction with infinite period. To achieve this, a beam with a proof mass at one end is constructed which can rotate. First, the torque T_g on the beam due to the weight W of the proof mass is defined.

$$T_g = W d \sin(\theta) \tag{2.27}$$

Furthermore, the effect of the spring on the torque balance has to be defined. Therefore,

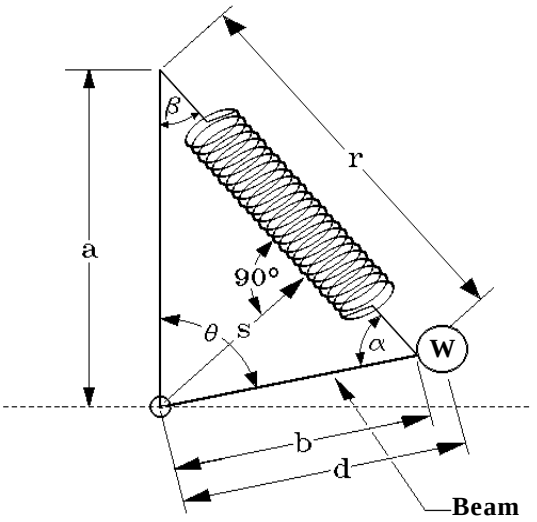

Figure 2.7: *Working principle of the system of LaCoste and Romberg (Model G&D).*

first the relationship between the height of the suspension of the spring a and the lever arm s is derived (see figure 2.7).

$$s = a\sin(\beta) \tag{2.28}$$

Using the law of sines, it is possible to find the relation between the length r of the spring and the distance of the beam from the point of rotation to the proof mass.

$$r = b\frac{\sin(\theta)}{\sin(\beta)} \tag{2.29}$$

Using the spring constant K, the torque T_s generated by the spring can be determined, in which case r_0 is the length of the spring when no torque is applied (initial position).

$$T_s = -K\left(r - r_0\right)s \tag{2.30}$$

Summing both the torque by the weight of the proof mass T_g and the torque by the spring T_s, the total torque T_{tot} present in the system is found.

$$T_{tot} = Kr_0 s + (Wd - Kab)\sin(\theta) \tag{2.31}$$

Although one could now calculate the total torque of the system, the system can be only described by introducing the inertial acceleration of the mass by defining the associated torque T_m, with I the moment of inertia[3].

$$T_m = I\frac{d^2\theta}{dt^2} \tag{2.32}$$

[3]Damping is neglected, since it will slows down the system and making mathematics (much) more complicated. More important, it does not change the working principle.

So, eventually the following relation is obtained

$$Kr_0 s + (Wd - Kab)\sin(\theta) + I\frac{d^2\theta}{dt^2} = 0 \tag{2.33}$$

Now, look what happens if variations are made around the working point. The system is designed in such a way, that the angle θ is around 90 degree (or $\pi/2$ radians). Making a first order approximation at this point results in

$$Kr_0 s + (Wd - Kad) + I\frac{d^2\theta}{dt^2} = 0 \tag{2.34}$$

where

$$I = md^2 \qquad W = mg_z \tag{2.35}$$

Solving this system for appropriate boundary conditions, meaning that at the start the proof mass m is present at its equilibrium position and is not moving, the solution given in equation 2.36 is found.

$$\theta = \frac{1}{2}\frac{\left(Kad - Kr_0 s - mg_z d\right)}{2md^2}t^2 + \frac{\pi}{2} \tag{2.36}$$

From this it can be seen that the system is 'stable' (keeping θ constant for every value of time t) if the following conditions are satisfied.

$$r_0 = 0 \qquad a = \frac{mg_z}{K} \tag{2.37}$$

This means that a *zero-length spring* (r_0=0) is required and that the height a of the suspension point has to be controlled very carefully. It now becomes clear that for small variations in gravity g_z the system is not in equilibrium anymore and the mass m will start to move away from the equilibrium point. Only by adjusting the screw (thus changing a) the system can be put in equilibrium again. Measuring is done by denoting which gravity is associated at a certain setting of the nulling dial.

Superconductivity

Another possibility to increase the performance of a mass-spring based system is to enhance it with superconductivity. This can be explained using the superconducting accelerometer given in figure 2.8, which is a design by Paik [19].

On the left the mass-spring system is recognized. When the superconductive proof mass is displaced (by gravitation) the inductance of the coil is modulated. From this, the resulting induced current is converted by a Superconducting Quantum Interference Device (SQUID) to an output voltage signal, making it possible to determine the displacement of the mass, thus the gravitational forces acting on it.

Since it is possible to measure very small changes in inductance, it means that also similar changes are measurable within the gravitational field. According to Baldi et al. [20] theoretical accuracy of such a device lies within a deviation of 1 ngal. Taking geophysical and environmental noise into account, still an effective accuracy of 0.1 μgal can be achieved.

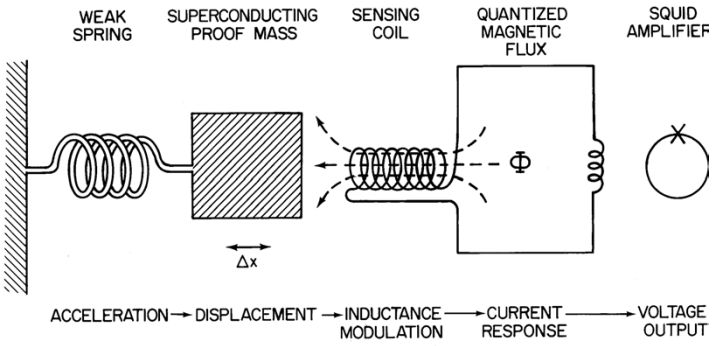

Figure 2.8: *Principle of a superconducting accelerometer.*

Taking two of these superconducting accelerometers and mounting them on a baseline, a Superconducting Gravity Gradiometer (SGG) is easily created. In figure 2.9 such a device is given, designed by the University of Maryland [19].

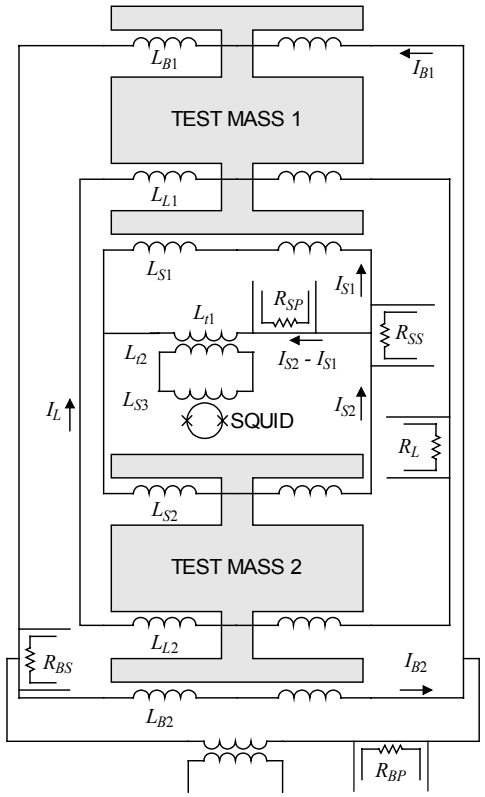

Figure 2.9: *Circuit diagram for each axis of a Model II SGG.*

The resolution of such a system lies within 1–5 E, but can be improved to below 1 E when reducing geophysical and environmental noise [20].

Micro Electro Mechanical Systems

All systems treated until now are quite large systems, but there are also possibilities to develop a sensitive mass-spring system using Micro Electro Mechanical System (MEMS) technology. There have been many developments within this field of research, and accelerometers made with bulk-micromachining nowadays show a resolution (by looking at its noise floor) of 10 μgal/$\sqrt{\text{Hz}}$ [21].

When measurements can be done within a typical bandwidth from 1 mHz – 1 Hz and the mechanical bandwidth of the sensor is 1 Hz, this leads to a sensitivity of 10 μgal. An overview of MEMS accelerometers is given in figure 2.10.

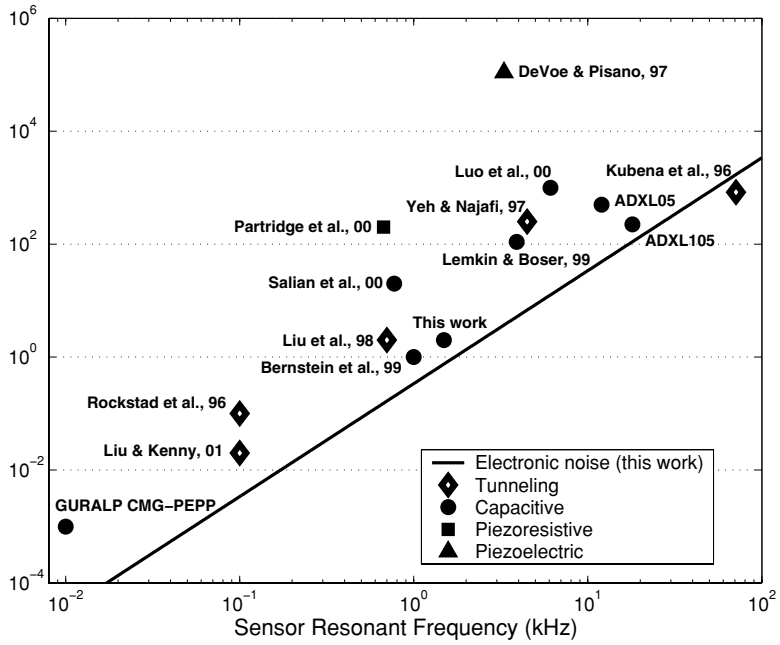

Figure 2.10: *Comparison of the noise floor of MEMS accelerometers [22].*

However, still no (commercial) MEMS accelerometers exist for gravitational applications. Since the displacement x of the proof mass m in a MEMS accelerometer can also be described by

$$x = \frac{g}{4\pi^2 f_r^2} \tag{2.38}$$

where g is the gravitational acceleration of the mass, it becomes clear that for large displacement x a low resonance frequency is required [21]. Looking at figure 2.10, it can be seen that most accelerometers have a resonance frequency f_r of about 1 kHz and gravitational effects are measured typically around (just) 1 Hz.

The consequence of equation 2.38 is that, although the resolution given above is quite interesting, it is the challenge to perform an appropriate readout, since it are actually very small displacements. For example, a mass can move 0.1 pm above its noise floor for a

certain gravity, but such a small displacement is (very) difficult to measure using common readout techniques. Therefore, the values given in figure 2.10 can be confusing.

2.4.5 Vibrating-string

To improve dynamic range for gravity measurements and keeping the device small, vibrating-string gravimeters are developed. Such a device consists of a string, which can be (vertically) suspended on one or both ends. Also, one or more masses are mounted onto the string[4], as can be seen in figure 2.11.

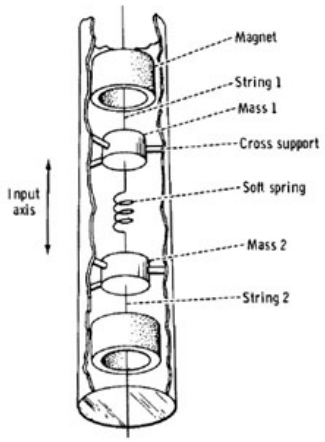

Figure 2.11: *Vibrating string gravimeter.*

The string itself is made of an electrically conducting material that oscillates at its resonance frequency in a magnetic field. Using the oscillating voltage it is possible to further excite the string. When the gravity changes, the resonance frequency of the system changes also, which is eventually measured [4].

Another approach is taken by Golden et al. [23], who designed the Gravitec Gravity Gradiometer. This is a device for measuring the gravity gradient components Γ_{xz} and Γ_{yz} inside a borehole, with a resolution of about 5 E.

They use a vertically suspended wire, with inductive readouts mounted at the 1/4 and 3/4 positions along the length of the wire. The wire itself is periodically brought under tension. Changes in gravity gradient will cause perturbations which are measured. To understand why this combination of changing the tension in the wire and changes in gravity gradient can be measured, consider a simplified model consisting of one mass on the wire (see figure 2.12).

Regarding the forces present, take the inertial acceleration of the mass m into account, and also the tension T in the wires, the viscous damping γ by the movement in air and the gravitational acceleration g of the mass. Summing these forces gives the force balance in

[4]In the case of a vertically suspended string with a freely suspended mass on one end it behaves as (and actually is) a pendulum.

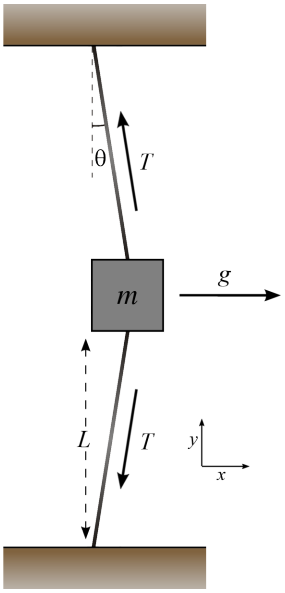

Figure 2.12: *Principle of the vibrating string gravimeter.*

equation 2.39.

$$m\frac{d^2x}{dt^2}+\gamma\frac{dx}{dt}+2T\sin(\theta)=mg \tag{2.39}$$

Although this seems to be an awkward differential equation, the term with angle θ can be approximated as given below.

$$\sin(\theta)\approx\theta\approx\tan(\theta)=\frac{x}{L} \tag{2.40}$$

Now, a new expression for the force balance can be given as

$$\frac{d^2x}{dt^2}+\Gamma\frac{dx}{dt}+\omega_0^2x=g \tag{2.41}$$

where ω_0 and Γ have been defined as

$$\omega_0=\sqrt{\frac{2T}{mL}} \qquad \Gamma=\frac{\gamma}{m} \tag{2.42}$$

When the system is stabilized, the displacement x for gravitational accelerations with a frequency below the resonance frequency (the static case) is given by

$$x=\frac{g}{{\omega_0}^2}=\frac{1}{2}\frac{mgL}{T} \tag{2.43}$$

From this it becomes clear that the displacement is proportional to the gravitational acceleration g. But, by changing the tension T in the wire periodically, the displacement x can be modulated. Especially when this tension is modulated around its first harmonic

frequency, of the system, the displacement is quite large for a relative small gravitational acceleration g.

Taking two places on the wire and exciting it at its *second* harmonic frequency, only a *gradient* in gravity will give displacement of the wire at the 1/4 and 3/4 positions, which is the basic idea behind the design of the earlier described sensor of Gravitec. Note that in this case the wire looks like a wave with one full period.

2.4.6 Atom interferometry

Gravity measurements can also be done using atom interferometry with a Mach-Zehnder configuration. This is a technique which uses the fact that atoms also behave as waves (quantum mechanics). From Peters et al. [24] can be learned that gravity introduces an extra phase difference $\Delta\phi$, as given in equation 2.44, where k is the Raman laser wave number, g is gravity and T is the interrogation time.

$$\Delta\phi = 2kgT^2 \tag{2.44}$$

By measuring this phase difference the value for the gravity g can be determined, which is also illustrated in figure 2.13. Here, on certain interrogation times T the phase difference between the presence and absence of gravity can be seen. Using this method, it is possible to determine gravity with a resolution of about 2 μgal.

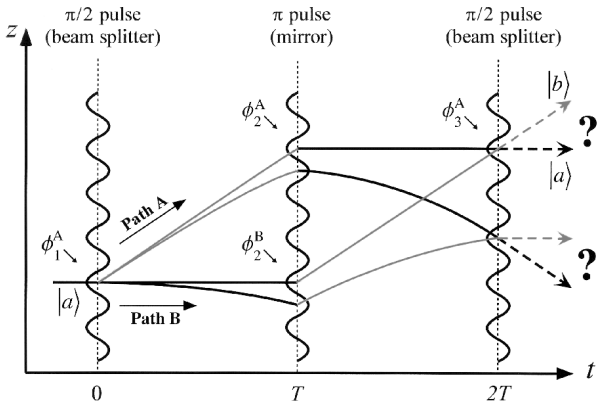

Figure 2.13: *Basic Mach-Zehnder atom interferometer with (curved lines) and without (straight lines) gravity.*

2.5 Conclusions

Using Newton's law for universal gravitation, gravitational accelerations can be described. These accelerations can be separated into gravity and its gradient. Both quantities can be measured using several techniques.

Measuring gravity, which is for most techniques toward the center of the Earth, can be done using a pendulum based system, by investigating its oscillation frequency. Also the

free-fall principle can be used, by determining the time which an object needs to displace itself over a certain distance. Mass-spring systems are available in several types (MEMS, zero-length spring, superconductive). Another type of measuring gravity is using atom interferometry. Typical resolutions which can be achieved performing gravimetry are about 1 μgal.

Gravity gradient can be measured using the systems for gravimetry and performing measurements on different locations, in order to approximate the gradient in gravity. Other systems can measure gravity gradients on one specific location rightaway, like the Eötvös torsion balance and a gradiometer based on the vibrating string principle. Best resolutions for gravity gradient measurements are about 1–5 E.

References

[1] D. C. Giancoli. *Physics*. Prentice Hall, Upper Saddle River, New Jersey, Fifth edition, 1998.

[2] S. Hammond and C. Murphy. "Air-FTG: Bell Geospace's Airborne Gravity Gradiometer – A Description and Case Study". In *Airborne Gravity*, 2003.

[3] J. Stewart. *Calculus – Early Transcendentals*. Brooks/Cole, United States of America, Fifth edition, 2003.

[4] M. Nabighian, M. Anders, V. Grauch, R. Hansen, R. LaFehr, Y. Li, W. Pearson, J. Peirce, J. Phillips, and M. Ruder. "Historical development of the gravity method in exploration". *Geophysics*, **70**(6):63–86, 2005. 75th Anniversary.

[5] J. van Popta and S. Adams. "Reprint of Gravity Gains Momentum". Technical report, Micro-g LaCoste, 2008.

[6] D. Simpson. *Gauss's Law for Gravity*. Prince George's Community College, 2006. Department of Physical Sciences and Engineering.

[7] C. Huygens. *Horologium Oscillatorium*. 17th Century Maths, 1673.

[8] F. Helmert. *Die mathematischen und physikalischen Theorien der höheren Geodäsie*. Teubner, 1884.

[9] M. van Camp, T. Camelbeeck, and P. Richard. "The FG5 absolute gravimeter: metrology and geophysics". *Physicalia Magazine*, **25**(3):161–174, September 2003.

[10] I. Falconer. "Henry Cavendish: the man and the measurement". *Measurement Science and Technology*, **10**:470–477, 1999.

[11] PASCO scientific. "Gravitational Torsion Balance", 1998.

[12] I. Rybàr. "Eötvös Torsion Balance Model E-54". *Geofisica Pura e Applicata*, **37**(1): 79–89, 1957.

[13] Z. Szabó. “Biography of Loránd Eötvös”. *The Abraham Zelmanov Journal*, **1**:1–8, 2008.

[14] M. Elwenspoek and G. Krijnen. *Introduction to Mechanics and Transducer Science*. University of Twente, 2003.

[15] M. J. Molny and M. Feinberg. “Stepped Gravity Gradiometer”, August 1994.

[16] D. E. Dosch and D. L. Sieracki. “Gravity Gradiometer and Method for Calculating a Gravity Tensor with Increased Accuracy”, October 2004.

[17] L. LaCoste. “A new type of long-period vertical seismograph”. *Physics*, **5**:178–180, 1934.

[18] L. LaCoste and A. Romberg. *Model G&D Gravity Meters*. LaCoste & Romberg, Austin, Texas, U.S.A., 2004.

[19] H. J. Paik. “Three-Axis Superconducting Gravity Gradiometer”, June 1989.

[20] P. Baldi, G. Casula, S. Focardi, and F. Palmonari. “Tidal analysis of data recorded by a superconducting gravimeter”. *Annali di Geofisica*, **38**(2):161–166, May 1995.

[21] J. Flokstra, R. Wiegerink, H. Hemmes, and J. Sesé. “Gravity gradient sensor concepts and related technologies for planetery/lunar missions”. Technical report, ESA, 2004.

[22] X. Jiang, F. Wang, M. Kraft, and B. E. Boser. “An Integrated Surface Micromachined Capacitive Lateral Accelerometer with $2\mu\mathrm{G}/\sqrt{\mathrm{Hz}}$ Resolution”. In *Solid-State Sensor, Actuator and Microsystems Workshop*, Hilton Head Island, South Carolina, June 2–6 2002.

[23] H. Golden, W. McRae, and A. Veryaskin. “Description of and Results from a Novel Borehole Gravity Gradiometer”. In *ASEG*, Perth, Western Australia, 2007.

[24] A. Peters, K. Y. Chung, and S. Chu. “High-precision gravity measurements using atom interferometry”. *Metrologia*, **38**:25–61, 2001.

Chapter 3

Design and analysis

Now that measuring techniques for gravity have been investigated, one of these should be chosen to use for a gravity (gradient) sensor fabricated using MEMS technology. Once known, all associated physics, important phenomena and parasitic effects will be addressed. Finally, a summary is given of the design of the proposed sensor.

3.1 Introduction

In chapter 2 several methods for determining the value of the gravitational acceleration in a certain direction and/or its gradient were discussed. Since eventually a gravity (gradient) sensor using MEMS technology should be used, each measurement technique will be discussed briefly and determined if it is a potentially technique to implement as a Micro Electrical Mechanical System.

Pendulum based is a rather straightforward system, measuring the value of gravity based on the oscillating frequency of the system. However, within MEMS it is difficult to create a mass that large compared to its suspension for free oscillations, since a (virtual) mechanical frictionless pivot is recommended for well-defined pendulum behavior.

Free-fall based shows a quite good accuracy for gravity measurements. However, measuring a free-fall requires a free mass, which is difficult to realize, since the mass should be *within* a tube/cavity. In addition, the accuracy of the measurement improves when using a large tube. Comparing this to fact that MEMS means systems on the micrometer scale, this method will offer a lot difficulties using such technology.

Torsion balance is a method which actually introduced the gravity gradient measurements with good accuracy. However, within MEMS it requires rotational parts and 'long' fibers, which should be very 'weak' in certain directions. These requirements give a big challenge concerning fabrication, where for reasonable sensitivity the structure will probably not survive the fabrication process.

Accelerometer is a generalized concept, also for MEMS fabrication. Today, there are many (commercial) MEMS accelerometers based on the concept discussed before. However,

they are not sensitive enough yet for use within the gravitational field.

Zero-length spring can be interesting for MEMS applications. However, it is very difficult to design such a system. In the first place, it requires a structure which can freely rotate over a certain point. More important, it requires a zero-length spring. Until now, such a spring has not been developed using MEMS technology. This is probably a difficult task, since it requires actually a (very stable) force stored in the device itself, generated during fabrication.

Vibrating string could be realized within MEMS, only the generated deflections by gravitational effects are too small to measure using conventional MEMS-readout techniques. Some vibrating string devices from chapter 2 use a metal wire combined with inductive readout, which is not usually done within MEMS technology. Others use a periodically change in tension in the string, which could be done within MEMS, but has to be thought out.

Superconductive shows very good accuracy, but the combination of MEMS with superconductivity is quite rare. In addition, the advantage of a MEMS product should be its form factor. When using superconductivity, the form factor is mainly determined by the cooling part of the system and not the accelerometer(s).

Atom interferometry is a nice concept with good results, but it will be very challenging to build such a system with MEMS technology.

In this description the devices are treated with respect to the feasibility within MEMS technology. For design choices also the achievable resolution(s) are taken into account. The results of this investigation are given in figure 3.1, where the accuracy for gravity measuring is compared to the accuracy for measuring gravity gradient.

Note that two techniques (torsion balance and vibrating string) are not used for gravity measurement. Therefore, they are plotted on the upper left of the graph. Also, several methods are specified for measuring (just) gravity. To calculate its equivalent sensitivity in gravity gradient, the 'smallest' mutual distance between two sensors has been estimated using the dimensions.

In this diagram of comparison it can be seen that mass-spring systems using superconductivity produce by far the best results regarding accuracy in both gravity and its gradient. It is also clear that a pendulum, despite its simplicity, shows the least measurement accuracy. Also the performance and position with respect to other methods of (MEMS) accelerometers should be denoted.

3.1.1 Design choice

Considering all treated methods with their accuracy and possibilities and looking at the feasibility within MEMS technology, it is concluded that a very sensitive *MEMS accelerometer* should be realized. Using multiple of these, it is possible to measure both gravity and its gradient.

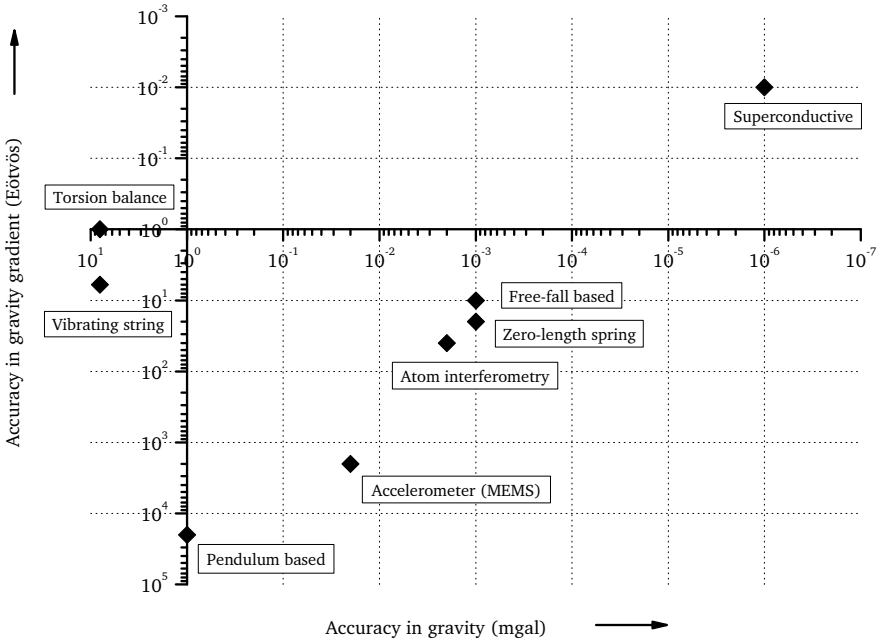

Figure 3.1: *Comparison of several methods for measuring gravity (gradient).*

Although focusing on this technique, thinking about the construction of a *zero-length spring* made with MEMS technology can be fruitful. If a system with such a spring can be realized, it is possible to make a very sensitive accelerometer using a new concept within the world of Micro Electro Mechanical Systems. Next, a closer investigation of the *vibrating string* could be interesting. Such a device might be difficult to realize, considering aspects like maximum stress during fabrication and required flexibility of the string (silicon is rather stiff).

3.2 Main design

An accelerometer can be described by a mass-spring system, because the main behavior of the system is described by the size of the mass m and the spring constant K of the springs. Since the sensor requires a rather large sensitivity, a sensor with a large proof mass and a low spring constant of the beams should be used, as will be explained in this chapter. Important for the sensor is that it should measure (very) small changes in gravity, but it should be able to withstand Earth's gravity. Therefore, gravity (gradient) will be measured in the horizontal direction, since Earth's gravity acts in the vertical direction.

In MEMS it is common to fabricate springs using small silicon beams. For this accelerometer the same type of spring will be used. Of course, the desired sensitivity gives some requirements regarding the design and fabrication of these beams. To prevent the mass from

extreme displacements with respect to its initial position the sensor is designed in such a way that the beams are clamped-guided suspended. Note that the design of the sensor is fully symmetric (over both visible axes), to improve the linear behavior of the sensor.

A schematic 2-dimensional view of the sensor is given in figure 3.2. Remark that the eventual sensor is realized in 3 dimensions, wherein the design is also symmetric over the third axis, leading to a total of eight beams, each with spring constant K, supporting the proof mass m.

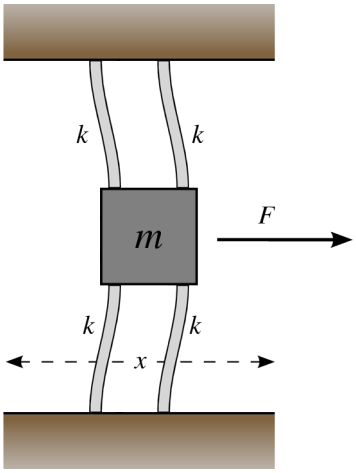

Figure 3.2: *Schematic view of the MEMS accelerometer (with beams).*

3.3 Springs

Describing the sensor by a mass-spring system requires a close investigation of both mass and spring(s) for proper designing. Since the mass will be made out of silicon, the mass can only be changed by its dimensions, since the mass m is given by

$$m = \rho V \tag{3.1}$$

where ρ is the density of silicon (2.23 g/cm^3) and V is the volume of the mass, which is determined by the design.

Investigating the springs is significantly more difficult. Sequentially, the main spring behavior of a beam, the effects of axial loading, the shortening of curvature, the equivalent spring constant and the effect of buckling are discussed.

3.3.1 Bending

Before doing the calculations concerning the spring constant of the bending beam, Hooke's law needs to be investigated. Normally, Hooke's law for the relation between stress σ and strain ϵ is considered for one dimension, which is given by

$$\sigma = E\epsilon \tag{3.2}$$

where E is Young's modulus. Actually, Hooke's law can be viewed in two dimensions by a stress-strain relationship [1]. Here, a certain correction is applied for Hooke's law, because when the (isotropic) material is elongated by tensile forces in the x-direction, it becomes shorter in the y direction by compression. The amount of compression in the y-direction is defined by the Poisson's ratio ν, where ϵ is the relative elongation (strain).

$$\nu = -\frac{\epsilon_y}{\epsilon_x} \tag{3.3}$$

With this information the effect of stress σ in both x- and y-direction on the strain in the x-direction ϵ_x can be calculated.

$$\epsilon_x = \frac{\sigma_x - \nu\sigma_y}{E} \tag{3.4}$$

The effect of stress σ on strain ϵin the y-direction is done in a similar way. Eventually, this leads to the following stiffness matrix.

$$\begin{bmatrix} \sigma_x \\ \sigma_y \end{bmatrix} = \begin{bmatrix} \frac{E}{(1-\nu^2)} & \frac{\nu E}{(1-\nu^2)} \\ \frac{\nu E}{(1-\nu^2)} & \frac{E}{(1-\nu^2)} \end{bmatrix} \begin{bmatrix} \epsilon_x \\ \epsilon_y \end{bmatrix} \tag{3.5}$$

When looking at the relation in x-direction, the relationship between the stress σ_x and the strain ϵ_x is found.

$$\sigma_x = \frac{E}{(1-\nu^2)}\epsilon_x \tag{3.6}$$

Note that the effective elasticity modulus E is a bit larger than the one for the one-dimensional case (equation 3.2), which is the result of the compression of the material in the y-direction. In case of silicon an increase of about 7.8% for the effective elasticity modulus E is found, considering a Poisson's ratio of 0.28. It is also possible to apply a three-dimensional analysis, but since all analysis is done in (quasi)-two dimensions, only this correction is applied.

Next, look at the moment of inertia I of the beam, which is also needed for the calculation of the behavior of the beam. The moment of inertia of the beam is given by its thickness t and its width w

$$I = \frac{tw^3}{12} \tag{3.7}$$

Investigating bending of the beam using [2], a differential equation can be formulated which describes the deflection of the beam δ.

$$P_b x - M_0 + \frac{EI}{(1-\nu^2)}\frac{d^2\delta(x)}{dx^2} = 0 \tag{3.8}$$

This differential equation has the following general solution.

$$\delta(x) = \frac{(1-\nu^2)}{EI}\left(\frac{1}{6}x^3 P + \frac{1}{2}M_o x^2\right) + C_1 x + C_2 \tag{3.9}$$

The constants C_1, C_2 and M_0 can be solved using the boundary conditions. To investigate what these boundary conditions are, have a look at the clamped-guided beam, as is given in figure 3.3.

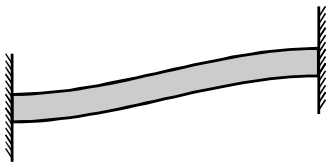

Figure 3.3: *Clamped-guided beam.*

From this it can be seen that both ends are suspended in such a way that the beam cannot rotate at the end points. Also the angle of the beam on both ends is zero for every deflection δ of the beam. Next, it is not surprising that the beam on one end is attached in such a way that is does not move. Combining leads to the boundary conditions given in equation 3.10.

$$\left.\frac{d\delta(x)}{dx}\right|_{x=L} = \left.\frac{d\delta(x)}{dx}\right|_{x=0} = \delta(x)|_{x=0} = 0 \tag{3.10}$$

Solving for these boundary conditions yields the final solution for the deflection δ.

$$\delta(x) = \frac{P_b x^2(3L-2x)(1-\nu^2)}{12EI} \tag{3.11}$$

Since it is mainly interesting to look at the deflection at the end of the beam (x=L), evaluating equation 3.11 at gives

$$\delta = \frac{P_b L^3(1-\nu^2)}{12EI} \tag{3.12}$$

or rewritten

$$P_b = \frac{12EI\delta}{L^3(1-\nu^2)} \tag{3.13}$$

In equation 3.12 a linear relation is observed between the force P_b and the deflection δ of the beam. Since a spring constant is defined as

$$K = \frac{dF}{dx} \tag{3.14}$$

where F is the force and x is the associated displacement, this can also be done for the expression in equation 3.13, to determine the spring constant K of a single beam.

$$K = \frac{dP_b}{d\delta} = \frac{12EI}{L^3(1-\nu^2)} = \frac{Etw^3}{L^3(1-\nu^2)} \tag{3.15}$$

3.3.2 Axial loading

In the case of the previously described beam axial forces are neglected, since only a transversal force P_b is applied. However, axial forces will be present by the fact that the weight of the proof mass m has to be supported by the beams, as illustrated in figure 3.4.

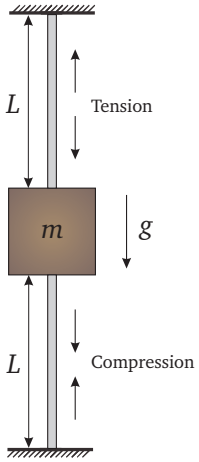

Figure 3.4: *Illustration of tensile and compressive effects in the beams.*

Therefore, the differential equation 3.8 is extended with a term for axial loading with force S.

$$P_b x - S\delta(x) - M_0 + \frac{EI}{(1-\nu^2)}\frac{d^2\delta(x)}{dx^2} = 0 \tag{3.16}$$

The general solution for the deflection δ from this differential equation is different with respect to the one without axial loading, as might be expected.

$$\delta(x) = C_1 e^{\kappa x} + C_2 e^{-\kappa x} - \frac{xP - M_0}{S} \tag{3.17}$$

where

$$\kappa = \sqrt{\frac{S(1-\nu^2)}{EI}} \tag{3.18}$$

Again, solve the previous by determining the constants C_1, C_2 and M_0 considering the (same) boundary conditions.

$$\left.\frac{d\delta(x)}{dx}\right|_{x=L} = \left.\frac{d\delta(x)}{dx}\right|_{x=0} = \delta(x)|_{x=0} = 0 \tag{3.19}$$

This will eventually lead to a beam deflection δ_A at the end of the beam L, which is given by Young and Budynas [3].

$$\delta_A = \frac{P_b\left(-2\cosh(\kappa L) + 2 + \kappa L \sinh(\kappa L)\right)}{\kappa S \sinh(\kappa L)} \tag{3.20}$$

The deflection over the beam itself can also be calculated, but is not given here, since it is mathematically quite complicated. Similar to the case with the absence of axial loading S, defining the spring constant K_t (using equation 3.14) leads to the expression below.

$$K_t = \frac{2 - 2\cosh(\kappa L) + \kappa L \sinh(\kappa L)}{\kappa S \sinh(\kappa L)} \tag{3.21}$$

Notice that this is only valid for beams under *tension*, meaning the beams are stretched. In the design these are the upper beams (see figure 3.4). For the lower beams one should look at effects by *compression*, which is treated similar. The solution for this is also given by Young and Budynas [3]. The final spring constant for compression K_c is then

$$K_c = \frac{2 - 2\cos(\kappa L) + \kappa L \sin(\kappa L)}{\kappa S \sin(\kappa L)} \tag{3.22}$$

Note that this expression for K_c is only valid for reasonable loads, since the device will buckle at a certain load, which is described in subsection 3.3.5. A graphical representation of K_c and K_t (using arbitrary values) is given in figure 3.5. In this plot it can be seen that a beam under axial tension will becomes stiffer, and under compression it will becomes weaker and eventually starts to buckle.

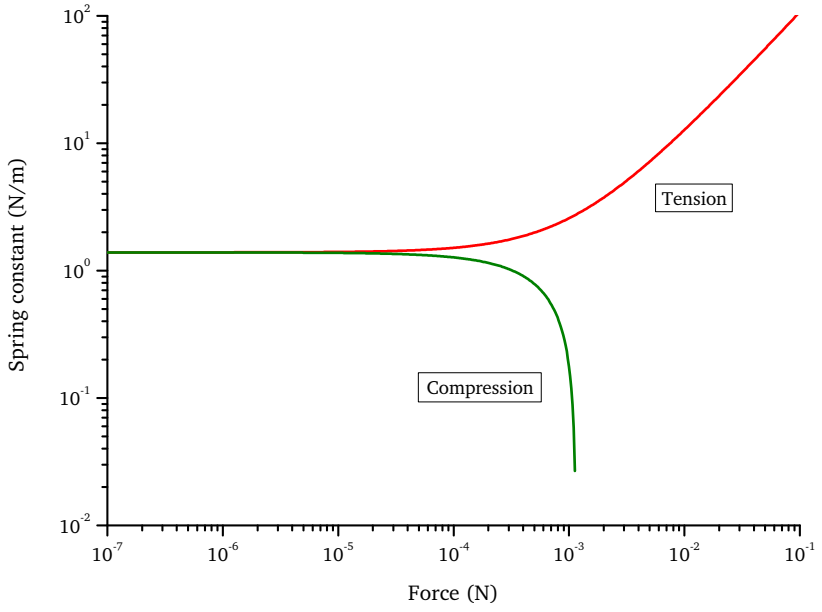

Figure 3.5: *Spring constant under compression and tension.*

Because the total system will consist of the same number beams (totally n beams) under tension as under compression, the spring constants are added[1], giving the total spring constant K_{tot} of the system. Note that in case the values for K_c and K_t show mutual deviance,

[1]This is allowed, since the system is designed in such a way that buckling will not occur.

the proof mass will not only move translational, but also a bit rotational.

$$K_{tot} = \frac{n}{2}K_c + \frac{n}{2}K_t \tag{3.23}$$

3.3.3 Curvature shortening

When the beam is deflecting and its ends can only move in the direction of deflection due to its clamped-guided suspension, it needs to become longer (regard figure 3.6).

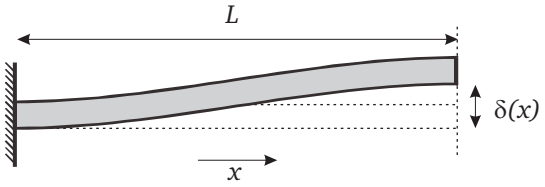

Figure 3.6: *Illustration of curvature shortening on a clamped-guided beam structure.*

Use arc length L_a to determine its associated elongation [4], where a beam of (default) length L is considered with deflection δ.

$$L_a = \int_0^L \sqrt{1 + \left(\frac{d\delta(x)}{dx}\right)^2}\, dx \tag{3.24}$$

This equation uses Pythagoras' theorem for small elements to calculate the total arc length L_a. When looking to such a small element with length ds over a distance dx, this can expressed as

$$ds = dx\sqrt{1 + \left(\frac{d\delta(x)}{dx}\right)^2} \tag{3.25}$$

Since the elongation of such an element ds is interesting, subtract the length dx from it, leading to

$$ds - dx = dx\left(\sqrt{1 + \left(\frac{d\delta(x)}{dx}\right)^2} - 1\right) \tag{3.26}$$

Using binomial series, an approximation for the previous expression can be formulated.

$$\sqrt{1+t} = 1 + \frac{t}{2} - \frac{t^2}{8} + \frac{t^3}{16} - \ldots \tag{3.27}$$

For small deflections (t is much smaller than 1), a first order approximation can be used.

$$\sqrt{1+t} \approx 1 + \frac{t}{2} \tag{3.28}$$

Now, substitute the term $\left(\frac{d\delta(x)}{dx}\right)^2$ for t, which leads to

$$ds - dx = dx\sqrt{1 + \frac{1}{2}\left(\frac{d\delta(x)}{dx}\right)^2} - 1 \approx \frac{1}{2}\left(\frac{d\delta(x)}{dx}\right)^2 \tag{3.29}$$

The total curvature shortening λ is then defined as the integral over all changes in length of the small elements, valid for small deflections of the beam.

$$\lambda = \frac{1}{2}\int_0^L \left(\frac{d\delta(x)}{dx}\right)^2 dx \tag{3.30}$$

Using this equation for the deflection of the beam given in equation 3.11, the shortening λ can be found as a given force P divided over n beams.

$$\lambda = \frac{1}{2}\int_0^L \left(\frac{xP(L-x)(1-\nu^2)}{2nEI}\right)^2 dx \tag{3.31}$$

Doing so, this leads to

$$\lambda = \frac{P_b^2 L^5 \left(1-\nu^2\right)^2}{240n^2E^2I^2} \tag{3.32}$$

This can be rewritten to a relationship for the deflection δ with the use of equation 3.13, giving

$$\lambda = \frac{3\delta^2}{5L} \tag{3.33}$$

3.3.4 Equivalent spring constant

To investigate whether the effect of curvature shortening will become important, some spring constants are calculated. First, Hooke's law is applied for elongation of the beam in the axial direction by Hibbeler [2], with the correction for Poisson's ratio ν in the two-dimensional case. This relationship is given in the equation below, where S is the axial force, λ is the elongation, E is the Young's modulus, L is the length of the beam and A is the cross-sectional area.

$$\lambda = \frac{SL(1-\nu^2)}{EA} \tag{3.34}$$

For a given elongation λ, the required force S needs to be calculated. Using the expression for curvature shortening λ by equation 3.33, also the relationship between the deflection δ of the beam in the *horizontal* direction and the associated axial force S in the *vertical* direction is determined.

$$S = \frac{\lambda EA}{L(1-\nu^2)} = \frac{3\delta^2 AE}{5L^2(1-\nu^2)} \tag{3.35}$$

To determine the associated force P_S in transversal direction, define the angle θ between the beam and the direction of deflection, where L is the length of the beam, n is the number of beams and S is the axial force in the beam.

$$P_s = nS\sin\theta \approx nS\theta \approx nS\tan(\theta) = nS\frac{\delta}{L} \tag{3.36}$$

Combining this with equation 3.35, the relationship between the force P_S in the transversal direction and the deflection δ in the *same* direction of the beam is found. Notice that this effect of curvature shortening is a non-linear relationship, and compare it to the deflection by transversal forces (regard equation 3.13), which is a linear relationship.

$$P_s = \frac{3\delta^3 AnE}{5L^3(1-\nu^2)} \tag{3.37}$$

To calculate the equivalent spring constant, by taking the effect of curvature shortening into account, have a look at the mechanical energy E_{tot}, by integrating the forces P_b and P_S over its displacement δ. Note that in this case the effect of spring stiffening is neglected, since it will make analytically treatment of the equivalent spring constant very difficult. More important, it is seen later on that the design is made in the regime where the effect of spring stiffening is negligible.

$$E_{tot} = \int_0^{\delta} P_b + P_s d\upsilon \tag{3.38}$$

Writing out this expression yields the expression below.

$$E_{tot} = \int_0^{\delta} \frac{12nEI\upsilon}{L^3(1-\nu^2)} + \frac{3\upsilon^3 AnE}{5L^3(1-\nu^2)} d\upsilon \tag{3.39}$$

Evaluating the previous expression leads to the following equation for the total energy E_{tot} of the beam.

$$E_{tot} = \frac{3nE\delta^2(40I+\delta^2 A)}{20L^3(1-\nu^2)} \tag{3.40}$$

From this energy the total force F_{tot} can be deduced by differentiating it with respect to the displacement δ.

$$F_{tot} = \frac{dE_{tot}}{d\delta} = \frac{3nE\delta(20I+\delta^2 A)}{5L^3(1-\nu^2)} \tag{3.41}$$

Differentiating again (with respect to δ) yields the equivalent spring constant K_{tot}, where n is the number of beams.

$$K_{tot} = \frac{dF_{tot}}{d\delta} = \frac{3nE(20I+3\delta^2 A)}{5L^3(1-\nu^2)} \tag{3.42}$$

From this result it is observed that the effect of curvature shortening contributes to the total spring constant E_{tot}. This effect can also be visualized by expanding the expression for

K_{tot} in two separate parts, namely K_b for the spring constant by the beam theory and K_s by the axial stiffening (see figure 3.7).

$$K_b = \frac{12nEI}{L^3(1-\nu^2)} \qquad K_s = \frac{9nE\delta^2 A}{5L^3(1-\nu^2)} \tag{3.43}$$

Note that the effect of spring stiffening is non-linear, regarding the presence of the deformation δ of the system.

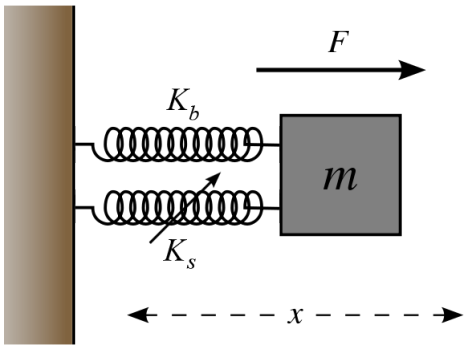

Figure 3.7: *Schematic view of the 'nominal' spring (K_b) and stiffening spring (K_s).*

It is interesting to look when this effects becomes equal to the 'nominal' spring constant (regard equation 3.15). From the previous equation it can be quickly determined that this occurs when

$$20I = 3\delta^2 A \tag{3.44}$$

where I is the moment of inertia I and A is the cross-sectional area of the beam. Since in this case the beam has a rectangular cross-section with width w and thickness t, I and A can be expressed as

$$A = wt \qquad I = \frac{tw^3}{12} \tag{3.45}$$

Combining this with equation 3.44, the following relationship between the deflection δ and the width w of the beam is obtained.

$$\delta = \sqrt{\frac{5}{9}}w \tag{3.46}$$

This means that when the deflection δ is about 0.75 times the width w of the beam, axial stiffening will become important regarding the behavior of the system. The effect of axial stiffening is also visualized in figure 3.8, where both the 'nominal' spring constant and the spring constant by axial stiffening are plotted, together with the resulting total spring constant. More information about spring stiffening effects and associated graphs can be found in appendix B.

This analysis is useful for determining the operating range of the sensor for a given range of gravitational accelerations. It becomes especially interesting when one would like

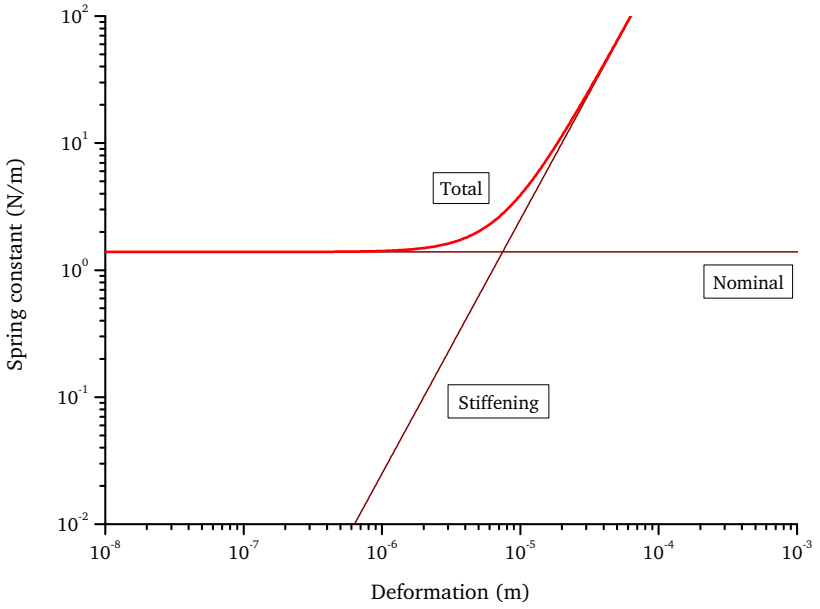

Figure 3.8: *Nominal stiffening, axial stiffening and total spring constant.*

to sense also in the vertical direction. Until now, the design was only considered for its horizontal operation, meaning that Earth's gravity is not measured. Measuring (changes in) Earth's gravity can be done by rotating the sensor 90 degree, as is given in figure 3.9.

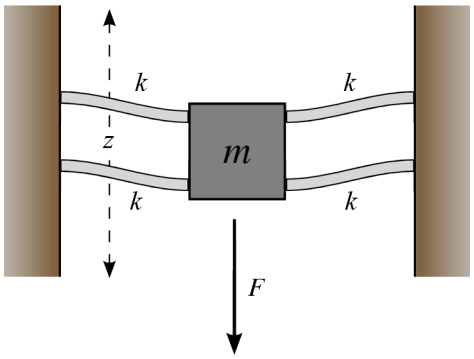

Figure 3.9: *Using the sensor for measuring Earth's gravity.*

Doing so, the device can become orientation independent, because it can measure gravitational accelerations in every direction. Since Earth's gravity should be measured within a certain range, one could say that Earth's gravity should be measured before spring stiffening occurs, as explained in the beginning of this section.

Combining the total force F_{tot} on the proof mass (equation 3.41), the displacement δ where spring stiffening starts (equation 3.46), and the gravity F_g acting on the proof mass.

$$F_g = F_{tot} \tag{3.47}$$

where

$$F_g = mg \qquad F_{tot} = \frac{3nE\delta(20I + \delta^2 A)}{5L^3(1-\nu^2)} \qquad \delta < \sqrt{\frac{5}{9}}w \tag{3.48}$$

Solving this equation yields the critical mass m_v for the restraint for orientation independence of the device.

$$m_v < \frac{4nE\sqrt{5}w^4 t}{9gL^3(1-\nu^2)} \tag{3.49}$$

3.3.5 Buckling

When operating in vertical operation, the risk of buckling might occur in the spring below the proof mass, which is illustrated in figure 3.10. The problem with buckling is that the behavior of the sensor becomes unpredictable and that the sensor in that case is not very useful as a (sensitive) sensor anymore.

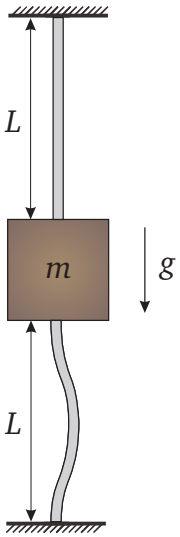

Figure 3.10: *Illustration of buckling effects.*

It is possible to find some criteria for which the device will not buckle. From Hibbeler [2] the critical force S_{cr} exerted on the beam in the axial-direction when buckling will start to occur can be calculated, where E is the Young's modulus, I the moment of inertia, ν Poisson's ratio, K the buckling factor and L the length of the beam.

$$S_{cr} = \frac{\pi^2 EI}{(KL)^2(1-\nu^2)} \tag{3.50}$$

Since in this case the beam has fixed ends, the buckling factor K becomes equal to 0.5.

$$S_{cr} = \frac{4\pi^2 EI}{L^2(1-\nu^2)} \tag{3.51}$$

The axial force S is in this case equal to a part of the gravity force acting on the proof mass m, with gravitation acceleration g. Since the devices consists of n beams, this leads to

$$S = \frac{mg}{n} < S_{cr} \tag{3.52}$$

Combining these equations will give us a restraint for designing the sensor, wherein the mass m and the length L can be varied.

$$mL^2 < \frac{n\pi^2 E t w^3}{3g(1-\nu^2)} \tag{3.53}$$

3.3.6 Stress

To investigate whether designs are feasible for production, the effects of stress should be investigated. Therefore, sequentially the maximum normal stress σ and shear stress τ occurring in the device are discussed.

Normal stress

When the device is operating in *horizontal* mode, the stress in the beams is caused by the weight of the proof mass m. The associated normal stress is easily determined by

$$\sigma_h = \frac{P_g}{A} = \frac{mg}{ntw} \tag{3.54}$$

where σ_h is the normal stress in the beams, P_g the force by gravity, A the cross-sectional area of a beam, m is the size of the proof mass, g is Earth's gravitational acceleration, n is the number of beams, t is the thickness of a beam and w is the width of a beam.

Also look what will happen when the device is held in *vertical* mode. Therefore, the axial force in the beams caused by the weight of the proof mass due to Earth's gravity needs to be calculated. First, the normal stress in the beams is defined and related to the force by gravity using equation 3.36.

$$\sigma_v = \frac{S}{A} = \frac{P_g L}{n\delta A} \tag{3.55}$$

From equation 3.37 the relationship between the force P_g and the deflection δ is determined.

$$\delta = \sqrt[3]{\frac{5L^3 P_g(1-\nu^2)}{3nAE}} \tag{3.56}$$

Combining these two expression yields the relation between the weight of the proof mass P_g in horizontal mode and the normal stress σ_v in the beams.

$$\sigma_v = \sqrt[3]{\frac{3Em^2g^2}{5n^2A^2(1-\nu^2)}} \tag{3.57}$$

From this can be concluded that the stress in the beams can be reduced by choosing another material (lower Young's modulus E), increasing the cross-sectional area A, increasing

the number of beams n, and reducing the size of the proof mass m. However, doing so will decrease sensitivity of the system.

Bending stress

Although the behavior of the beams is described by bending theory, it is interesting to look at the effects on bending when the beam would not deform over its length. From this the stress by bending at the suspension can be found, which is also a design criteria. The bending stress σ_b is defined as

$$\sigma_b = \frac{Mc}{I} \tag{3.58}$$

where M is the moment acting at the suspension, c is the perpendicular distance from the neutral axis to a point farthest away from it and I and is the moment of inertia. In this case, define c as half of the thickness of the beam, I as before, the moment M as the force P_g multiplied by the length of the beam L and n the number of beams.

$$c = \frac{w}{2} \qquad I = \frac{tw^3}{12} \qquad M = \frac{P_g L}{n} \tag{3.59}$$

Combining these expression yields the expression for determining the associated bending stress at the suspension σ_b, which will be lower in reality. Nevertheless, this leads to good design criteria.

$$\sigma_b = \frac{6mgL}{nw^2t} \tag{3.60}$$

As expected, a lower mass m and a shorter beam with length L reduce the stress at the suspension. Also, the width w and the thickness t of the beam might be increased for less stress. Again, remark the trade-off between robustness en sensitivity of the system.

Note that the mass might also move in the direction of the thickness t. To calculate the associated stress effects, it is just a matter of swapping the variables t and w.

3.4 Characteristics

The mass m and the spring (constant) K have been closely investigated. From here, the behavior of the system should be investigated for gravitational accelerations, regarding both its static and dynamic behavior.

Therefore, use the expression for the differential equation describing a second order mass-spring system with damping using the sum of forces, which has already been given in equation 2.23. It is however more convenient to write this for an applied gravitational acceleration g, resulting in equation 3.61.

$$\frac{d^2x}{dt^2} + \frac{\gamma}{m}\frac{dx}{dt} + \frac{K}{m}x = g \tag{3.61}$$

Using LaPlace's transformation, the system can be also described with a second order mechanical transfer function from acceleration to displacement considering the mass m, as is given below.

$$H(s) = \frac{X(s)}{G(s)} = \frac{1}{s^2 + \frac{\gamma}{m}s + \frac{K}{m}} = \frac{1}{s^2 + \frac{\omega_r}{Q}s + \omega_r^2} \tag{3.62}$$

where the quality factor Q and the resonance frequency ω_r are defined as

$$Q = \frac{\omega_r m}{\gamma} \qquad \omega_r = \sqrt{\frac{K}{m}} \tag{3.63}$$

Although the term resonance frequency suggests that the device will have it largest displacement at frequency ω_r, this is not the case when there is sufficient damping of the device. Considering the quality factor Q, the oscillation frequency ω_o (for harmonic accelerations) of the system is given in the equation below [5].

$$\omega_o = \omega_r \sqrt{1 - \frac{1}{4Q^2}} \tag{3.64}$$

The difference in frequency $\Delta\omega$ between oscillation and resonance can then be expressed as

$$\Delta\omega = \omega_r - \omega_o = 1 - \sqrt{1 - \frac{1}{4Q^2}} \approx \frac{1}{8Q^2} \tag{3.65}$$

As can be seen from this approximation, the difference $\Delta\omega$ decreases with 20 dB per decade. Note that this investigation is only valid when the quality factor Q of the system is larger than 0.5 (underdamped system). The difference is visualized in figure 3.11, from which can also deduced that the effect of $\Delta\omega$ is negligible for quality factors of 5 or higher.

Because the quality factor of accelerometers with relatively large proof masses are generally larger than 5 [6], the effect of change in oscillation frequency is neglected and therefore

$$\omega_o \approx \omega_r \tag{3.66}$$

Since most gravity measurements are done for very low frequencies, consider the transfer function given in equation 3.62 and use the fact the every term consisting of s will drop out, resulting in

$$x = \frac{g}{\omega_r^2} \tag{3.67}$$

where x is the displacement, g is the gravitational acceleration and ω_r is the resonance frequency of the system. Notice that this implies a trade-off between sensitivity and bandwidth. Luckily, most gravity measurements require very little bandwidth, making it possible to focus the design on sensitivity.

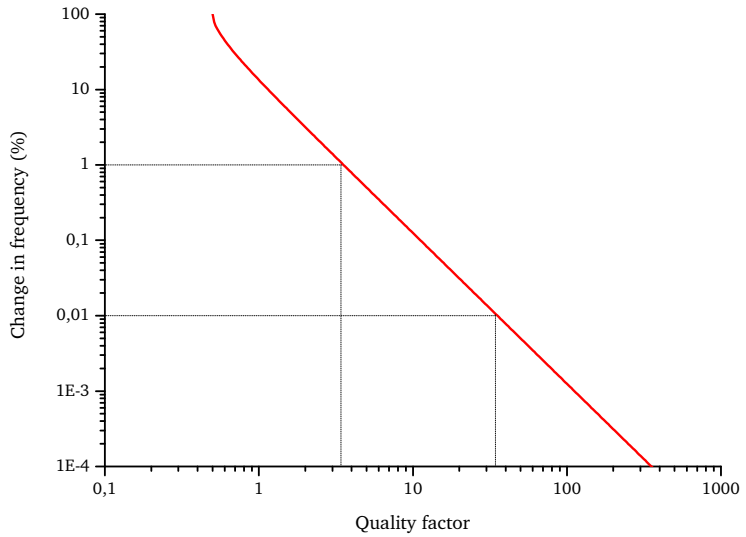

Figure 3.11: *Effect of quality factor on the oscillation frequency.*

3.4.1 Sensitivity

Since very small changes in gravity should be measured, a way of maximizing sensitivity of the sensor needs to be determined. With the use of equations 3.15 and 3.67 and the fact that a number of beams n is used, the sensitivity dx/dg can be rewritten to

$$\frac{dx}{dg} = \frac{1}{\omega_r^2} = \frac{m}{K} = \frac{mL^3(1-\nu^2)}{12nEI} \tag{3.68}$$

However, several design restraints do not allow to increase both mass m and L too much. It is especially interesting to look at the restraint by buckling, as discussed in section 3.3.5. Using the resulting expression for this restraint, the maximum obtainable sensitivity for the system is

$$\frac{dx}{dg} \leq \frac{\pi^2 L}{3g_0} \tag{3.69}$$

where L is the length of a beam and g_0 is Earth's gravitational acceleration. It can now be clearly seen that changing the mass m will not result in a better maximum sensitivity, but increasing the length L does. From this criteria, the sensor should be designed in such a way that the length L is as long as possible.

3.4.2 Modal analysis

In the previous paragraphs the presence of a resonance frequency ω_r in the system was already mentioned. However, it is very likely that there are more than one resonance frequencies present. In other words, the accelerometer system will have several modes.

When looking carefully at the system, three significant modes can be expected. Since the beams have a thickness t which is not deviating much from their width w, they should have a resonance frequency in both directions (mode 1 and 2). A third mode (3) is instead of translation in the x or y-direction rotation in the xy-plane. Because the system is built in such a way that Earth's gravity in the z-direction is resisted, the modes with the z-direction involved are neglected, because the associated spring constant K_z is such high that movement of the mass is almost impossible.

Mode 1 – Translation in x-direction

The first mode of the system is a result of the resonance frequency in the desired x-direction. Indeed, the beams are designed to have a small width w compared to a bit larger thickness t to ensure the largest movement in that direction. This mode is visualized in figure 3.12, where the spring-equivalents from the beams are given. Note that this is a *top view* of the sensor, meaning that Earth's gravity is pointing into the paper.

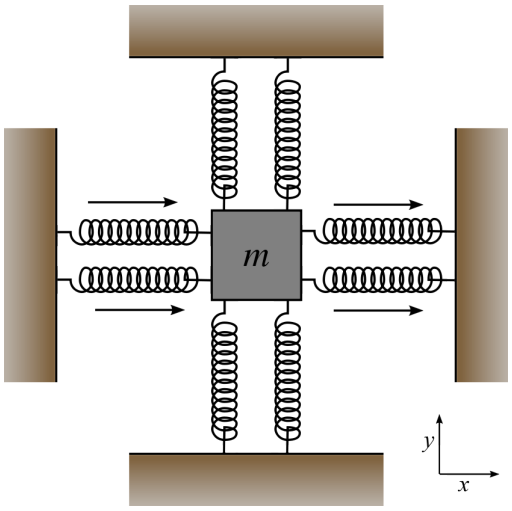

Figure 3.12: *Mode 1 – Translation in x-direction.*

To calculate the associated resonance frequency $\omega_{x,t}$ in the x-direction, first the moment of inertia I_x of the beams is defined by means of the expression below.

$$I_x = \frac{tw^3}{12} \tag{3.70}$$

The spring constant K_x of one beam is then given by the following equation (see also equation 3.15).

$$K_x = \frac{12EI_x}{L^3(1-\nu^2)} \tag{3.71}$$

From the previous theory the resonance frequency $\omega_{x,t}$ is found in terms of the number of beams n, its thickness t, its width w, its length L, the Young's modulus E of the material,

the Poisson's ratio ν and the proof mass size m.

$$\omega_{x,t} = \sqrt{\frac{nK_x}{m}} = \sqrt{\frac{ntw^3E}{mL^3(1-\nu^2)}} \tag{3.72}$$

Mode 2 – Translation in y-direction

For the second mode a similar approach is used. Therefore, a schematic drawing of the resonance in the y-direction is given in figure 3.13.

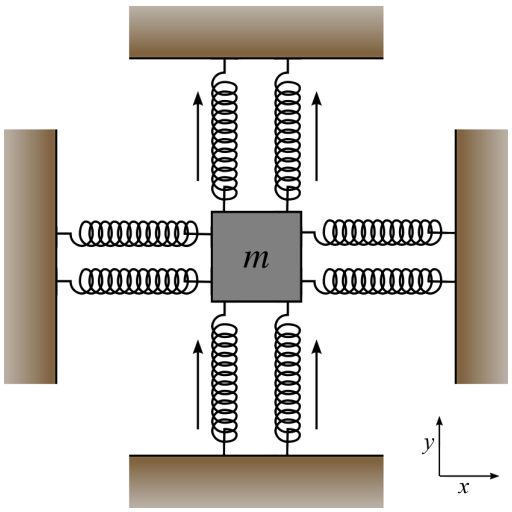

Figure 3.13: *Mode 2 – Translation in y-direction.*

Finding the resonance frequency starts with determining the moment of inertia in the y-direction, consisting of the thickness t of the beam and the width w of the beam.

$$I_y = \frac{wt^3}{12} \tag{3.73}$$

This leads to the spring constant K_y in the y-direction for one beam as

$$K_y = \frac{12EI_y}{L^3(1-\nu^2)} \tag{3.74}$$

For n beams the resulting resonance frequency $\omega_{y,t}$ in the y-direction becomes

$$\omega_{y,t} = \sqrt{\frac{nK_y}{m}} = \sqrt{\frac{nwt^3E}{mL^3(1-\nu^2)}} \tag{3.75}$$

This can be rewritten to

$$\omega_{y,t} = \left(\frac{t}{w}\right)\omega_{x,t} \tag{3.76}$$

Note this interesting result, because the second mode is just the ratio of the thickness t and the width w of the beam with respect to the resonance frequency $\omega_{x,t}$ in the x-direction.

Mode 3 – Rotation in xy-plane

The third mode lies within the rotational domain and is more complicated to find then the two modes described before. First, a schematic view of this mode is given in figure 3.14. Notice that here four springs are compressed (two in x-direction and two in y-direction) and four springs are elongated (idem), as indicated by the arrows.

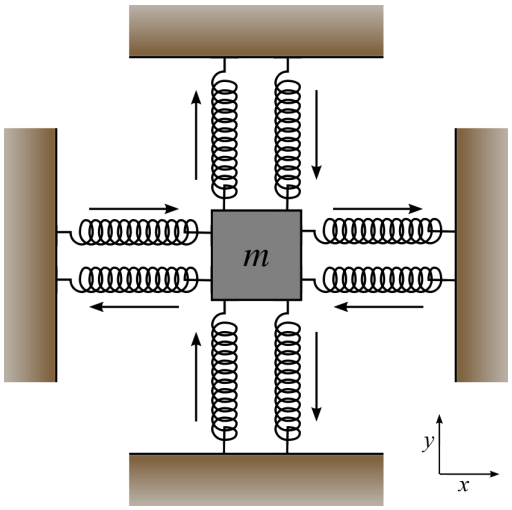

Figure 3.14: *Mode 3 – Rotation in xy-plane.*

The resonance frequency $\omega_{xy,r}$ of a system in the rotational domain is generally given by the following equation, where K_{xy} is the rotational spring constant and J_{xy} is the rotational moment of inertia [5].

$$\omega_{xy,r} = \sqrt{\frac{K_{xy}}{J_{xy}}} \tag{3.77}$$

For this accelerometer, the rotational moment of inertia J_{xy} is given by

$$J_{xy} = \frac{m}{12}\left(t_{Si}^2 + w_{Si}^2\right) \tag{3.78}$$

where m is the size of the (equal density) proof mass, t_{Si} is the thickness (y-direction) and w_{Si} is the width (x-direction) of the silicon.

Before calculating the spring constant K_{xy} in the rotational domain, another drawing is given in figure 3.15. Here, a simplistic view is given about the proof mass m which is rotated over an angle α.

Although the rotational spring constant K_α is not known, it is possible to derive it from the spring constants K_x and K_y. Therefore, a look at figure 3.16 is desired. In this figure two cuts are given from figure 3.15, wherein the width w_{Si} and the thickness t_{Si} of the proof mass are given, combined with the force F by the spring(s) in x- and y-direction.

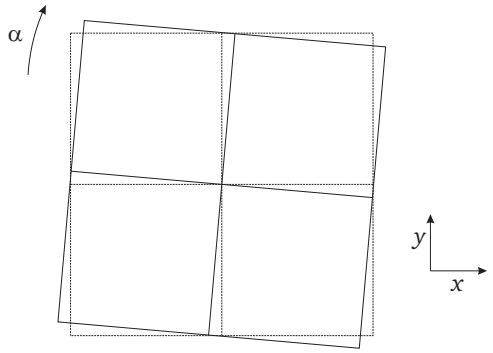

Figure 3.15: *Rotation of the mass in the xy-plane.*

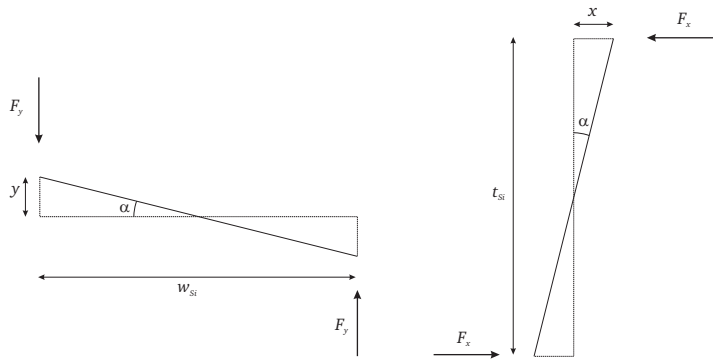

(a) *In the y-direction.* **(b)** *In the x-direction.*

Figure 3.16: *Determining the spring constant for the rotational domain.*

A spring constant K_r in the rotational domain is generally given by

$$K_r = \frac{dT}{d\alpha} \tag{3.79}$$

where T is the torque exerted by the spring and α is the associated angle.

First, have a look at the effect of the springs in the y-direction. Using figure 3.16, it is possible to determine both the torque T and the angle α for small angles of α from the force F_y, the width w_{Si} of the proof mass and the displacement y in the y-direction.

$$T = \left(\frac{w_{Si}}{2}\right) F_y \qquad \alpha = \tan\left(\frac{2y}{w_{Si}}\right) \approx \frac{2y}{w_{Si}} \tag{3.80}$$

The associated rotational spring constant $K_{r,xy}$ is then determined by combining the two previous equations, eventually relating the spring constant K_y to the one in the rotational domain (for one beam) $K_{r,y}$.

$$K_{r,y} = \frac{dT}{d\alpha} \approx \left(\frac{w_{Si}}{2}\right)^2 \frac{dF_y}{dy} = \left(\frac{w_{Si}}{2}\right)^2 K_y \tag{3.81}$$

A similar approach can be used for the x-direction, which yields for the rotation spring constant $K_{r,x}$ in the x-direction, where t_{Si} is the thickness of the proof mass and K_x is the spring constant of one beam in the x-direction.

$$K_{r,x} \approx \left(\frac{t_{Si}}{2}\right)^2 K_x \tag{3.82}$$

The total (equivalent) spring constant for the rotational domain K_{xy} is eventually found by taking in account the number of beams n and summing the contributions by both directions.

$$K_{xy} = n\left(K_{r,x} + K_{r,y}\right) = \frac{n}{4}\left(K_x t_{Si}^2 + K_y w_{Si}^2\right) \tag{3.83}$$

Now that both the rotational spring constant $K_{r,xy}$ and the moment of inertia J_{xy} are known, the resonance frequency $\omega_{xy,r}$ can be found.

$$\omega_{xy,r} = \sqrt{\frac{K_{xy}}{J_{xy}}} = \sqrt{\frac{3n\left(K_x t_{Si}^2 + K_y w_{Si}^2\right)}{m\left(t_{Si}^2 + w_{Si}^2\right)}} \tag{3.84}$$

For masses which have a width w which is much larger than its thickness t and a spring constant K_y which is larger than K_x, the previous expression can be approximated for the resonance frequency $\omega_{xy,r}$ by

$$\omega_{xy,r} \approx \sqrt{\frac{3nK_y}{m}} = \sqrt{3}\omega_{y,t} \tag{3.85}$$

3.4.3 Noise

The system itself will not be free of noise. In mass-spring systems noise is usually dominated by (white) thermal noise of the proof mass (by Brownian motion), which is better known to be described by its spectral density and the associated Total Noise Equivalent Acceleration (TNEA), given with a_n by the expression below [7].

$$\sqrt{\overline{a^2}_n} = \sqrt{\frac{4k_B T\omega_r}{Qm}} \qquad \left[\mathrm{m/s^2/\sqrt{Hz}}\right] \tag{3.86}$$

Here, k_B is the constant of Boltzmann ($1.381 \cdot 10^{-23}$ J/K), T is the temperature of the system, ω_r is the resonance frequency of the system, Q is the quality factor and m is the size of the proof mass. It should be denoted that here the entire mechanical bandwidth is used, determined by its resonance frequency ω_r.

When applying filtering to this bandwidth, the effect of thermal noise might be reduced. Therefore, rewrite expression to a more general expression for thermal noise, where γ is the damping coefficient and $\Delta\omega$ is the bandwidth after filtering. Remark that a_n is given as Root Mean Square (RMS), since noise is a varying quantity.

$$a_n = \sqrt{\overline{a^2}_n}\sqrt{\Delta\omega} = \frac{\sqrt{4k_B T\gamma\Delta\omega}}{m} \qquad \left[\mathrm{m/s^2}\right] \tag{3.87}$$

From this can be seen that noise can be reduced by decreasing the bandwidth $\Delta\omega$, which is possible due to the fact that gravity measurements require most of time very little bandwidth ($<$ 1 Hz, see chapter 2). Note also that increasing the size of the proof mass m will decrease the noise in the measurements.

Signal-to-Noise Ratio

Since an expression for the noise has been found, this can be also formulated to an expression for the associated Signal-to-Noise Ratio (SNR). From equation 3.87 the following equation is obtained for the SNR, where the signal acceleration a_s and noise acceleration a_n are both given square, since noise is normally treated using its power spectral density.

$$SNR = \left|\frac{a_s}{a_n}\right|^2 = \frac{a_s^2 m^2}{4k_B T\gamma\Delta\omega} \tag{3.88}$$

The minimum measurable gravity is given by a SNR equal to one. From the previous equation combined with equation 3.86, a more useful expression for determining this minimum $a_{s,min}$ can be used, since it is easier to estimate a quality factor Q than the viscous damping coefficient γ.

$$a_{s,min} = \sqrt{\frac{4k_B T\omega_r\Delta\omega}{Qm}} \qquad \left[\mathrm{m/s^2}\right] \tag{3.89}$$

3.4.4 Figure of Merit

To design the sensor in such a way that high sensitivity S, high bandwidth BW and low thermal noise equivalent acceleration $TNEA$ are obtained, it requires a trade-off between the length L of the beams and the size of the proof mass m.

A possible manner to determine the so-called optimum for a MEMS design is the use of a Figure of Merit, which is a quantity used to characterize the performance of a system [8]. From the requirements given in the previous paragraph it is rather easy to find an expression for a Figure of Merit FoM for the accelerometer for geophysical applications by means of expression 3.90.

$$FoM = \frac{S^2 \cdot BW}{TNEA} \tag{3.90}$$

Here, the sensitivity S is obtained using equation 3.68, the bandwidth BW is found in expression 3.63 and the TNEA is given by equation 3.87. Notice that the sensitivity is squared, because the main purpose of the sensor is measuring very small accelerations, requiring a high sensitivity. Noise and bandwidth are also needed, but are of less importance. Using these expressions leads to a rewritten form of the previous equation for the Figure of Merit FoM.

$$FoM = \frac{\left(\frac{m}{K}\right)^2 \cdot \left(\frac{K}{m}\right)^{\frac{1}{2}}}{\frac{\sqrt{4k_B T\gamma}}{m}\left(\frac{K}{m}\right)^{\frac{1}{4}}} \tag{3.91}$$

Although this might look quite difficult, it can be simplified to the expression below.

$$FoM = \left[\frac{m^{11} L^{21} \left(1 - \nu^2\right)^7}{\left(4 k_B T \gamma\right)^2 \left(n t w^3 E\right)^7} \right]^{\frac{1}{4}} \tag{3.92}$$

Since the Figure of Merit can be defined as an arbitrary number, it means that powers on the entire entity are just a scale factor for the FoM. Looking at this Figure of Merit, one can improve the performance of the (designed) system by changing either the mass m, the length L, the number n, the width w and the thickness t of the beams. By taking the decreasing variables (n, t and w) as a starting point by minimizing them as far as possible (within reasonable technological limits), the Figure of Merit improves by the right choices regarding the length L and the mass m. Doing so, the expression for the Figure of Merit simplifies to

$$FoM = C_1 m^{11} L^{21} \approx C_2 m^3 L^5 \tag{3.93}$$

where C_1 and C_2 are certain constants, consisting of several parameters, like the Young's modulus E of the used material (silicon in this case). Notice that also a simplification is given, because high powers are not always suitable for performing calculations. Besides, the relationship between m and L is qualitative and stays approximately the same. Now the expression for the Figure of Merit is known, this can be used for designing the optimal sensor.

Though it might be expected that increasing both the length L and the mass m would result in a better sensor performance, the restraints of the system (i.e. buckling) have to be taken into account. In chapter 4 a graph of a Figure of Merit will be given, wherein can be seen that eventually the highest performance (FoM) of the system is achieved when the required sensitivity is equal to the buckling restraint. So, the Figure of Merit will help us in finding the best trade-off in the system, thus finding the 'optimal' design.

3.5 Read-out

Since the displacement of the proof mass is a measure for the gravitational acceleration, this displacement needs to be determined. Several read-out techniques are available for this purpose. Here, both the possibilities using capacitive read-out and optical read-out are discussed, because these mechanisms are very good implementable within the final design. Other mechanisms like electron tunneling read-out might be interesting, but have some limitations for this purpose, as can be found in Flokstra et al. [9].

The discussed read-out mechanisms in the next paragraphs are all capable of measuring displacements below 1 nm. Since gravitational accelerations are often lower than 1 mgal, the advised requirement for sensitivity is 1 nm/mgal. Although it is still a challenge to perform appropriate read-out for these accelerations, these techniques can be optimized to detect even smaller displacements (like [10]), to eventually measure accelerations in the order of μgal.

A brief overview of common used read-out mechanisms in realized MEMS accelerometers and their associated noise floors for displacement (resolution) of the proof mass can be found in figure 3.17. From this figure can be (also) concluded that especially capacitive and tunneling based read-out are commonly used principles.

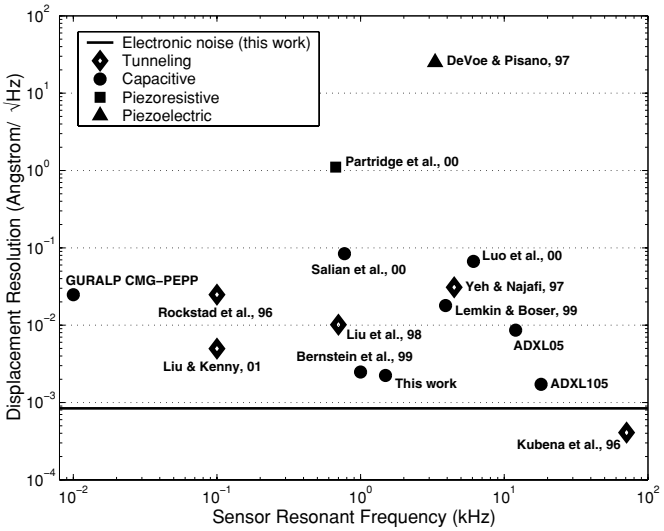

Figure 3.17: *Comparison of the read-out principles of MEMS accelerometers [11].*

3.5.1 Tunneling

Using the principle of tunneling it is possible to determine displacement of the proof mass with a resolution in the order of 0.01 pm/$\sqrt{\text{Hz}}$. The idea of tunneling is to bring a small tunneling tip within a distance of several nanometer of the proof mass. In figure 3.18 an example is given of an implementation of tunneling read-out for an accelerometer.

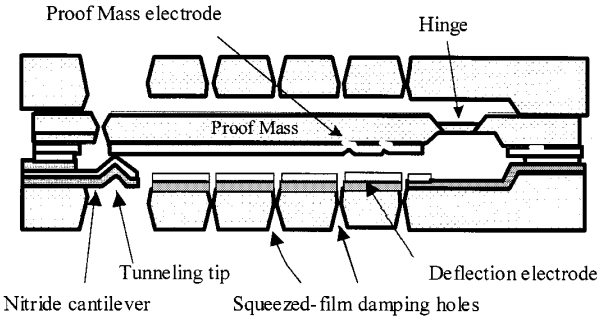

Figure 3.18: *Tunneling read-out of an accelerometer [12].*

When applying a DC bias voltage U_b between the tip and the surface (of the proof mass),

a tunneling current I_t of about 1 nA can be measured, depending on the distance as

$$I_t = U_b e^{-\alpha\sqrt{\phi h}} \tag{3.94}$$

where α is a constant, ϕ is the tunneling barrier height and h is the gap between the electrodes. For typical values of U_b (0.1 V), ϕ (0.5 eV) and h (1 nm), the tunneling current I_t doubles for every Å displacement. Some disadvantages using tunneling read-out are 1/f noise and drift of the tunneling barrier height due to contamination of the electrode surfaces [9].

3.5.2 Optical

With the use of an optical interferometer it is possible to obtain an accurate measurement of the position of a certain object. Using interference patterns very good out-of-plane distance measurements can be done, up to a resolution of $3 \cdot 10^{-3}$ Å/$\sqrt{\text{Hz}}$ [6].

The basic principle of such an interferometer is determining the intensity $I(d)$ of the diffracted modes, which can be described by

$$I(d) = I_0 \sin^2\left(\frac{2\pi d}{\lambda}\right) \tag{3.95}$$

where I_0 is a constant, d is the distance between the substrate and the (moving) object, and λ is the illumination wavelength. An example of such a setup is given in figure 3.19, consisting of a MEMS accelerometer by Loh et al. [6], a laser source and a light detector.

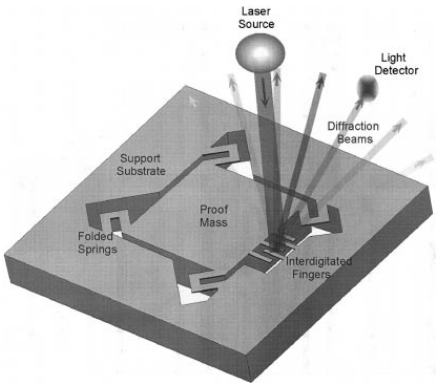

Figure 3.19: *Optical read-out of an accelerometer.*

3.5.3 Capacitive

A regularly used technique within the field of MEMS is capacitive read-out, by converting displacement to a voltage. When a parallel plate capacitor is considered, its capacitance C is given by

$$C = \frac{\epsilon A}{d} \tag{3.96}$$

where ϵ is the dielectric constant of the medium between the plates, A is the area of the plates and d is the distance between the plates. When the area A or the distance d is changed by moving one of the plates, the capacitance changes in relation to the displacement of the plate. When designing in such a way that one of the plates is the moving proof mass, its position can be determined.

There are many circuits which give an output voltage proportional to the change of the capacitance, but it is convenient to aim for a symmetric design. A proven circuit is the changing gap method used by the ADXL 50 accelerometer, which is visualized in figure 3.20 and described by Boser [13].

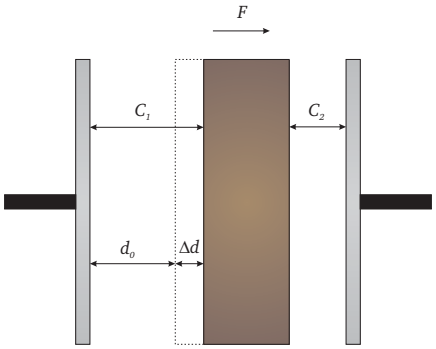

Figure 3.20: *Capacitive readout by changing gap.*

Here, the proof mass is centered, forming with the left plate capacitor C_1 and with the right plate capacitor C_2. The expressions for these capacitors with a change in displacement Δd is given by

$$C_1 = \frac{\epsilon A}{d_0 + \Delta d} \qquad C_2 = \frac{\epsilon A}{d_0 - \Delta d} \tag{3.97}$$

where ϵ is the electric permittivity (of air) and A is the surface area of the capacitor plates.

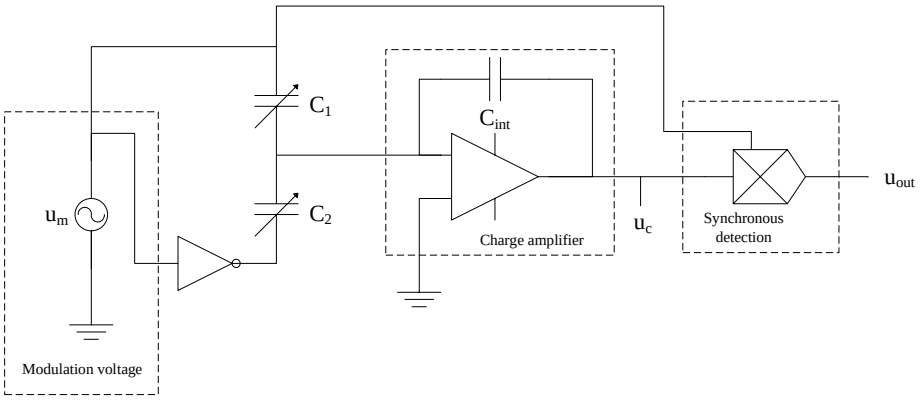

Figure 3.21: *From changing capacitances to output signal.*

Combining this with a charge amplifier setup and obtaining the circuit given in figure 3.21, the following relation exists between the change in displacement Δd and the output voltage of the charge amplifier u_c.

$$u_c = u_m \frac{C_2 - C_1}{C_{int}} \tag{3.98}$$

Before writing out the previous expression in terms of Δd, a closer look has to be taken at the difference between C_1 and C_2. In the expression below a first order approximation is made for this difference, valid for small displacements of the proof mass with respect to the nominal distance between the plates d_0.

$$C_2 - C_1 = \frac{\epsilon A}{d_0 - \Delta d} - \frac{\epsilon A}{d_0 + \Delta d} = \frac{2\epsilon A \Delta d}{d_0^2 - \Delta d^2} \approx \frac{2\epsilon A}{d_0^2} \Delta d \tag{3.99}$$

The modulation voltage u_m can be expressed as a harmonic voltage with amplitude V_m and angular frequency ω_m.

$$u_m = V_m \cos(\omega_m t) \tag{3.100}$$

Using this expression, the relation between change in displacement Δd and output voltage u_c is found.

$$u_c = V_m \cos(\omega_m t) \frac{2\epsilon A}{C_{int} d_0^2} \Delta d \tag{3.101}$$

However, the displacement of the proof mass is now modulated with an angular frequency ω_m. With the use of synchronous detection (multiplying it with a factor β of the modulation signal, where β is normally equal to 1), an output voltage u_{out} is obtained linear to the displacement Δd. Low pass filtering should be applied after synchronous detection to remove the contribution of the term with double the angular frequency ω_m.

$$u_{out} = u_m u_c = \beta V_m^2 \frac{1}{2} \left[1 + \cos(2\omega_m t)\right] \frac{2\epsilon A}{C_{int} d_0^2} \Delta d \tag{3.102}$$

With the use of equation 3.68, rewrite the expression to the sensitivity in the change in output voltage u_{out} (after low pass filtering) with respect to a change in gravity g, where m is the size of the proof mass and K is the spring constant.

$$\frac{du_{out}}{dg} = \frac{\epsilon A \beta V_m^2 m}{C_{int} d_0^2 K} \qquad \left[\mathrm{V/m/s^2}\right] \tag{3.103}$$

Spring softening

From equation 3.103 can be seen that for a high sensitivity the modulation amplitude V_m should be increased to high values. However, this will result in significant spring softening. Therefore, have a look at the energy of the system. Or better said, the co-energy E' of

the system, given by Elwenspoek and Krijnen [5], because the capacitor is actually voltage controlled by the modulation voltage u_m.

$$E' = -\frac{u_m^2 \epsilon A}{2d} \tag{3.104}$$

In this expression u is the voltage, ϵ is the dielectric constant, A is the area of the plates and d is the distance between the plates. When taking the derivative of this expression with respect to the position d_0 and keeping the modulation voltage u_m constant, the associated force F_m is obtained.

$$F_m = \left(\frac{\partial E'}{\partial d}\right)_{u_m} = \frac{\epsilon A u_m^2}{2d^2} \tag{3.105}$$

In this case one has two plates, each with its own distance between the plates with respect to the position of the proof mass. Therefore, expand the previous expression to the one below, with $F_{m,1}$ and $F_{m,2}$ the forces as result of the modulation voltage. Note that the force of the spring F_k is added, since it is also present in the (energy) system.

$$F_{m,1} = \frac{\epsilon A u_m^2}{2(d_0 + \Delta d)^2} \qquad F_{m,2} = -\frac{\epsilon A u_m^2}{2(d_0 - \Delta d)^2} \qquad F_k = K\Delta d \tag{3.106}$$

The total force caused by the modulation voltage control is then obtained by summing the forces to F_{tot} and doing a first order approximation by a Taylor expansion.

$$F_{tot} \approx -\frac{2\epsilon A u_m^2}{d_0^3}\Delta d + K\Delta d \tag{3.107}$$

The associated spring constant is obtained by differentiating again with respect to the displacement d and keeping the voltage u_m constant.

$$K_{tot} = \left(\frac{\partial F_{tot}}{\partial \Delta d}\right)_{u_m} = K - \frac{2\epsilon A u_m^2}{d_0^3} \tag{3.108}$$

Although the modulation voltage u_m is a harmonic voltage with a high frequency ω and amplitude V_m, given by

$$u_m = V_m \cos(\omega t) \tag{3.109}$$

the associated total spring constant K_{tot} is then found by

$$K_{tot} = K - \frac{2\epsilon A V_m^2 \cos^2(\omega t)}{d_0^3} \tag{3.110}$$

Using trigonometric identities, this expression can be expanded to

$$K_{tot} = K - \frac{\epsilon A V_m^2}{d_0^3} - \frac{\epsilon A V_m^2 \cos(2\omega t)}{d_0^3} \qquad [\mathrm{N/m}] \tag{3.111}$$

This is an important result, because despite the high frequency of the modulation voltage, spring softening is obtained by the virtual DC-component. The component of double the frequency is damped by the second order system, because it is much higher than the cut-off (or resonance) frequency ω_r.

A negative spring constant is not desired, since in that case the proof mass will not move to the equilibrium anymore. To calculate the so-called pull-in voltage when this effect occurs, one arrives at the following expression.

$$V_m < \sqrt{\frac{Kd_0^3}{\epsilon A}} \tag{3.112}$$

Combining these results from spring softening effects with the expression for the sensitivity of the system, found in equation 3.103, the relationship below is found.

$$\frac{du_{out}}{dg} = \frac{\epsilon A \beta V_m^2 m d_0}{C_{int}\left(Kd_0^3 - \epsilon A V_m^2\right)} \qquad \left[\mathrm{V/m/s^2}\right] \tag{3.113}$$

Although this is a useful result, consider the fact that the system might be affected by large accelerations, making the first order approximation not valid anymore. Therefore, a more detailed analysis can be found in appendix C.

When taking the deviation in voltage to be less than half (3 dB) of the maximum allowable control voltage, the minimum spring constant K_{tot} should be reduced with 1/4 of the original spring constant (6 dB), which should be enough for keeping the system stable under (process) variations, the modulation amplitude V_m can be calculated.

$$V_m = \sqrt{\frac{Kd_0^3}{4\epsilon A}} \tag{3.114}$$

and the associated maximum sensitivity

$$\left.\frac{du_{out}}{dg}\right|_{max} = \frac{md_0\beta}{3C_{int}} \qquad \left[\mathrm{V/m/s^2}\right] \tag{3.115}$$

From this result it is even more convenient to increase the size of the proof mass m as much as possible, since in that case the maximum sensitivity is increased (equation 3.115) and the Thermal Noise Equivalent Acceleration is reduced (equation 3.87).

To protect the system from extreme displacements of the proof mass, a series of bumps will be created, preventing the parallel plates to touch each other. These bumps allow the system to move at a maximum distance of d_b.

3.5.4 Using the quality factor

To increase the displacement x at a certain gravitational acceleration g, one could also make use of the quality factor Q, which is defined as

$$Q = \frac{\omega_r m}{\gamma} \tag{3.116}$$

The quality factor can be used for displacement amplification by looking first at the mechanical transfer function

$$H(s) = \frac{X(s)}{G(s)} = \frac{1}{s^2 + \frac{\omega_r}{Q}s + \omega_r^2} \tag{3.117}$$

which can be rewritten for the frequency domain as

$$H(j\omega) = \frac{1}{\left(\omega_r^2 - \omega^2\right) + j\left(\frac{\omega_r}{Q}\right)} \tag{3.118}$$

The amplitude of the displacement $|X|$ for a given gravitation $|G|$ is then

$$|X| = |G| \frac{1}{\sqrt{\left(\omega_r^2 - \omega^2\right)^2 + \left(\omega\frac{\omega_r}{Q}\right)^2}} \tag{3.119}$$

When the gravitational acceleration has a frequency ω equal to the resonance frequency ω_r, the resulting displacement amplitude becomes

$$|X| = |G| \frac{Q}{\omega_r^2} \tag{3.120}$$

Compared to the displacement of the proof mass m for 'static' ($\omega \approx 0$) gravitational accelerations, the displacement is

$$|X| = |G| \frac{1}{\omega_r^2} \tag{3.121}$$

So, the displacement of the proof mass is amplified by a factor Q. It could be interesting if this property can be used, because in most mechanical accelerometers the quality factor is larger than 1.

A possibility to do so is using the rotating disk principle described by Weits and van der Horn [14]. When the disk is rotating at an angular frequency equal to the resonance frequency ω_r, the gravitational acceleration $g(t)$ with amplitude g_0 becomes

$$g(t) = g_0 \cos(\omega_r t) \tag{3.122}$$

resulting in a displacement $x(t)$ equal to

$$x(t) = g_0 \frac{Q}{\omega_r^2} \cos(\omega_r t) \tag{3.123}$$

Of course, the displacement is now modulated, so the signal has to be demodulated by a signal with an angular frequency ω_r. Another advantage of this methodology is the suppression of noise and common mode rejection when using multiple accelerometers, as described in chapter 2. In addition, the system can be designed more robust, because a given acceleration causes a larger displacement of the proof mass, so the system can be made more stiff.

3.6 Feedback

To increase the performance of the accelerometer system force-feedback could be applied to the system, as described by Boser [15]. Doing so, drift of the sensor can be reduced, the frequency response (or bandwidth) can be changed and high quality factors can be used, because mechanical resonance can be more or less prevented by the feedback system.

A typical feedback loop is given in figure 3.22. Here, $H(s)$ is the open loop transfer function of the system, which has been already treated in section 3.4. The feedback loop is given by $G(s)$, which can be constructed in such a way for optimal system performance.

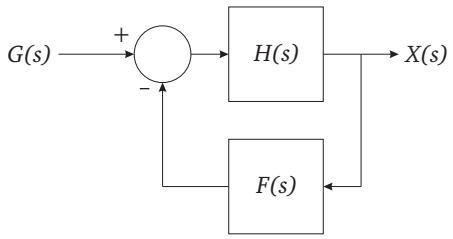

Figure 3.22: *System with a feedback loop.*

In stead of the open loop transfer $H(s)$, the closed loop transfer function is given by

$$\frac{X(s)}{G(s)} = \frac{H(s)}{1 + F(s)H(s)} \tag{3.124}$$

To investigate what happens when a constant part of the output signal is returned to the input stage, the transfer becomes

$$\frac{X(s)}{G(s)} = \frac{H(s)}{1 + CH(s)} \tag{3.125}$$

where C is an arbitrary constant. The so-called weight of this constant determines the effect of the feedback loop on the total system behavior. This is illustrated by figure 3.23, wherein several magnitudes of feedback are used.

From this figure it becomes clear that both the magnitude of the displacement at a certain force (or acceleration) and the bandwidth ('resonance' frequency) can be changed by the constant C.

In case of such a first order feedback system the product of 'sensitivity' (displacement of the proof mass) and the bandwidth is constant. It is possible to express both this mechanical transfer S and bandwidth ω_r in terms of open loop (no feedback) transfer and the feedback constant C.

$$\omega_{r,c} = \omega_{r,o}\,(1 + C) \qquad S_c = \frac{S_o}{1 + C} \tag{3.126}$$

Of course, it is more interesting to apply a more complex type of feedback $F(s)$ to improve system characteristics for the desired application. This can be done both in the analog domain and the digital domain, which will be explained in the next subsections.

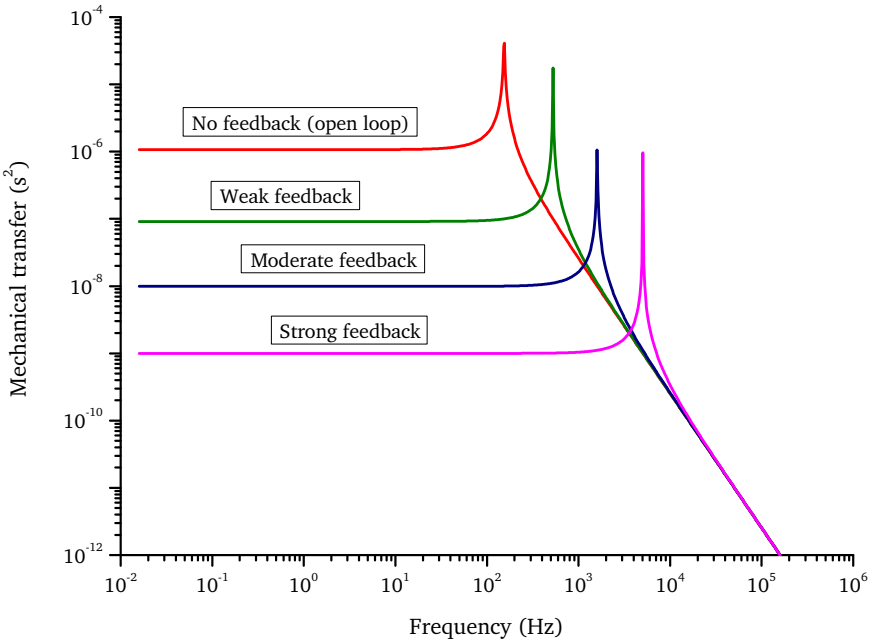

Figure 3.23: *Illustration of the effect of feedback on the system.*

3.6.1 Analog feedback

To ensure a well-described behavior of the feedback system by analytical methods and a fast response to the system without a so-called dead-zone, one could use analog feedback to implement the feedback loop $F(s)$, as illustrated in figure 3.24, where the output voltage is given by $U(s)$. First, some main transfer functions will be discussed for $F(s)$ and their effect on the total mechanical transfer of the system.

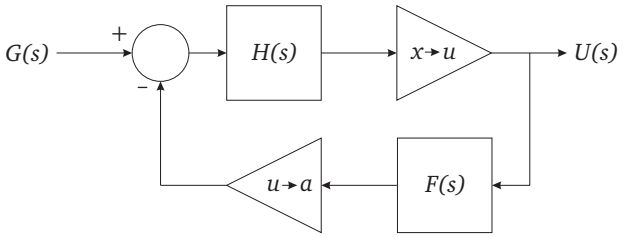

Figure 3.24: *System with an analog feedback loop.*

Common transfer functions

For a desired system behavior the feedback loop $F(s)$ is generally a quite complex function. For instance, when someone would like to remove the peak generated by the quality factor, but wants to keep the other system properties unchanged, the required transfer function $F(s)$ is usually complex, consisting of multiple zeros and poles and can be found only

numerically by using dedicated software.

Here, some common transfer functions are described and their effect of the equivalent transfer of the system. Note that this is done for getting an idea about the effect of implementation choices on the total system behavior and increasing the feeling about creating the design of the feedback loop.

For this purpose five types of transfer functions are used, namely a proportional transfer $F_1(s)$, a low pass filter $F_2(s)$, a high pass filter $F_3(s)$, a integration network $F_4(s)$ and a differentiation network $F_5(s)$. The associated expressions are given below in equation 3.128, where n is the order of the system, α is a scaling constant and τ is the time constant, defined in equation 3.127, where ω_c is the cut-off frequency of the transfer function.

$$\tau = \frac{1}{\omega_c} \tag{3.127}$$

$$F_1(s) = K \qquad F_2(s) = K\left(\frac{1}{s\tau+1}\right)^n \qquad F_3(s) = K\left(\frac{s\tau}{s\tau+1}\right)^n \tag{3.128}$$

$$F_4(s) = K\left(\frac{s\tau+1}{s\tau\alpha+1}\right)^n \qquad F_5(s) = \frac{K}{\alpha^n}\left(\frac{s\tau\alpha+1}{s\tau+1}\right)^n$$

The associated transfer curves are given in figure 3.25, wherein the cut-off frequency ω_c for all functions is chosen the same, namely equal to the resonance frequency ω_r of the accelerometer with no feedback applied.

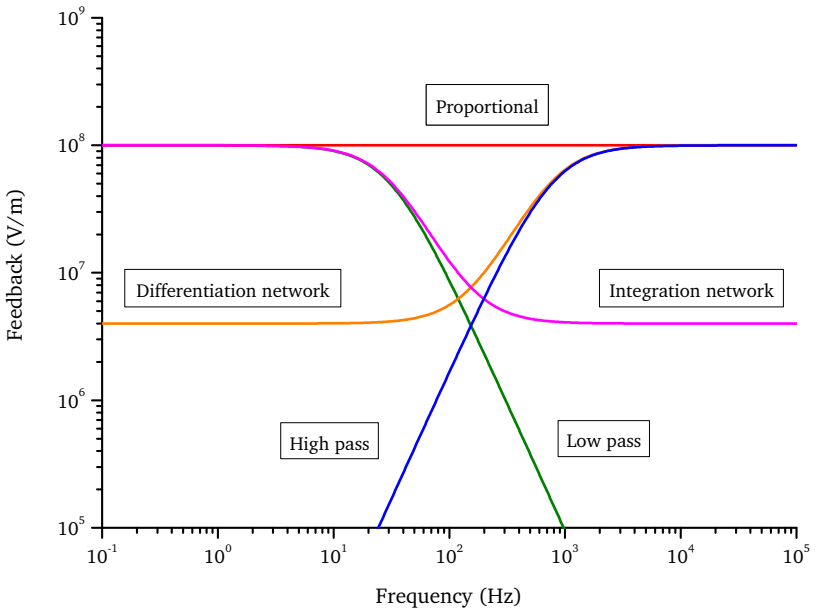

Figure 3.25: *Several types of filters for feedback implementation.*

The effect of these transfer functions on the total transfer function of the system is illustrated in figure 3.26.

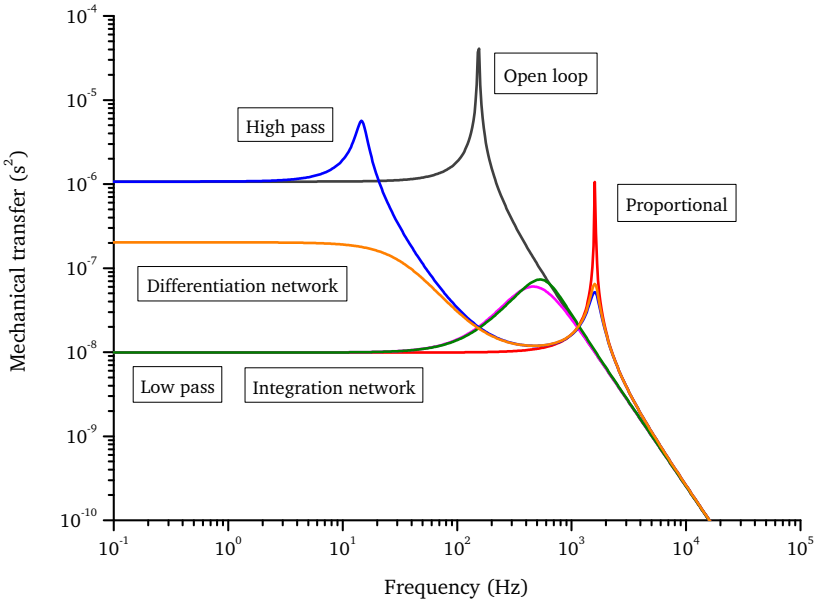

Figure 3.26: *The effect of filter types on the total mechanical transfer.*

In this figure can be seen that applying a proportional feedback has the effect described before, namely shifting the resonance frequency to a higher value and decreasing the movement of the mass by a certain factor. Both the low pass filter and the integration network show the same behavior by reducing the transfer significantly for lower frequencies. Also the effect of resonance is decreased, since the peak of the quality factor is less high and sharp.

Applying a high pass filter results in two peaks in the system, namely one below and one above the original open loop resonance frequency ω_r. When one would like to remove the effect of the resonance peak, but keeping the other system properties as much as possible in tact, a *differentiation network* should be used. Indeed, there is a small resonance peak present, but the magnitude of this peak lies below the magnitude of the transfer function for low frequencies, meaning that resonance does not cause the largest movement in the system by a given amplitude of acceleration.

Denote that in this consideration arbitrary values for the transfer function parameters are used. By adjusting these, better system characteristics can be achieved. Of course, like said before, one could gain major improvements by either combining transfer functions and/or using more complicated transfer functions to get the desired system performance.

Stability

To ensure that the system is stable when applying (negative) feedback, this aspect should be taken into account when designing the feedback loop. In the previous part only the magnitude of the transfer function was treated, but there is of course also an interesting change in phase ϕ of the signal. This change in phase is important for designing the feedback loop. From [16] it is known that the product of the mechanical transfer function $H(s)$ and

the feedback loop $F(s)$ should behave for every frequency ω under the condition given in equation 3.129.

$$H(s)F(s) > -1 \tag{3.129}$$

This means that when the product of the feedback loop is pure real (no imaginary part) and smaller than -1, the displacement of the proof mass is increased instead of reduced, leading to oscillation of the proof mass (positive feedback). This is unintended, since it makes the system behaving 'uncontrolled' and the sensor can not be used anymore for measuring small changes in gravity.

3.6.2 Digital feedback

Instead of using analog feedback with a feedback function $F(s)$, one could decide to apply digital feedback by means of Sigma-Delta modulation, as is explained by Boser [15]. A schematic view of such a system is given in figure 3.27, wherein can be seen that a part of the system is digitalized using a Analog-to-Digital Converter (ADC) toward a digital output signal $D(z)$ and made 'analog' for feedback using a Digital-to-Analog Converter (DAC). Note that the output signal $D(z)$ is digital (and modulated), requiring a decimation filter to obtain the measured quantity.

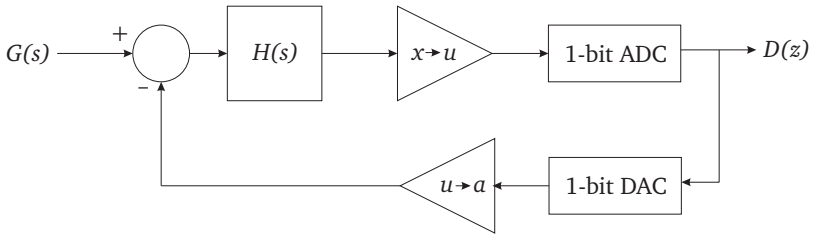

Figure 3.27: *System with a digital feedback loop.*

The principle of Sigma-Delta modulation is to apply periodically (determined by the sample frequency f_s of the converters) either a 'strong' positive or negative force on the proof mass, thus acceleration, and combined with the right modulation of this two-valued force, the position of the proof mass can be controlled. Sigma-Delta conversion of an analog signal can be viewed as Pulse Width Modulation (PWM), as is illustrated by figure 3.28.

A great benefit of applying this type of digital feedback is the excellent linearity obtained regarding the system behavior. Some disadvantages of this method are the presence of quantization noise (by the ADC), residual motion (the proof mass will displace despite the strong feedback) and a dead zone (minimum input detection), which can all be reduced by increasing the sample frequency f_s.

3.6.3 Voltage to force conversion

Now that the main analysis on feedback is done, it is important to know how this feedback can be applied. In other words, the output voltage of the system, given by $H(s)$, should

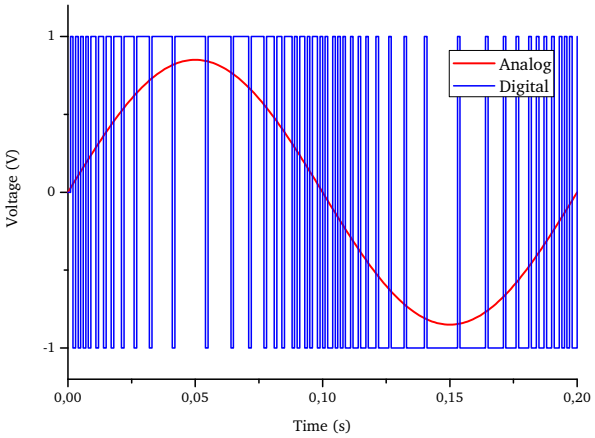

Figure 3.28: *Sigma-Delta modulation of an analog signal.*

be converted to a feedback force F_{fb} (or acceleration a). A voltage to force (thus acceleration) conversion can be done using capacitive structures in the system. First, the sensing capacitors (see figure 3.20) can be used for controlling the position of the proof mass. Also, additional capacitive structures can be constructed to control the position in another way.

Capacitive forces using changing gap

When the changing gap capacitance construction is considered used for capacitive read-out, a feedback force F_{fb} should be applied as given in figure 3.29.

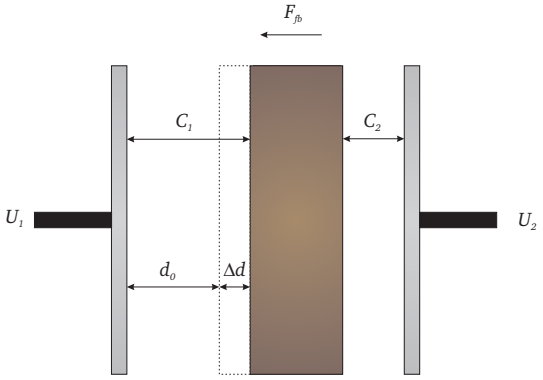

Figure 3.29: *Electrostatic force-feedback by changing gap.*

To calculate the associated feedback force, the Legendre transform is used for both capacitors, to determine the relation to the voltage U. So, first the co-energy E_1' and E_2' of both capacitors is calculated.

$$E_1' = -\frac{1}{2}U_1^2 C_1 \qquad E_2' = -\frac{1}{2}U_2^2 C_2 \tag{3.130}$$

The capacitance of the capacitor C_1 and C_2 is then given by

$$C_1 = \frac{n\epsilon A}{(d_0 - d_\Delta)} \qquad C_2 = \frac{n\epsilon A}{(d_0 + d_\Delta)} \tag{3.131}$$

where n is the number of capacitors, ϵ is the electrical permittivity, A is the surface area of the (parallel) plates, d_0 is the nominal distance between the plates and d_Δ is the changing in distance.

When the voltages U_1 and U_2 are given by a bias voltage component U_b and a feedback voltage component U_f, and the knowledge is used that the proof mass is virtually grounded, the voltages over the capacitors are defined as

$$U_1 = U_b - U_f \qquad U_2 = U_b + U_f \tag{3.132}$$

the co-energy expressions become

$$E_1' = -\frac{1}{2}(U_b - U_f)^2 C_1 \qquad E_2' = -\frac{1}{2}(U_b + U_f)^2 C_2 \tag{3.133}$$

from which the associated forces F_1 and F_2 can be calculated

$$F_1 = \left(\frac{\partial E_1'}{\partial d_\Delta}\right)_{U_1} \qquad F_2 = \left(\frac{\partial E_2'}{\partial d_\Delta}\right)_{U_2} \tag{3.134}$$

which can be evaluated to

$$F_1 = -\frac{1}{2}\frac{n\epsilon A(U_b - U_f)^2}{(d_0 - d_\Delta)^2} \qquad F_2 = -\frac{1}{2}\frac{n\epsilon A(U_b + U_f)^2}{(d_0 + d_\Delta)^2} \tag{3.135}$$

The total feedback force F_{fb} is the sum of these two forces[2], where the direction of the forces should be taken into account.

$$F_{fb} = F_1 - F_2 = -\frac{1}{2}\frac{\epsilon A(U_b - U_f)^2}{(d_0 - d_\Delta)^2} + \frac{1}{2}\frac{\epsilon A(U_b + U_f)^2}{(d_0 + d_\Delta)^2} \tag{3.136}$$

Since the proof mass will mainly move around its initial position[3], a first order Taylor expansion can be used to determine the sensitivity of the feedback (i.e. the feedback force given a certain feedback voltage) and the effective spring constant by the bias voltage. The sensitivity of the feedback S_{fb} is found using the force F_{fb} for U_f around zero displacement d_Δ of the proof mass.

$$F_{fb} \approx -\frac{2n\epsilon A U_b}{d_0^2} U_f \tag{3.137}$$

The sensitivity S_{fb} is found by differentiating this force with respect to the feedback voltage U_b.

$$S_{fb} = \frac{\partial F_{fb}}{\partial U_f} = -\frac{2n\epsilon A U_b}{d_0^2} \qquad [\mathrm{V/m}] \tag{3.138}$$

[2]The total force is also found by summing the co-energies and then taking the derivative of it instantaneously.
[3]For relative large movements a more detailed discussion is given in appendix C.

This means by increasing the area A of the plates, decreasing the gap d_0 and increasing the bias voltage U_b, the sensitivity can be increased.

The associated effect of spring softening can be found in a similar way. First, the force F_{fb} is approximated with respect to d_Δ around zero feedback voltage U_f.

$$F_{fb} \approx \frac{2n\epsilon A U_b^2}{d_0^3} d_\Delta \tag{3.139}$$

Differentiating again with respect to the displacement d_Δ, a certain spring constant K_{fb} can be found, which results eventually in spring softening.

$$K_{fb} = \frac{\partial F_{fb}}{\partial d_\Delta} = \frac{2n\epsilon A U_b^2}{d_0^3} \qquad [\mathrm{N/m}] \tag{3.140}$$

This means that feedback might also result in pull-in, when for instance a too large bias voltage U_b is used. Therefore, when applying feedback using the sense capacitors, this effect should be taken into account.

Capacitive forces using changing area

In stead of using the sense capacitors for feedback, it is also possible to add other capacitors based on the changing area method, as illustrated in figure 3.30. Here, the proof mass is allowed to move in or out between the plates of capacitors C_1 and C_2.

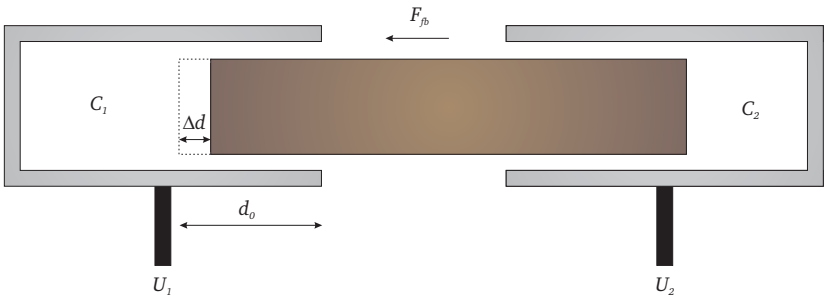

Figure 3.30: *Electrostatic force-feedback by changing area.*

To determine the behavior of this type of feedback, a similar type of analysis is used compared to the changing gap method. Therefore, first the co-energy of the system is defined as

$$E_1' = -\frac{1}{2} U_1^2 C_1 \qquad E_2' = -\frac{1}{2} U_2^2 C_2 \tag{3.141}$$

The capacitance of the capacitor C_1 and C_2 is given by

$$C_1 = \frac{\epsilon h (d_0 - d_\Delta)}{b} \qquad C_2 = \frac{\epsilon h (d_0 + d_\Delta)}{b} \tag{3.142}$$

where n is the number of capacitors, ϵ is the electric permittivity, h is the 'height' of the plates (into the paper), d_0 is the initial width of the capacitance between a plate and

the proof mass, d_Δ is the displacement of the proof mass and b is the distance between the plate and the proof mass. Notice that now the area A of the capacitors are changing and not the distance between the proof mass and the plates anymore.

The forces are found again by defining the voltages U_1 and U_2, using the knowledge that the proof mass is virtually grounded, so that the voltages over the capacitors become

$$U_1 = U_b - U_f \qquad U_2 = U_b + U_f \tag{3.143}$$

In which case the co-energy expressions become

$$E_1' = -\frac{1}{2}(U_b - U_f)^2 C_1 \qquad E_2' = -\frac{1}{2}(U_b + U_f)^2 C_2 \tag{3.144}$$

from which the associated forces F_1 and F_2 can be calculated

$$F_1 = \left(\frac{\partial E_1'}{\partial d_\Delta}\right)_{U_1} \qquad F_2 = \left(\frac{\partial E_2'}{\partial d_\Delta}\right)_{U_2} \tag{3.145}$$

which can be evaluated to

$$F_1 = -\frac{1}{2}\frac{n\epsilon h(U_b - U_f)^2}{b} \qquad F_2 = -\frac{1}{2}\frac{n\epsilon h(U_b + U_f)^2}{b} \tag{3.146}$$

Notice that the forces F_1 and F_2 are independent of the position and displacement of the proof mass, which was not the case when using the changing gap method. From this it might be expected that the spring constant by feedback is zero, as can be shown using the total feedback force F_{fb}.

$$F_{fb} = F_1 - F_2 = \frac{2n\epsilon h U_B U_f}{b} \tag{3.147}$$

Using this expression, the sensitivity of the feedback system is given by

$$S_{fb} = \frac{\partial F_{fb}}{\partial U_f} = \frac{2n\epsilon h U_B}{b} \qquad [\mathrm{V/m}] \tag{3.148}$$

where it turns out that increasing the capacitance by its height h and (reducing) distance between the plates b and increasing the bias voltage U_b improves the sensitivity S_{fb}.

More interesting is the resulting spring constant K_{fb} by this method of feedback, because it is zero. Therefore, the system will never be unstable by this type of feedback.

$$K_{fb} = \frac{\partial F_{fb}}{\partial d_\Delta} = 0 \qquad [\mathrm{N/m}] \tag{3.149}$$

From equation 3.146 it also turns out that the feedback force is always positive or negative, independent of the position of the proof mass. So, in this case the position of the bumps do not effect the behavior of the feedback system.

3.7 Conclusions

The main elements for the MEMS accelerometer for geophysical applications are a large proof mass, long and thin beams (springs) and a symmetric design over three axes. Since the springs are vital parts of the system, these are investigated in detail, regarding axial loading, spring stiffening, buckling, allowable stress and whether the sensor can be used for measuring gravity (gradient) in every direction (orientation independence).

The characteristics of the total system are described using a mechanical transfer function, in order to determine the dynamic behavior of the system. Also the modes of the sensor are investigated and its thermal noise equivalent acceleration (TNEA). Using this information, a Figure of Merit has been defined to determine the optimal design of the sensor, by considering the restraints given by buckling, allowable stress and orientation independence.

For read-out of the displacement of the proof mass, some read-out techniques are discussed, leading to the recommendation of capacitive read-out for its integratability, accuracy and other aspects. By introducing several force-feedback methods using capacitive structures, the system behavior might be improved.

References

[1] K. Gramoll. *Mechanics – Theory*. University of Oklahoma, 2009.

[2] R. Hibbeler. *Mechanics of Materials*. Prentice Hall, Singapore, Second SI edition, 2005.

[3] W. C. Young and R. G. Budynas. *Roark's Formulas for Stress and Strain*. McGraw-Hill, Seventh edition, 2002.

[4] J. Gere and S. Timoshenko. *Mechanics of Materials*. Stanley Thornes, London, Fourth SI edition, 1999.

[5] M. Elwenspoek and G. Krijnen. *Introduction to Mechanics and Transducer Science*. University of Twente, 2003.

[6] N. C. Loh, M. A. Schmidt, and S. R. Manalis. "Sub-10 cm^3 Interferometric Accelerometer With Nano-g Resolution". *Journal of Microelectromechanical Systems*, **11**(3):182–187, June 2002.

[7] T. Gabrielson. "Mechanical-thermal noise in micromachined acoustic and vibration sensors". *IEEE Trans. Electron. Devices*, **40**:903–909, 1993.

[8] J. G. Korvink and O. Paul. *MEMS – A practical guide to design, analysis and applications*. William Andrew, Norwich, New York, 2006.

[9] J. Flokstra, R. Wiegerink, H. Hemmes, and J. Sesé. "Gravity gradient sensor concepts and related technologies for planetery/lunar missions". Technical report, ESA, 2004.

[10] M.-H. Chen, S.-J. Hung, J.-H. Hsu, and M. S. Lu. "Design and Characterization of a CMOS Micromachined Capacitive Acoustic Sensor". In *6th IEEE Int. Conf. on Sensors*, pages 1148–1151, Atlanta, USA, October 2007.

[11] X. Jiang, F. Wang, M. Kraft, and B. E. Boser. "An Integrated Surface Micromachined Capacitive Lateral Accelerometer with $2\mu G/\sqrt{Hz}$ Resolution". In *Solid-State Sensor, Actuator and Microsystems Workshop*, Hilton Head Island, South Carolina, June 2–6 2002.

[12] C.-H. Liu and T. W. Kenny. "A High-Precision, Wide-Bandwidth Micromachined Tunneling Accelerometer". *Journal of Microelectromechanical Systems*, **10**(3):3, September 2001.

[13] B. E. Boser. *Capacitive Position Sense Circuits*. Berkeley Sensor & Actuation Center, 1996.

[14] H. Weits and B. van der Horn. "Investigating the accelerometer for airborne and borehole gravity gradiometry", 2009.

[15] B. E. Boser. *Electrostatic Force-Feedback*. Berkeley Sensor & Actuation Center, 1996.

[16] J. van Amerongen. *Regeltechniek*. Open Universiteit, 1990.

Chapter 4

Numerical investigation

To determine the expected behavior of the fabricated system, the theory from chapter 3 is evaluated for a specific sensor. This specific sensor has quite good sensitivity, but is also designed in such a way that it is pretty robust during fabrication and other usage. First, the theoretical part is evaluated using specific parameters. From these results, it is possible to determine the expected behavior of the produced sensor. Next, finite element calculations are done to investigate both statical and dynamical behavior of the system.

4.1 Introduction

Since many configurations are possible to analyze using both analytical and software simulation methods, one of such a configuration has to be chosen to investigate. This configuration is given by its mask design in figure 4.1. This design should be robust enough for processing, capable of measuring gravitational effects of about 1 mgal, electrical read-out (sense fingers) should be possible by the way described in chapters 3 and 5, and ready for optional electronic feedback using the changing area method (feedback fingers).

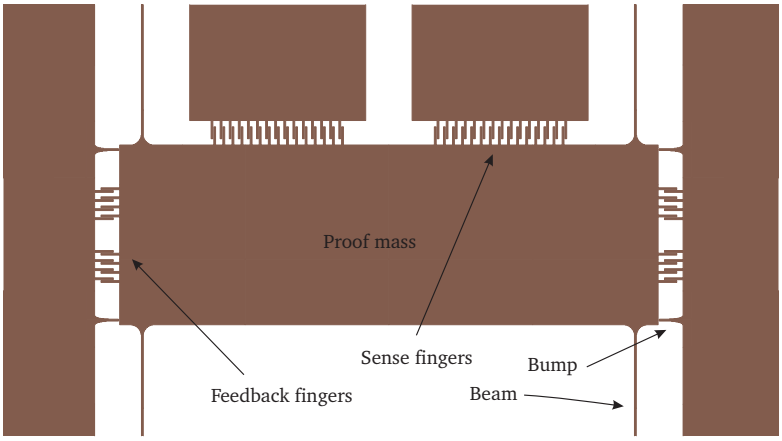

Figure 4.1: *Mask image of the sensor design for modeling.*

For this design the previous theoretical analysis will be evaluated, as also the simulation of the behavior of the system using dedicated simulation software.

4.2 Evaluation theoretical model

As a basic material for the sensor mono-crystalline silicon is used. Therefore, first some parameters for this material are given (see table 4.1).

Table 4.1: *Properties of silicon.*

Quantity	Symbol	Value	Unit
Density	ρ	2.330	g/cm^3
Young's modulus	E	150	GPa
Poisson's ratio	ν	0.28	
Wafer thickness	t_{Si}	525	μm

The next step is the dimensions of the several parts of the system. Although the system is ready for the appliance of electrostatic feedback, this part will be treated later. In table 4.2, the dimensions of the beams (width w, thickness t and length L), the aspect ratio R of the beam and the size of the proof mass m are given.

Table 4.2: *Dimensions of the accelerometer.*

Quantity	Symbol	Value	Unit
Width (beam)	w	10	μm
Thickness (beam)	t	23	μm
Length (beam)	L	2	mm
Aspect ratio (w:L)	R	1:200	
Number of beams	n	8	
Width of the mass	w_{Si}	2.94	mm
Height of the mass	h_{Si}	0.98	mm
Mass	m	3.37	mg
Bump distance	d_{bmp}	4	μm

4.2.1 Main parameters

From this the moment of inertia I_x and the cross-sectional area A can be calculated by

$$A = wt \qquad I = \frac{tw^3}{12} \tag{4.1}$$

It is also possible to calculate the spring constant K_x of one beam using

$$K_x = \frac{12EI}{L^3(1-\nu^2)} \tag{4.2}$$

Table 4.3: *More beam properties.*

Quantity	Symbol	Value	Unit
Cross-sectional area	A	230	μm^2
Moment of inertia	I_x	0.192	μm^4
Spring constant	K_x	0.397	N/m

Now that the spring constant of one beam of the system and the size of proof mass are known, it is possible to calculate the sensitivity S of the system and the bandwidth (resonance frequency) ω_r, with the knowledge that the system contains n beams. Also the sensitivity for gravity gradient G is given, where the baseline is chosen in such a way that one wafer (containing two accelerometers) can be used for gradient sensing.

Table 4.4: *System properties.*

Quantity	Symbol	Value	Unit
Sensitivity	S	10.7	pm/mgal
Baseline	b	5.0	cm
Gradient sensitivity	G	0.54	fm/E
Bandwidth	ω_r	154.6	Hz

4.2.2 Beam effects

The effect of spring stiffening can also be evaluated by means of equation 3.42. As expected from expression 3.46, the spring constant will be constant for 'low' accelerations (resulting in small displacements), but when the displacement becomes equal to about 75% of the width of the beam (i.e. 7.5 μm), spring stiffening becomes important, as can be seen in figure 4.2. Since the movement of the proof mass is limited to 4 μm by the bump distance d_{bmp}, the effect on spring stiffening is negligable.

To investigate the effect of possible buckling, the associated buckling force S_{cr} has to be calculated by means of the described in subsection 3.3.5. This force should be compared with the real force S_g in the beam due to earth's gravity.

$$S_{cr} = \frac{4\pi^2 EI}{L^2(1-\nu^2)} \qquad S_g = \frac{mg}{n} \tag{4.3}$$

Table 4.5: *Buckling investigation.*

Quantity	Symbol	Value	Unit
Critical buckling force	S_{cr}	2.62	mN
Force in beam	S_g	4.17	μN

Regarding these values, the system should not buckle. To confirm this, look also at the effect of axial stiffening and the associated influence on the spring constant. Therefore, in

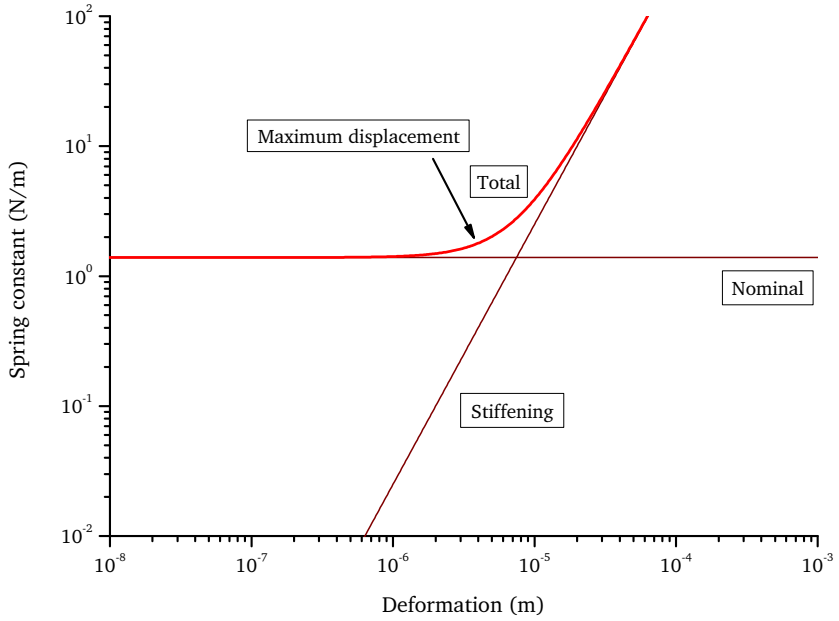

Figure 4.2: *The effect of spring stiffening for the design.*

figure 4.3 a plot is given of the spring constant of the beam for both compression and tensile stress inside. On the plot also this system is marked, confirming that the design is not in the neighborhood of the buckling area.

4.2.3 Stress

To investigate the amounts of horizontal/vertical orientation normal stress σ_h and σ_v and shear stress σ_b in the beams in an arbitrary orientation of the sensor (during fabrication it is not always oriented in the way it should be used during measurements), the expressions from subsection 3.3.6 are used. The results of the numerical evaluation of this sensor are given in table 4.6.

$$\sigma_h = \frac{mg}{ntw} \qquad \sigma_v = \sqrt[3]{\frac{3Em^2g^2}{5n^2A^2(1-\nu^2)}} \qquad \sigma_b = \frac{6mgL}{nwt^2} \tag{4.4}$$

From table 4.6 can be seen that the effect of shear stress at the position where the beam is connected to the mass and substrate is dominating in this case. This might be also expected, since the beams are rather long and small, giving a quite large torque with a small cross-sectional area of the beam.

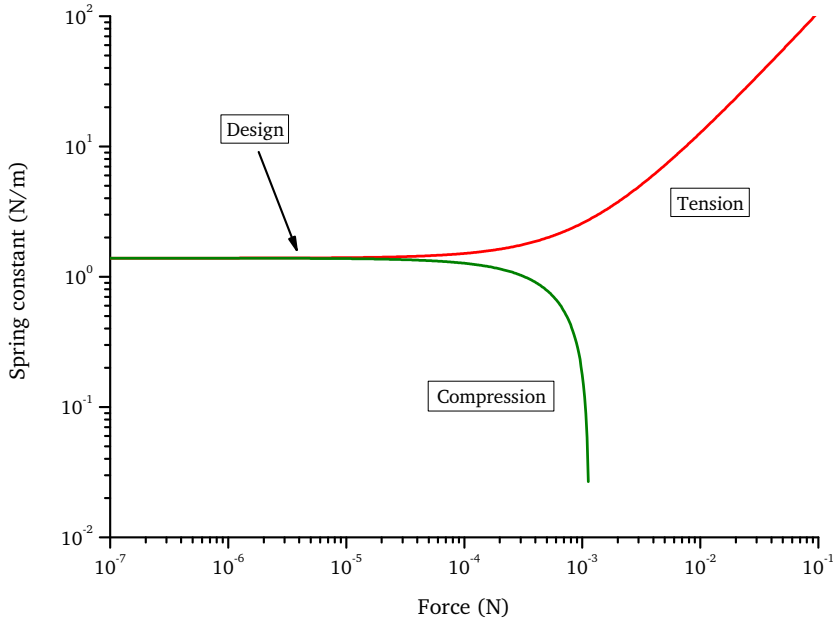

Figure 4.3: *Loading effects on the spring constant with the design included.*

Table 4.6: *Buckling investigation.*

Quantity	Symbol	Value	Unit
Normal stress (horizontal)	σ_h	18.1	kPa
Normal stress (vertical)	σ_v	0.75	MPa
Shear stress	σ_b	21.8	MPa

4.2.4 Dynamics

Using the relationships found in section 3.4, it is possible to calculate the resonance frequencies of the three described (significant) modes of the system. The first mode of the system is given in the x-direction with resonance frequency $\omega_{x,t}$, as given below.

$$\omega_{x,t} = \sqrt{\frac{nK_x}{m}} \tag{4.5}$$

The second resonance frequency $\omega_{y,t}$ is found in the y-direction.

$$\omega_{y,t} = \sqrt{\frac{nK_y}{m}} \tag{4.6}$$

where the spring constant K_y is related to K_x as

$$K_y = K_x \left(\frac{t}{w}\right)^2 \tag{4.7}$$

The value of the third resonance frequency $\omega_{xy,r}$ is more complicated to calculate, but can be evaluated for the given parameters in this chapter.

$$\omega_{xy,r} = \sqrt{\frac{3n\left(K_x t_{Si}^2 + K_y w_{Si}^2\right)}{m\left(t_{Si}^2 + w_{Si}^2\right)}} \tag{4.8}$$

An overview of this modal analysis is given in table 4.7, wherein can be seen that the resonance frequencies are quite high for geophysical applications (see chapter 2), but quite low for MEMS accelerometers [1].

Table 4.7: *Modal analysis overview.*

Quantity	Symbol	Value	Unit
Mode 1 - x-translation	$\omega_{t,x}$	154.6	Hz
Mode 2 - y-translation	$\omega_{t,y}$	355.6	Hz
Mode 3 - xy-rotation	$\omega_{r,xy}$	608.1	Hz

4.2.5 Noise

The system performance will be strongly determined by the thermal noise floor, since the accelerometer should be very sensitive. Using the expressions found in section 3.4, the Thermal Noise Equivalent Acceleration (TNEA) can be determined. The resulting values are given in table 4.8, where in the first case only the mechanical filtering is applied (bandwidth is equal to the resonance frequency $\omega_{x,r}$. Secondly, the bandwidth is reduced to 1 Hz (enough for geophysical applications) with the use of good electrical filtering and signal processing.

Table 4.8: *Thermal Noise overview.*

Quantity	Symbol	Value	Unit
TNEA noise floor	$\sqrt{\overline{a^2}_n}$	0.07	mgal/$\sqrt{\text{Hz}}$
TNEA without filtering	a_n	0.95	mgal
TNEA with filtering	a_n	0.07	mgal

From this table it can be concluded that filtering the output signal and reducing the noise is strongly recommended in order to measure gravity changes with an accuracy of 1 mgal with an acceptable Signal-to-Noise Ratio (SNR). Note that the thermal noise floor of 70 ng/$\sqrt{\text{Hz}}$ of this moderate device is comparable to the noise floor of 40 ng/$\sqrt{\text{Hz}}$ from one of the most sensitive MEMS accelerometers [2], meaning that a very low noise floor can be achieved by increasing the design performance.

4.2.6 Figure of Merit

In the theoretical analysis also a Figure of Merit was defined, consisting of the sensitivity S of the system, the bandwidth BW and the Thermal Noise Equivalent Acceleration $TNEA$. Using the present parameters the quality factor Q needs to be estimated, which is done in table 4.9. In this table also the yield strength of silicon is given by σ_Y [3].

Table 4.9: *Quality factor.*

Quantity	Symbol	Value	Unit
Quality factor	Q	50	
Yield strength	σ_Y	7	GPa

Now, the Figure of Merit can be drawn, as is done in figure 4.4. This design is indicated with an arrow in the gray area.

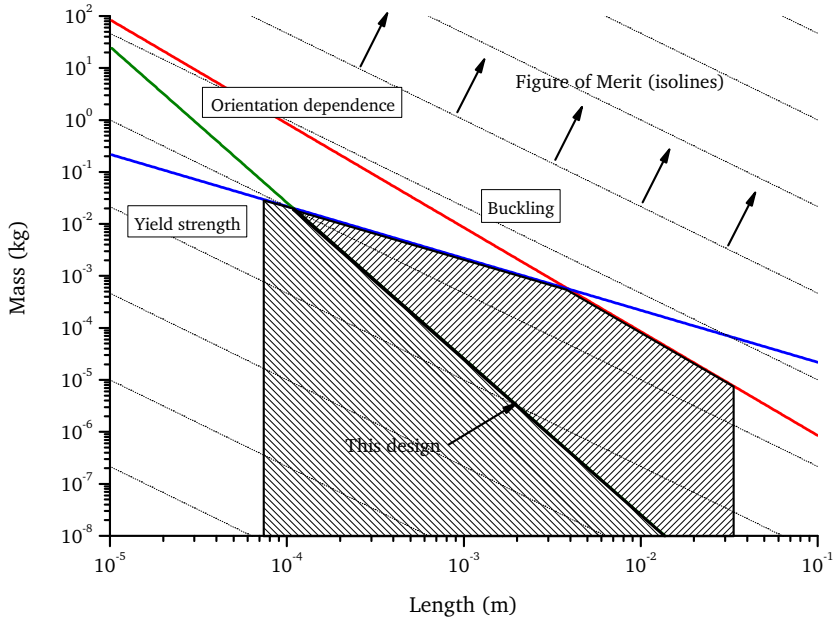

Figure 4.4: *Figure of Merit with the present design included.*

From this Figure of Merit (FoM) can be seen that three restraints are drawn, namely the maximum allowable stress in the system, the restraint of buckling and whether the device can be suspended only vertical or also horizontal (orientation dependence). Since these restraints require it to stay below the lines, the obtainable FoM values are limited. The values of the FoM are indicated with isolines, since the FoM is a function of both the length L and the mass m, which are the main changeable parameters. The arrows indicate

in which the FoM is increasing. Because not every length is available[1], an area can be indicated which contains the feasible devices.

It turns out that the highest value for the Figure of Merit is obtained when both restraints for buckling and the yield strength are intersecting, and in case of only vertical suspension (and use). From chapter 3 the associated equations can be found and expressed in terms of critical mass m. For the maximum allowable stress m_σ equation 4.9 can be defined equal to the yield strength σ_Y.

$$m_\sigma < \frac{nw^2 t\sigma_Y}{6gL} \tag{4.9}$$

To prevent buckling, the mass m_{bck} should be smaller than as given in the next expression.

$$m_{bck} < \frac{4n\pi^2 EI}{gL^2(1-\nu^2)} \tag{4.10}$$

Solving the equality of these expressions yields the optimal length L.

$$m_\sigma = m_{bck} \tag{4.11}$$

gives

$$L = \frac{2\pi^2 Ew}{\sigma_Y(1-\nu^2)} \tag{4.12}$$

From this length, the resulting spring constant K is found. Substitution of L into either the expression for m_σ or m_{bck} gives the optimal mass m.

$$K = \frac{nt\sigma_Y^3(1-\nu^2)^2}{8\pi^6 E^2} \qquad m = \frac{nwt\sigma_Y^2(1-\nu^2)}{12g\pi^2 E} \tag{4.13}$$

The sensitivity S and the associated (mechanical) bandwidth BW of the system for an optimal Figure of Merit is then given by

$$S = \frac{2w\pi^4 E}{3\sigma_Y g(1-\nu^2)} \qquad BW = \omega_r = \sqrt{\frac{3\sigma_Y g(1-\nu^2)}{2w\pi^4 E}} \tag{4.14}$$

Since the Figure of Merit also consists of the TNEA, this value is found by the expression earlier treated, given again in equation 4.15.

$$\sqrt{\overline{a^2}_n} = \sqrt{\frac{4k_B T\omega_r}{Qm}} \tag{4.15}$$

Summarizing and evaluating these properties for the optimal design is done in table 4.10. Although this looks promising, it should be denoted that this a design 'on the edge'. In other words, it is a critical design, meaning that it is not (very) robust, because it could easily break and/or buckle.

[1]Beams with too short length are no beams anymore, and used silicon wafers have a limited diameter (in this case 4"), meaning L has also an upper limit of about 3 cm.

Table 4.10: *Properties of the optimal design.*

Quantity	Symbol	Value	Unit
Length	L	3.90	mm
Aspect ratio (w:L)	R	1:390	
Mass	m	561.5	mg
Sensitivity	S	13.1	nm/mgal
Baseline	b	5.0	cm
Gradient sensitivity	G	0.65	pm/E
Spring constant	K	0.429	N/m
Bandwidth	ω_r	4.40	Hz
Noise floor	$\sqrt{\overline{a^2}_n}$	0.40	μgal/$\sqrt{\text{Hz}}$

When someone would like to use the device also in the vertical direction, making it possible to measure the gravitational field also in the z-direction (earth's gravity), the highest value for the Figure of Merit is found when the restraints for orientation dependence and yield strength are intersecting. The associated mass m_v is found by

$$m_v = \frac{4nE\sqrt{5}w^4t}{9gL^3(1-\nu^2)} \tag{4.16}$$

Equating this expression for m_v equal to the expression for the critical mass m_σ given the yield strength restraint

$$m_\sigma = m_c \tag{4.17}$$

the associated optimal length L becomes

$$L = \frac{2}{3}w\sqrt{\frac{6\sqrt{5}E}{\sigma_Y(1-\nu^2)}} \tag{4.18}$$

From this the associated mass m_v can be evaluated and aspects like sensitivity S and bandwidth BW can be found on a similar way like described in the previous part for the optimal design regarding only suspension in the vertical direction. An overview of these values is given in table 4.11. As can be expected from (combining) the theoretical analysis, the very low noise floor (0.40 ng/$\sqrt{\text{Hz}}$) stays the same for this optimal design, but the sensitivity S is reduced dramatically, which is the result of resisting earth's gravity. Since the mass of this sensor is such large, it is not possible to fabricate two accelerometers out of one wafer. Therefore, no statements are given about the gradient sensitivity G.

4.2.7 Capacitive structures

The behavior of the capacitive structures is of importance when electronic read-out of the system is desired. Therefore, the associated properties of this design are evaluated, starting with the value for the electric permittivity ϵ (see table 4.12).

Table 4.11: *Properties of the optimal design for orientation independence.*

Quantity	Symbol	Value	Unit
Length	L	0.11	mm
Aspect ratio (w:L)	R	1:11	
Mass	m	20.17	g
Sensitivity	S	10.1	pm/mgal
Baseline	b	—	m
Gradient sensitivity	G	—	m/E
Spring constant	K	19.9	kN/m
Bandwidth	ω_r	158.1	Hz
Noise floor	$\sqrt{\overline{a^2}_n}$	0.40	μgal/$\sqrt{\text{Hz}}$

Table 4.12: *Sense fingers.*

Quantity	Symbol	Value	Unit
Electric permittivity (air)	ϵ	$8.85 \cdot 10^{-12}$	F/m

Using the relationships of section 3.5, the properties of the read-out capacitors are evaluated in table 4.13.

Table 4.13: *Properties of the sense fingers.*

Quantity	Symbol	Value	Unit
Number of fingers	n	15	
Width of plates	w	65	μm
Distance between plates	b	5	μm
Thickness of the fingers	h	23	μm
Nominal capacitance	C	39.71	fF

In order to use the sense fingers for electronic read-out, a modulation voltage Um has to be applied to these fingers, as explained in section 3.5. It turns out that at the chosen modulation voltage amplitude V_m the equivalent (or total) spring constant K is reduced from 3.18 (using K_x for 8 beams) to 3.02 N/m, meaning the system is 'stiff' enough for reliable behavior. When feedback is used on these sense fingers at a certain bias voltage U_b, the resulting parameters for this type of feedback for the system are given in table 4.15.

Instead of using feedback on the sense fingers, feedback can also be applied to the fingers on the left and the right of the proof mass, resulting in the changing area method. In table 4.16 the associated parameters are evaluated, proving that the feedback can also be well controlled, although a higher voltage is required to generate the same feedback force as with the changing gap method. However, the system never becomes unstable, since the spring (softening) constant by the feedback is 0 N/m.

Table 4.14: *Modulation voltage properties.*

Quantity	Symbol	Value	Unit
Maximum amplitude	V_m	2.00	kV
Amplitude	V_m	10	V
Frequency	ω_m	1	MHz
Spring (softening) constant	K_m	0.159	N/m
Equivalent spring constant	K	3.02	N/m

Table 4.15: *Feedback using sense fingers.*

Quantity	Symbol	Value	Unit
Bias voltage	U_b	1	V
Sensitivity	S_{fb}	471.3	mgal/V
Spring (softening) constant	K_{fb}	$3.17 \cdot 10^{-3}$	N/m

Table 4.16: *Feedback using 'feedback' fingers.*

Quantity	Symbol	Value	Unit
Number of fingers	n	8	
Width of plates	w	65	μm
Distance between plates	b	5	μm
Thickness of the fingers	h	23	μm
Nominal capacitance	C	21.22	fF
Bias voltage	U_b	1	V
Sensitivity	S_{fb}	19.3	mgal/V
Spring (softening) constant	K_{fb}	0	N/m

4.3 Finite element analysis

In order to determine if the used theoretical analysis corresponds to reality, simulations using the Finite Element Method (FEM) are done. These FEM-simulations are often quite reliable for predicting and investigating the behavior of the real system.

For this purpose the design was implemented in SolidWorks™ 2008, which is a 3D mechanical CAD (Computer-Aided Design) program. Using this user-friendly program it is not difficult to create rather complex structures, which can be exported to a geometry file for usage with FEM software.

With the aid of ANSYS™ 11 (engineering simulation software) the appropriate simulations for the design were carried out. After applying a correct and well-defined mesh, properties like deformation, stress and modal analysis are investigated.

4.3.1 Main parameters

The most important part of simulating the device in ANSYS^{TM} 11 is to determine its sensitivity. Since the sensor should be capable of measuring gravitational accelerations which lie under or around 1 mgal, an acceleration in the x-direction of 1 mgal (10^{-5} m/s^2) is used. The resulting image from the simulation is given in figure 4.5.

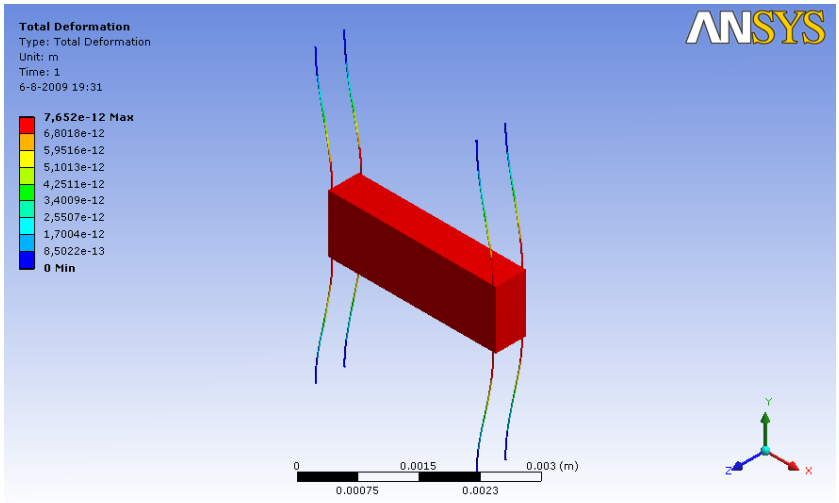

Figure 4.5: *Deformation of the system for a gravitational acceleration of 1 mgal.*

It turns out that the system is a bit more stiff than calculated, because the displacement of the proof mass is 7.7 pm for an acceleration of 1 mgal, giving a sensitivity S of 7.7 pm/mgal. In the theoretical analysis part a displacement of 10.7 pm was calculated. An overview of these values is given in table 4.17. Although this might look as a large deviation between calculation and simulations, the order of the displacement is in agreement. This is of significant importance, because using this performance of such a sensor can be stated, since not all displacements can be measured (too large means 'clipping', too small means too much noise).

Table 4.17: *Comparing the calculated and simulated sensitivity.*

Description	Calculated	Simulated	Difference (%)
Sensitivity	10.7 pm/mgal	7.7 pm/mgal	-28.0 %

4.3.2 Stress

To determine whether the theoretical stress calculations done in the previous section are more or less correct, the design is simulated in ANSYS^{TM} 11. Using the von Mises stress, also called equivalent stress, the robustness of the design can be stated. From the theoretical evaluation the shear stress σ_b has the highest value and is therefore dominating the equivalent (von Mises) stress.

In figure 4.6 the result from the simulation in ANSYS^{TM} 11 is given. Here can be seen that shear stress is indeed dominating by regarding the red colors at the beam edges. From this simulation it turns out that the maximum stress is about 9.13 MPa. Separate ANSYS^{TM} 11 simulations for normal stress in the beams show a maximum value of 19.6 kPa, comparable to the calculated value of 18.1 kPa. From this it is confirmed that the effect of shear stress is indeed much larger than normal stress.

Comparing the maximum stress from ANSYS^{TM} 11 with the calculated shear stress of 21.8 MPa, the simulated value is lower. This can be explained by the knowledge that for the shear stress calculation a straight non-deformable beam was used, which is in reality not the case, which can also be seen in the figure. Important is the fact that the maximum equivalent stress is much lower than the yield strength of silicon σ_Y, which is about 7 GPa, meaning that the device is quite robust for usage. An overview of the stress values is given in table 4.18.

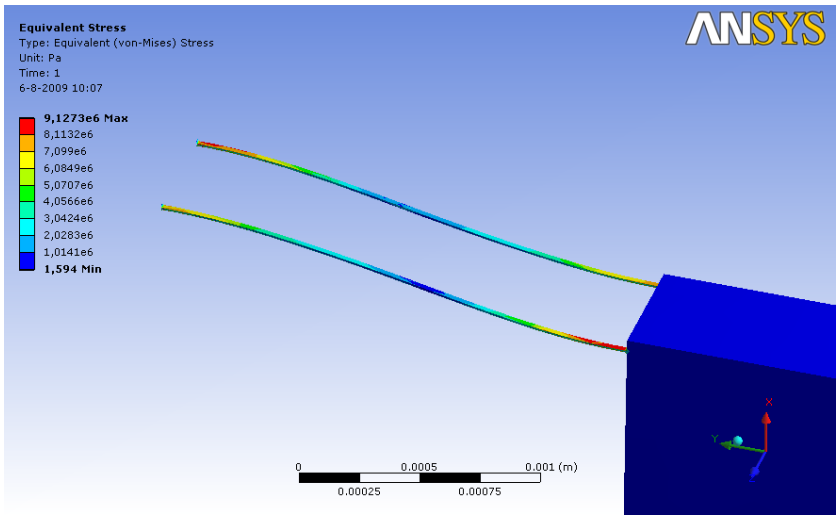

Figure 4.6: *Equivalent (von Mises) stress in the beams of the sensor.*

Table 4.18: *Comparing the calculated and simulated stress.*

Description	Calculated	Simulated	Difference (%)
Normal stress	18.1 kPa	19.6 kPa	+8.3 %
Shear (maximum) stress	21.8 MPa	9.13 MPa	-58.1 %

It is also interesting to see what happens when the sensor is tilted in such a way that earth's gravity itself is acting in the (most sensitive) x-direction, which could be the case during fabrication or transport of the device. In figure 4.7 the resulting deformation is given of the proof mass, whereby the proof mass is moving for about 7.5 μm. Although in this case spring stiffening is not occurring yet, the proof mass will be stopped by the bumps, because these are on a distance of 4 μm

To reduce the stress in the corners of the suspension of the proof mass to the beams, the

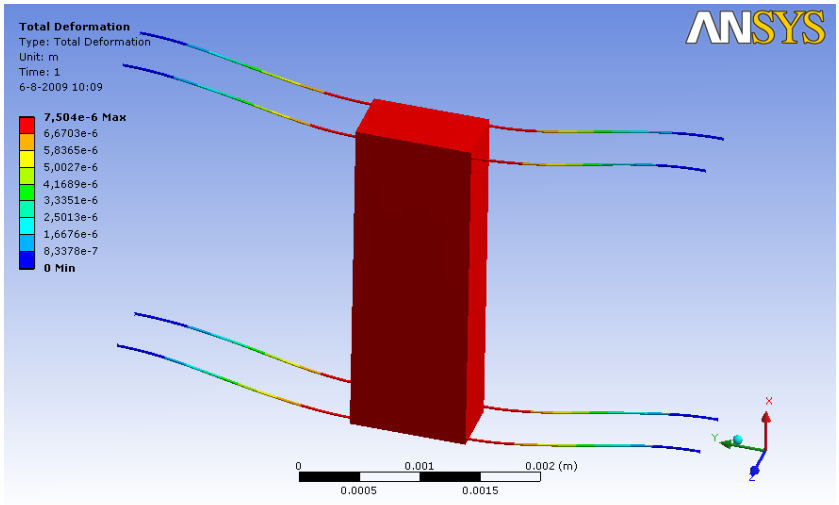

Figure 4.7: *Deformation of the design in the x-direction for earth's gravity.*

corners are rounded (i.e. smoothing the surface). From figure 4.8 can be deduced that this a provable method since the highest stress values are seen in the straight outer parts of the beams.

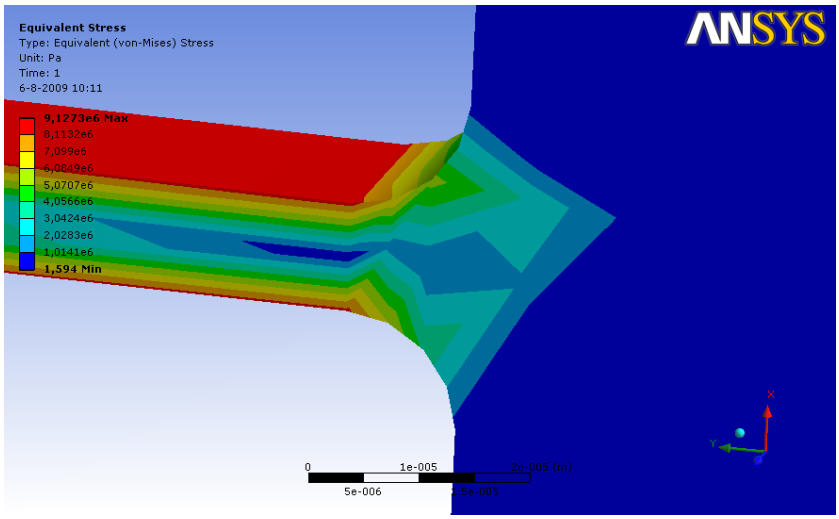

Figure 4.8: *Smoothed corners for reducing stress at the suspension.*

4.3.3 Dynamics

From the theoretical analysis it has been found that three (significant) modes can be expected. In the previous section three resonance frequencies have been calculated, one for each mode. Using ANSYS^{TM} 11 also a modal analysis is carried out.

The first mode is indeed found in the x-direction where the associated resonance fre-

quency is set for 182.1 Hz, which is a bit higher than the calculated 154.6 Hz. The deformation of the system is given in figure 4.9.

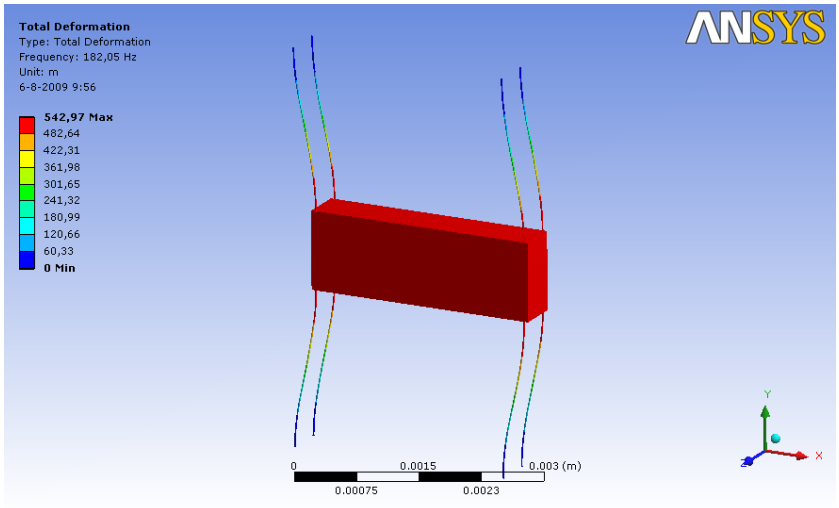

Figure 4.9: *Mode 1 – Translation in x-direction.*

In the y-direction[2] the resonance frequency is found at 376.6 Hz, as given in figure 4.10, which is also higher than the evaluated 355.6 Hz.

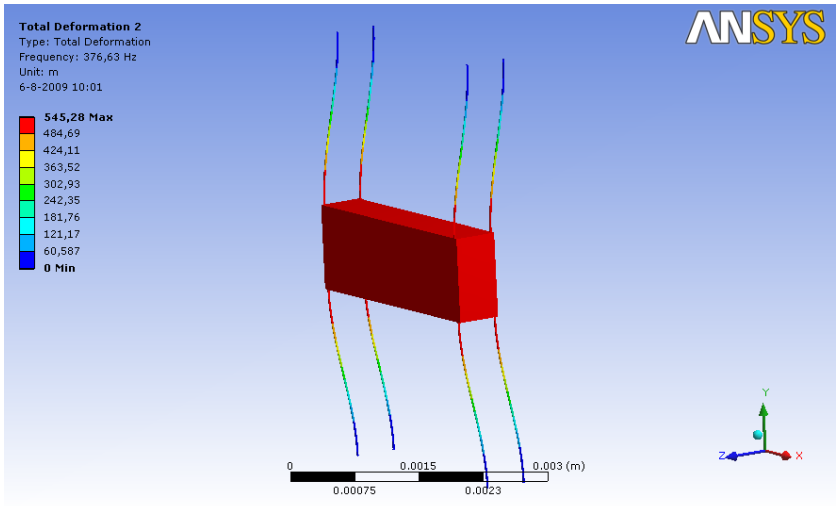

Figure 4.10: *Mode 2 – Translation in y-direction.*

The third resonance frequency of the system is simulated for 631.5 Hz (see figure 4.11), again a bit higher than the 608.1 Hz from the theoretical analysis.

An overview of both the calculated and simulated resonance frequencies of the three modes is given in table 4.19, making clearly visible that each simulated resonance frequency

[2]Notice that ANSYS^{TM} 11 uses a different coordinate system, meaning that x is x, y is z and z is y.

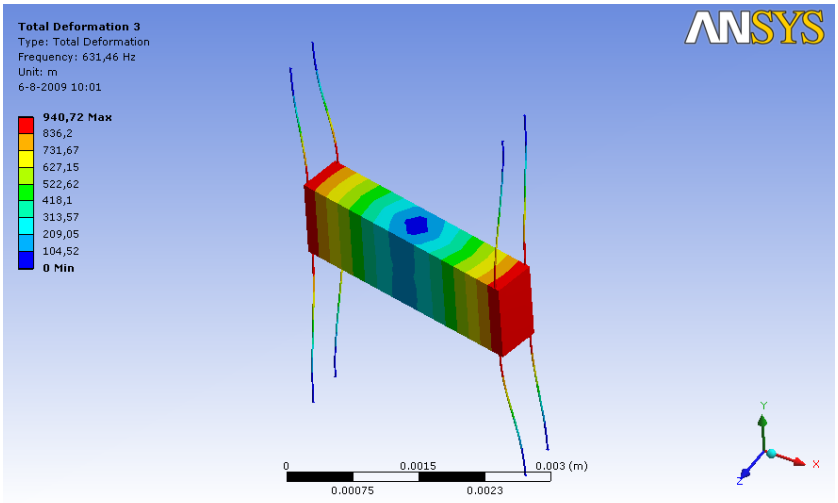

Figure 4.11: *Mode 3 – Rotation in xy-plane.*

is higher than the ones calculated. This is probably due to the fact that in the theoretical analysis the effect of the suspension protection by corner smoothing is neglected. In other words, the beams are effectively in reality a little bit shorter, thus more stiff, thus resulting in a higher resonance frequency.

Although there is a slight deviation between these values for the resonance frequencies of the several modes, the main solutions are in agreement with each other. Namely, the modes are given in the same sequence as calculated, and also the order of and distance between the resonance frequencies are corresponding. So, the theoretical analysis proves to be a good indicator for the expected behavior of the sensor. This is a (big) advantage, because analytical expressions can be used for designing instead of creating a design and investigate how it would behave using FEM simulations.

Table 4.19: *Comparing the calculated and simulated resonance frequencies.*

Mode	Description	Calculated	Simulated	Difference (%)
1	Translation (x)	154.6 Hz	182.1 Hz	+17.8 %
2	Translation (y)	355.6 Hz	376.6 Hz	+5.9 %
3	Rotation (xy)	608.1 Hz	631.5 Hz	+3.8 %

4.4 Conclusions

To investigate what the physical and quantitative properties of a ‘moderate’ accelerometer for geophysical applications are, both the theoretical model and simulation software are used for parameter evaluation. Both methods are in good agreement with each other, wherein the software regards the material a bit more stiff than the theoretical model.

According to the established Figure of Merit and the associated restraints, it follows that the 'optimal' design is found on the intersection of the buckling and yield strength restraint. The evaluated sensitivity of the sensor is about 13.1 nm/mgal, which is according to specifications. When one would have a sensor which is orientation independent, the intersection of the orientation independence and yield strength restraint should be used, giving a sensitivity of 10.1 pm/mgal.

These designs are however quite critical and some margin should be taken using the Figure of Merit for determining the associated design dimensions. In addition, from these numerical results it appears that it will be very difficult to developed a sensor based on this principle to achieve a resolution of 1 nm/mgal.

References

[1] X. Jiang, F. Wang, M. Kraft, and B. E. Boser. "An Integrated Surface Micromachined Capacitive Lateral Accelerometer with $2\mu G/\sqrt{Hz}$ Resolution". In *Solid-State Sensor, Actuator and Microsystems Workshop*, Hilton Head Island, South Carolina, June 2–6 2002.

[2] N. C. Loh, M. A. Schmidt, and S. R. Manalis. "Sub-10 cm^3 Interferometric Accelerometer With Nano-g Resolution". *Journal of Microelectromechanical Systems*, **11**(3):182–187, June 2002.

[3] S. Franssila. *Introduction to Microfabrication*. John Wiley & Sons, Chicester, England, 2004.

Chapter 5

Technology

To fabricate the sensor described in the chapter before, the necessary technology needs to be investigated and a process (flow) has to be produced. In this chapter the required steps and the process flow are described in detail.

5.1 Introduction

In the previous chapters already some requirements with respect to the design were given concerning the proof mass and the beams, which are the main components of the proposed accelerometer. For convenience, in figure 5.1 a schematic overview of the desired sensor is given. Note that only the springs (beams) and the proof mass are given.

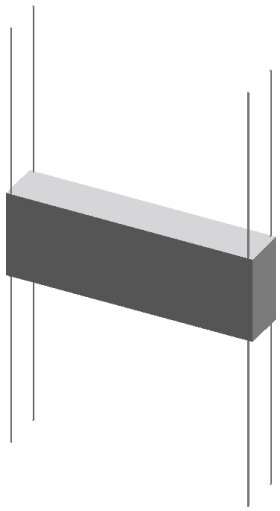

Figure 5.1: *Schematic view of the mass-spring system by SolidWorks™ 2008.*

Eventually, there will be also capacitive structures and bumps[1] present, but design and technology will be focused to create a large proof mass and very long and small beams

[1] Small structures which limit the displacement of the proof mass, in order to prevent capacitive pull-in.

with a low spring constant. From those results the associated process for the capacitive and bump structures can be determined.

5.1.1 Symmetric design

For a reliable sensor with more or less equally distributed stress a symmetrical design is recommended (see figure 5.1). This means that the design is folded over three axes, leading to eight (2^3) parts of the same form factor. Such a design is providing a good response, since the mass and the equivalent spring constant can be easily summed from the parts. It is also quite robust, because the proof mass is supported at every corner. Note that these three requirements (weak springs, large proof mass and symmetric design over all axes) lead to a challenging fabrication process, because it is not difficult to achieve the requirements one by one, but combining them requires proper technology.

5.2 Micromachining

Considering the main requirements for the desired mass-spring system, a suitable type of micromachining should be used for a successful fabrication method, leading to a device with a large proof mass, very long and thin beams, and a symmetric design over three axes. In addition, it is recommended to realize beams out of mono-crystalline silicon, because such beams are perfect springs due to crystal structure of the silicon.

Since the sensor should consist of a large proof mass, it is very convenient to use bulk micromachining as a basic methodology for the process. Although there are other ways of micromachining available, bulk micromachining is convenient for usage, since the proof mass should be very large and the bulk (mono-crystalline) silicon can be used very well for creating and releasing the beams eventually.

Also surface micromachining allows the fabrication of very small and long beams, but using this type of micromachining it is not possible to create the entire sensor out of one piece of mono-crystalline silicon, which is an advantage of bulk micromachining.

Other types of micromachining are bond micromachining and mold micromachining. However, both techniques might lead to difficulties when the beams have to be released from the wafer substrate. In other words, create the sidewall profile (beam thickness) can be done using relative simple technology steps, but releasing the beams requires an etching step to remove material beneath the beams, which makes processing to a challenge.

Therefore, *bulk micromachining* is the chosen type of fabrication methodology and is starting point for development of the required technological steps.

5.2.1 Sidewall coating

To form the rectangular cross-sectioned long and thin beams and a well defined proof mass out of a mono-crystalline silicon wafer using bulk micromachining (see chapter 4 and figure 5.1), a *sidewall coating* can be used in combination with a <111> silicon wafer. The basic idea for using a wafer with this type of crystal orientation is described by Oosterbroek et al. [1]. First, have a look at the differences between a <100>- and a <111>-oriented

crystal, as can be seen in figure 5.2. Note that in this figure the crystal is described by its typical {111}-planes.

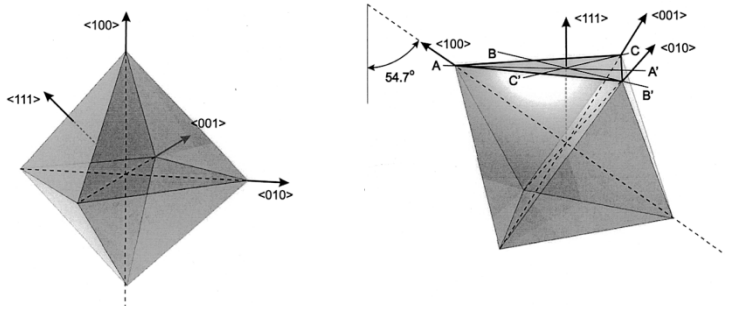

(a) *<100>-oriented.* **(b)** *<111>-oriented.*

Figure 5.2: *Different types of crystal orientation in a silicon wafer.*

The etch rate of silicon depends on its crystal orientation [2]. Especially etching in the {111}-directions is much slower than etching compared to the {100} directions. When a proper design and wafer crystal orientation is chosen, this property of wet etching can be used in a smart way.

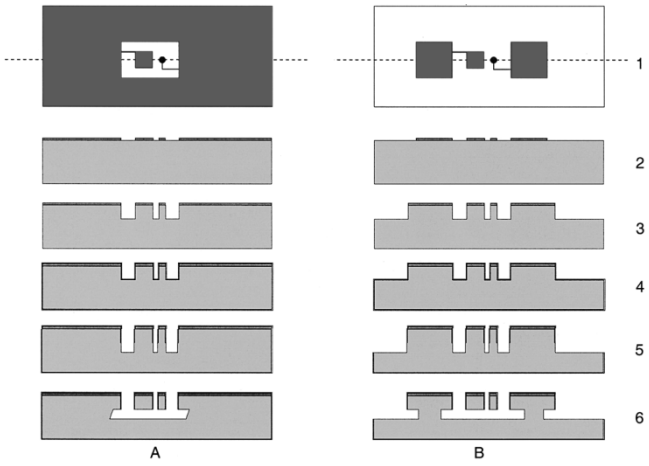

Figure 5.3: *Methodology of sidewall coating for creating beams [1].*

In order to do so, apply sidewall coating to the device. This principle is visualized in figure 5.3, for both inside and outside etched structures. In step **(2)** a pattern is applied using photolithography. Next, directional etching is applied to create the trenches for determining the thickness of the structures to release **(3)**.

To protect the beams during etching a sidewall coating is applied (for example by silicon dioxide) **(5)**. After this, the structure is directional etched, resulting in the bottom removal of the silicon oxide and a part of the silicon beneath **(5)**.

The final step **(6)** is performing anisotropic wet etching of silicon, resulting in the re-

lease of the beams. From theory about wet etching {111}-planes etch (much) more slowly than other planes (like {100}-planes), meaning that etching mainly occurs in the x and y direction, when z is defined along the thickness of the wafer.

Although etching occurs nearly only in the above described directions, consider the {111}-planes in the x and y direction. Depending on the direction of etching, the wall will also show an angle after etching (regard figure 5.3), as given in figure 5.4 [1].

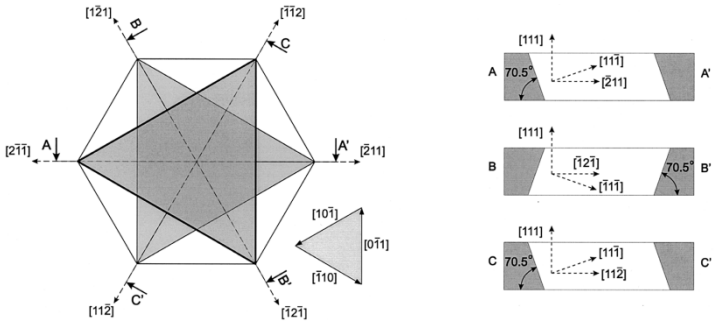

(a) *Top view.* **(b)** *Cross-section.*

Figure 5.4: *Two-dimensional view of {111}-planes in a <111>-oriented silicon wafer.*

5.3 Total design

The total design consists of combining the previous aspects about symmetrical design and side-wall coating. To perform electrical readout by capacitive sensing, the wafer will be partially packaged by bonding a glass wafer on top, which is regularly the case for bulk micromachined MEMS accelerometers [3]. Since the wafer is just one side polished and because polished surfaces are highly recommended for good quality bonds [4, 5], the sensor cannot be fully packaged using wafer bonding. Although, not when a one side polished wafer is used.

In the next section (5.4) an overview is given for the entire device, including the glass wafer for packaging. Every step will be explained, and also some design considerations are given for several steps. At the end of this chapter it becomes clear why the chosen fabrication methodology is useful for creating such a sensor with electronic read-out functionality.

5.4 Process overview

Since the eventual sensor consists of a glass wafer bonded on a silicon wafer, the associated process flows are treated separately. First, the silicon wafer process is explained. Then, the silicon wafer is bond-ready and the glass part of the process will be discussed. On the end the two wafers are bonded.

5.4.1 Silicon wafer

The base of the design is an <111>-oriented silicon wafer. The ultimate design will consist of a double side polished (DSP) wafer, but since these wafers are not standard available within the cleanroom of MESA$^+$, a one side polished (OSP) wafer is used.

After cleaning the wafer (figure 5.5a), a thin layer of 100 nm of Silicon Rich Nitride (SiRN) is deposited using Low Pressure Chemical Vapor Deposition (LPCVD), as visualized in figure 5.5b. On top of this layer a film of 1500 nm of Silicon Oxide (SiO_2) is deposited with LPCVD tetraethyl orthosilicate (TEOS), regarding figure 5.5c.

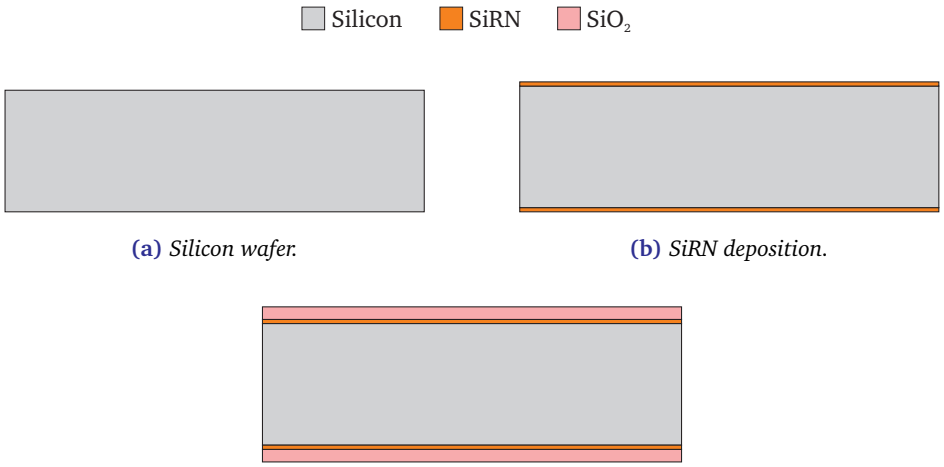

(a) *Silicon wafer.*

(b) *SiRN deposition.*

(c) *SiO_2 deposition.*

Figure 5.5: *Coating of the <111> silicon wafer before photolithography.*

With the presence of these layers, the lithography of the process can be started. First the top side of the wafer is treated using SU-8 lithography (figure 5.6a). SU-8 is a commonly used epoxy-based negative photoresist, which is known about its straight sidewall profile after postbaking [6]. This straight profile is useful for a better protection of the corners during directional etching, since photoresist is always slightly attacked during Deep Reactive Ion Etching (DRIE) processes. The postbake of the photoresist is performed to reduce the damage of the photoresist during directional etching.

The SU-8 lithography process is started with a dehydration bake. Then the wafers are spin-coated with a layer of SU-8, at such a spinning speed that a thickness of 4 μm is obtained. The next step is doing a softbake, before exposing the SU-8 using the created mask with the sensors. After exposure a post-exposure bake is done for hardening the SU-8. When this is completed, the SU-8 can be developed, leaving the exposed SU-8 behind and ready for postbaking.

Now that the pattern (width) of the sensors is created using SU-8 lithography, the thickness of the beams can be adjusted using DRIE. First, the Silicon Oxide (SiO_2) and Silicon Rich Nitride (SiRN) are removed[2] according to figure 5.6b, and next the desired thickness

[2]Information about the used DRIE recipes can be found in appendix A.

of the beams is controlled by removing the same thickness of silicon (Si), visible in figure 5.6c. Afterward, the remaining SU-8 is removed using a "Piranha" cleaning procedure (figure 5.6d).

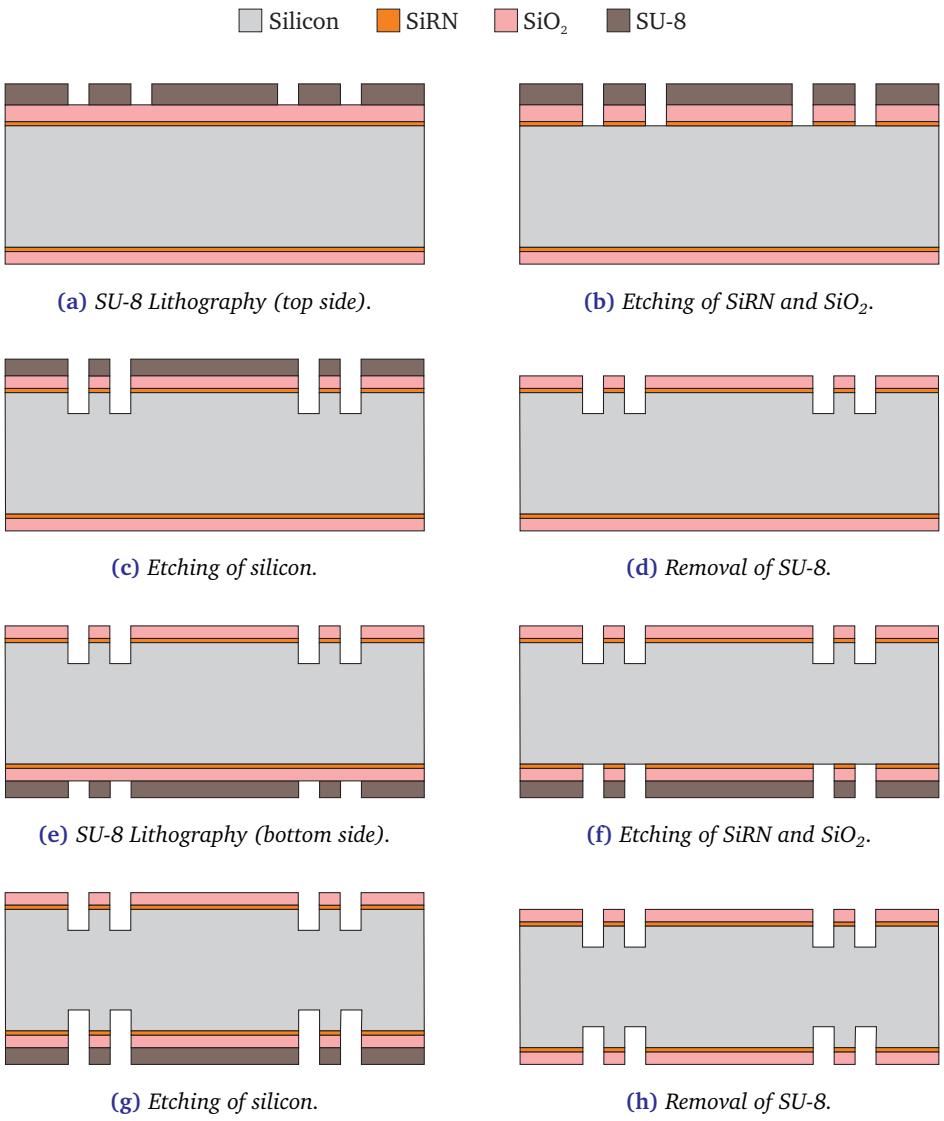

(a) *SU-8 Lithography (top side).*

(b) *Etching of SiRN and SiO_2.*

(c) *Etching of silicon.*

(d) *Removal of SU-8.*

(e) *SU-8 Lithography (bottom side).*

(f) *Etching of SiRN and SiO_2.*

(g) *Etching of silicon.*

(h) *Removal of SU-8.*

Figure 5.6: *SU-8 lithography and directional etching for both sides.*

Since a symmetrical design is desired, it is quite straightforward to apply the same process to the bottom side of the wafer. In figures 5.6e–5.6h a similar treatment is given as for the top side (i.e. the used steps are the same). Special attention should be given to the mask alignment procedure using the EVG 620 Mask Aligner, because the effect of misalignment between the top and bottom side of the silicon wafer should be minimized for an optimal three-axes symmetric device.

When both sides of the wafer are processed with SU-8 lithography a small part of the SiRN will be (back)etched using hot phosphoric acid (H_3PO_4), as illustrated in figure 5.7a.

Note that the SU-8 layer is removed ("Piranha" cleaning) before this step, because it will not survive 180 °C. An important reason for backetching the SiRN layer is to achieve a conformal coating around the corners. Another reason is using the effect of the bird's beak, which is explained later on.

After etching the SiRN the silicon will be wet thermal oxidized to form a small layer of SiO_2 (figure 5.7b). The interesting part about thermal oxidation is that a part of the silicon (44%) is consumed, providing a very good adhesion between these materials. Also, the junction of silicon and SiO_2 moves into the silicon, giving a better protection of the silicon during directional etching.

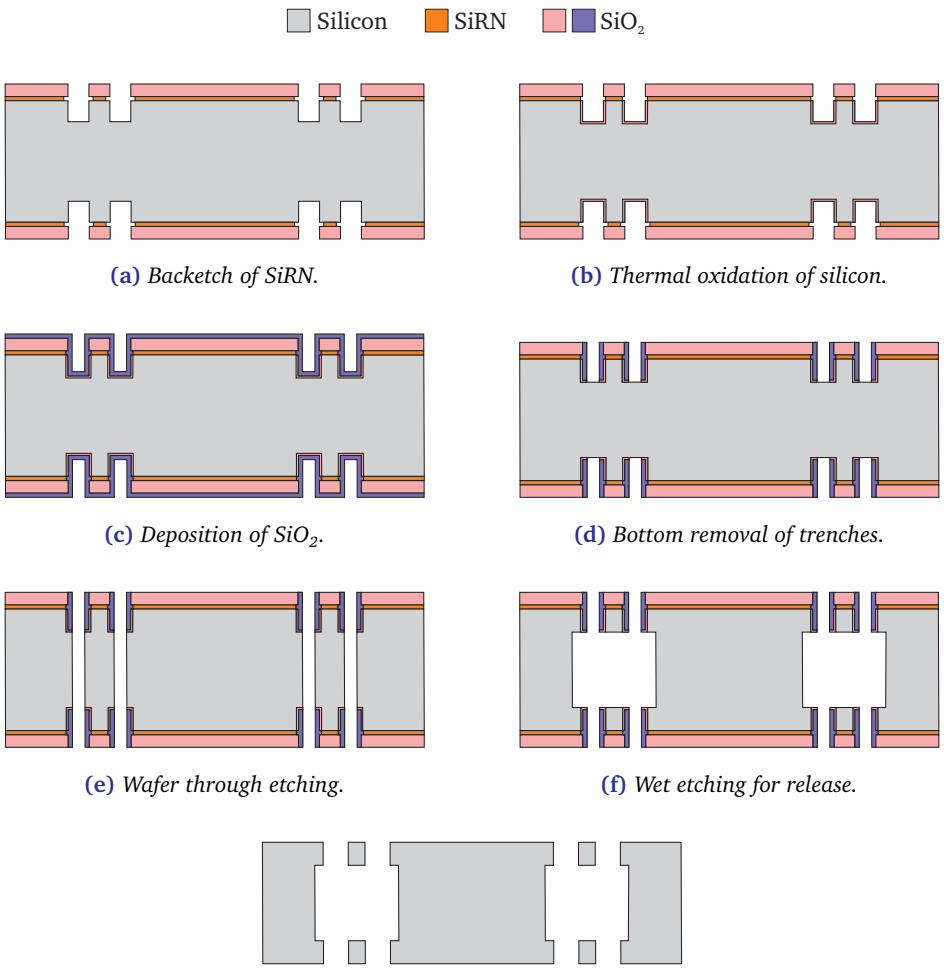

(a) *Backetch of SiRN.*

(b) *Thermal oxidation of silicon.*

(c) *Deposition of SiO_2.*

(d) *Bottom removal of trenches.*

(e) *Wafer through etching.*

(f) *Wet etching for release.*

(g) *Stripping SiRN and SiO_2.*

Figure 5.7: *Further processing of the device.*

Although the thickness of the grown silicon dioxide is quite small (50 nm), it provides a bird's beak for optimal sealing, a very good adhesion for the silicon dioxide which is deposited using TEOS. The SiO_2 layer by TEOS forms the major part of the sidewall coating in this process (figure 5.7c). This layer requires a thickness of at least half the layer thickness

of SiRN (50 nm), since the gap created by H_3PO_4 etching should be filled for a conformal coating. However, using a thicker SiO_2 layer by TEOS (250 nm) gives a thicker sidewall, resulting in a better protection of the silicon during TMAH (wet) etching, since the SiO_2 sidewall is also attacked during TMAH etching (TMAH selectivity is not infinite) [7].

Note that thermal oxidation can not provide optimal coating, because it will be only present in the trench. When removing this oxide layer, a lot of the (first) SiO_2 mask layer will be removed. Using TEOS for SiO_2 also the total mask layer (on top) becomes thicker, decreasing the damage to the first SiO_2 mask layer. Therefore, a thin SiO_2 layer by thermal oxidation and a rather thick layer of SiO_2 by LPCVD TEOS should be used.

Next, the bottom of the trenches needs to be removed in order to etch the silicon beneath it, visualized in figure 5.7d. Etching this oxide layer is done by using DRIE at the Adixen AMS100SE. The associated recipe for perfect removal of SiO_2 in (high aspect ratio) trenches has been recently developed by Brookhuis [8]. Since the SU-8 mask layer is not present anymore, the SiO_2 on top of the wafer is also attacked. But, since this layer is quite thicker than the bottom part, most of it will remain as protection for further etching.

After removing the bottom, the recipe is changed and the silicon beneath will be wafer-through etched using DRIE (again), given in figure 5.7e. Important is that for wafer-through etching a special carrier wafer with a 'drainage' system and Fomblin oil for thermal contact is required. This carrier wafer needs to be mounted below the device wafer. The reason for this is to keep the helium backside cooling system operational during wafer-through etching for maintaining the (device) wafer temperature low. When there are wafer-through holes present inside the wafer, the helium starts leaking into the chamber and cooling is not working properly anymore.

The absence of a drainage system in the carrier wafer could destroy some parts of the wafer, because the wafer is loaded under atmospheric conditions, but DRIE processes are usually carried out in vacuum. When some cavities at the bottom are sealed from vacuum pressure (thus at atmospheric pressure), and the silicon above is almost etched away, there is a pressure difference present over a small silicon membrane. When this pressure difference becomes too large, the membrane breaks, leading to damage of the wafer. Appendix A.2 contains the process flow and associated process details for the carrier wafer.

To release the beams and structures using the before described technology by using the {111}-planes in a proper way, a tetramethylammonium hydroxide (TMAH) solution of 25% at 70°C is used for wet etching of silicon. Compared to potassium hydroxide (KOH), TMAH shows better selectivity with respect to the SiO_2 sidewall coating, which is desired in this case (it is about releasing the structures, etching time is not very important). Also smooth surfaces can be obtained using TMAH as an etch solution [2].

When the structures are eventually released, the sensor will work mechanically (figure 5.7a), but is not yet ready for applying electrical readout by capacitive sensing. Therefore, strip the SiO_2 and the SiRN of the device using hydrogen fluoride (HF), as illustrated in figure 5.7g.

Details of the described and used process steps can be found in appendix A.1, where the part of the process document for the silicon device wafer is given.

Bird's beak

Although one might expect that sealing the beams by using only SiO_2 layers both on top and at the sidewalls shows optimal protection, it could be possible for the TMAH etchant to move through the interface between the separate SiO_2 layers toward the silicon, starting undesired etching [9]. Therefore, an effect known as bird's beak can be used to prevent this and to perfectly seal the protected structures from TMAH etching [10]. The bird's beak for the described process flow is given in figure 5.8.

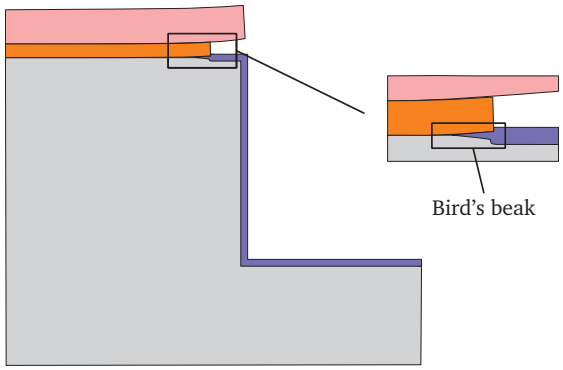

Figure 5.8: *Bird's beak.*

The presence of a bird's beak is the result of a combination of (wet) thermal oxidation of silicon, also called Local Oxidation of Silicon (LOCOS), and a SiRN layer in its neighborhood. It appears that under thermal oxidation conditions a small part of silicon beneath the SiRN is capable of oxidizing, but this effect is limited to a certain distance and height. These limitations result eventually in a shape called bird's beak.

Typical properties of a bird's beak are lifting of the SiRN layer (oxidation of the silicon) and very good closing between the SiRN layer and the SiO_2 layer next to it. Therefore, it will offer perfect sealing of the protected structure at the transition from SiO_2 to SiRN.

Conformal coating

For an optimal protection of the structures a conformal coating is recommended, which can be achieved in this process by using TEOS for SiO_2 deposition. A conformal coating means that the deposited film has the same thickness regardless the place of deposition. In other words, the thickness of the sidewall coating is the same everywhere, offering also a good protection in the lower parts of the trenches. Since a small backetch was applied for the SiRN layer, the expected profile of the SiO_2 by TEOS is illustrated in figure 5.9.

RIE lag

The effect of RIE lag should be taken into account during wafer-through etching, which causes slower etching in high aspect ratio trenches [11]. Therefore, the capacitive finger structures are (mask) designed in such a way that a set of fingers, wherein a finger has a thickness of 5 μm, is always surrounded by a larger gap (25 μm), reducing the aspect ratio

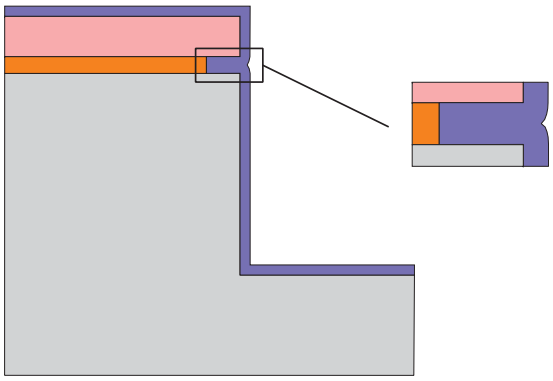

Figure 5.9: *Conformal SiO_2 coating using TEOS.*

of the trench to about 1:20, in order to minimize the effect of RIE lag. Using TMAH etching, the sets of fingers are released, which is visualized in figure 5.10.

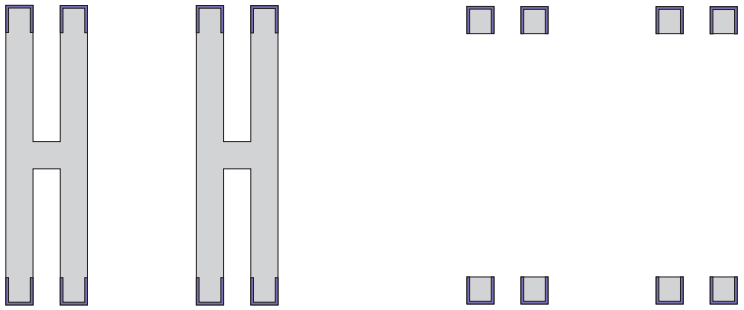

(a) *Before TMAH etching.* **(b)** *After TMAH etching.*

Figure 5.10: *Set of capacitive fingers before and after TMAH etching.*

5.4.2 Glass wafer

Although the mechanical part of the sensor can be realized using the process treated before, the system is still made out of one part of silicon, meaning every part is connected to each other. To implement the electronic read-out capability, the device (i.e. the proof mass and capacitive fingers) should be isolated electronically, so read-out and optional feedback can be applied.

In order to do so, a glass (Borofloat) wafer will be prepared and eventually bonded on top of the sensor. Doing so, the system will be mechanical connected by means of the (bonded) glass wafer, but can be electronically isolated, because glass is a good insulator, consisting for 81% of SiO_2 [12].

For electrical connections with the silicon for read-out and feedback, some holes through the glass wafer should be created, making wire bonding to the silicon possible. In addition, the glass should also consist of a large cavity for the mass to move in, because it can move in

multiple directions (see chapter 3). The required process flow for realizing this glass wafer is given in figure 5.11.

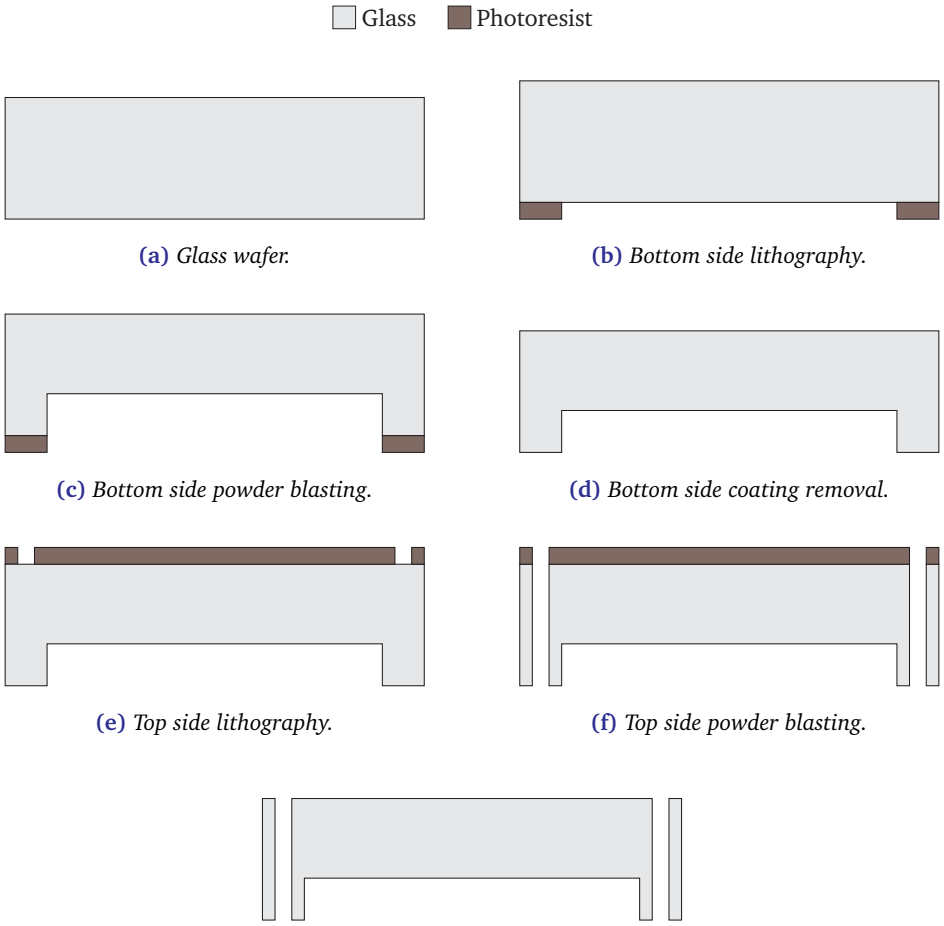

(a) *Glass wafer.*

(b) *Bottom side lithography.*

(c) *Bottom side powder blasting.*

(d) *Bottom side coating removal.*

(e) *Top side lithography.*

(f) *Top side powder blasting.*

(g) *Top side coating removal.*

Figure 5.11: *Preparing the glass wafer for bonding.*

The process for the glass wafer starts with a clean Borofloat wafer (figure 5.11a), with approximately the same dimensions as a silicon wafer. Then the bottom side is coated with foil, in order to make powder blasting possible (figure 5.11b). Powder blasting of glass is for this purpose quite useful, because it is a well known technique in MEMS technology, it is pretty fast and creates a rough surface [13]. This rough surface prevents the proof mass from sticking to the glass which could be the case when the surface is very smooth and the proof mass is placed under high accelerations. The result after powder blasting is given in figure 5.11c.

After powder blasting the bottom side using lithography techniques for applying the foil, the foil should be eventually removed (figure 5.11d). The next step is doing a similar process for the top side of the glass wafer, but now for creating the wafer-through holes for establishing the eventual wire bonds. Again, lithography techniques are used for applying,

exposing and developing the foil, to make sure the holes are created on the desired positions. Removing the foil afterward results in a (pure) glass wafer consisting of the desired patterns (figures 5.11e–5.11g). See appendix A.3 for the process details.

5.4.3 Bonding the wafers

Now both wafers are fabricated using the described technology and fabrication steps, these wafers should be eventually bonded together. This is done using anodic bonding, which gives a very solid bond between the silicon and glass wafer. Anodic bonding consists of applying a high voltage (at least 500 V), thus electrical field, over the interface between the silicon and glass wafer at a high environmental temperature (about 400°C), as is illustrated in figure 5.12 by Veenstra et al. [14]. With this type of bonding the silicon at the interface changes to SiO_2, explaining the strong chemical bond with the other SiO_2.

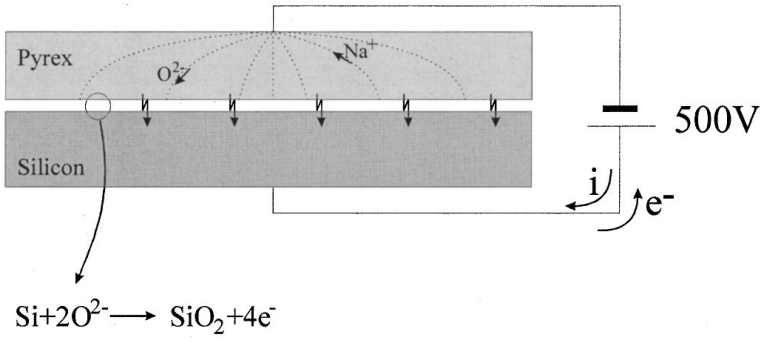

Figure 5.12: *Illustration of anodic bonding (pyrex is a glass equivalent).*

The result from bonding the two wafers can be seen in figure 5.13, wherein the electrical isolation of the several parts of the silicon wafer can be viewed by its cross-section and the mechanical connection using the glass. For details about the wafer bonding, see the process given in appendix A.4.

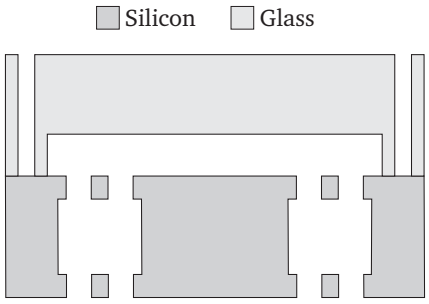

Figure 5.13: *Preparing the glass wafer for bonding.*

Note that the cavity in the glass wafer for letting the proof mass move for every direction needs to have a certain depth due to the strong electric forces caused by the anodic bonding.

Since the proof mass is sensitive for small forces, the proof mass will certainly show a large displacement for the bonding forces. From the results of the spring stiffening analysis from section 3.3, the cavity should have a depth of a least a few times of the thickness of the beam. Since a beam will have a thickness between 20–25 μm, the cavity should be at least 100 μm deep to prevent permanent stiction of the proof mass to the glass wafer. With powder blasting these depths are very good feasible, with the advantage that the surface becomes also quite rough.

5.5 Masks

Although the process is rather clear and straightforward and the simulations and calculations are in good agreement with each other, it is a good idea to do several tests before fabricating the eventual bonded devices with electrical read-out. Therefore, test devices are realized using the procedure described in the next subsection. Next, a mask design is made for the eventual devices, based upon the parameters given in chapter 4.

5.5.1 Test devices

To determine whether the chosen process has the expected outcome and results, a mask design for the silicon wafer is made consisting of several types of devices. Regarding the designed accelerometer of figure 4.1, the devices vary between very small beams (very robust) and very long beams (very sensitive).

The mask is designed in such a way that every device is created within a chip of 1x2 cm. The advantage of this method is that every device can be characterized separately, but a disadvantage is the absence of a possible electrical connection, since the device cannot be isolated electrically in case of bonding an appropriate glass wafer on top. This means the devices can be characterized only mechanically, which is however the base of the sensor functionality.

5.5.2 Devices for bonding

To realize the eventual devices with a glass wafer bonded for electronic read-out using the capacitive structures, the design of the mask for the silicon wafer should be changed a bit with respect to the one for the test devices. To do so, the base of the design is an array of (four) accelerometers, spanning the entire width of a silicon wafer, as is given in figure 5.14.

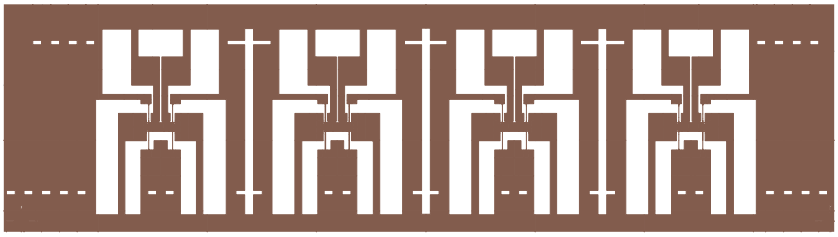

Figure 5.14: *Dicing an array of identical sensors.*

In order to achieve the electrical isolation of the vital parts of the accelerometer, and to also keep the device strong and robust, the device should be diced along the dashed white lines. The white areas mean there is no silicon present (etched). Combined with a partial dice into the glass wafer along the white dashes silicon line, it should be possible to break the wafers (after bonding) along that line. Doing so, a single device can be obtained as given in figure 5.15.

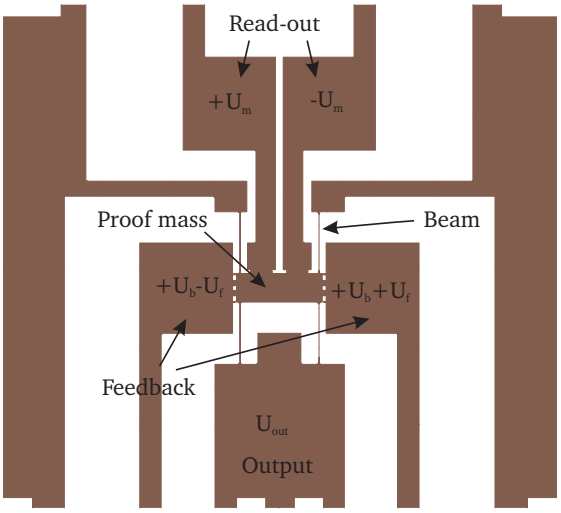

Figure 5.15: *Main lay-out of the accelerometer for connections.*

In this figure the important parts of the device are indicated. Regarding the brown (silicon) parts for the vital functions, it can be seen that every part is now electrically isolated. When the glass wafer is bonded with the right pattern, as given in section 5.4.2, the necessary cavity for the proof mass and the electrical connections can be established. The resulting device is visualized in figure 5.16

5.6 Conclusions

As a starting point for the process of the proposed accelerometer for geophysical applications bulk micromachining is used. Together with sidewall coating technology and anisotropic wet etching in <111>-oriented wafers, it is possible to realize an accelerometer with a large proof mass, thin and long beams, and design symmetry over three axes.

The process consists of coating a <111>-wafer with SiRN and SiO_2. Next, the design is created using SU-8 lithography combined with directional etching on both sides of the wafers, to realize three-axes symmetry. After patterning a SiRN backetch is applied, the SiO_2 sidewall coating is realized and direction etching is done for wafer-through etching. After wafer-through, the desired structures are released using TMAH anisotropic wet etching.

For sensor packaging a glass wafer with a cavity and wafer-through holes for wire bonding is proposed. Bonding this glass wafer on top of the silicon wafer, it is possible to create electrical isolation for capacative read-out of the sensor.

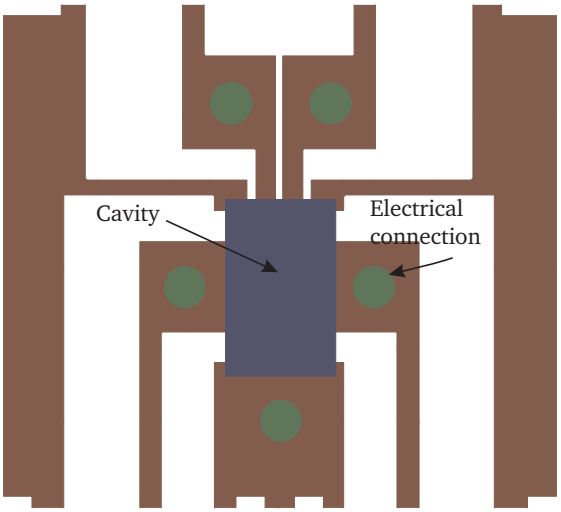

Figure 5.16: *Resulting connection points and cavity from the glass wafer.*

References

[1] R. E. Oosterbroek, J. W. Berenschot, H. V. Jansen, A. J. Nijdam, G. Pandraud, A. van den Berg, and M. Elwenspoek. "Etching Methodologies in <111> oriented wafers". *Journal of Microelectromechanical Systems*, **9**(3):390–398, September 2000.

[2] H. Jansen, N. Tas, and J. Berenschot. "MEMS-Based Nanotechnology". *Encyclopedia of Nanoscience and Nanotechnology*, **X**:1–107, 2004.

[3] M. Elwenspoek and R. Wiegerink. *Mechanical Microsensors*. Springer, 2001.

[4] C. Gui, M. Elwenspoek, N. Tas, and J. G. E. Gardeniers. "The effect of surface roughness on direct wafer bonding". *Journal of Applied Physics*, **85**(10):7448–7454, May 1999.

[5] G. Li and L. Wang. "Influence of bonding parameters on electrostatic force in anodic wafer bonding". *Thin Solid Films*, **462**:334–338, 2004.

[6] J. Liu, B. Cai, J. Zhu, G. Ding, X. Zhao, C. Yang, and D. Chen. "Process research of high aspect ratio microstructure using SU-8 resist". *Microsystem Technologies*, **10**:265–268, 2004.

[7] O. Tabata, R. Asahi, H. Funabashi, K. Shimaoka, and S. Sugiyama. "Anisotropic etching of silicon in TMAH solutions". *Sensors and Actuators A: Physical*, **34**(1):51–57, July 1992.

[8] R. Brookhuis. "A MEMS based micromirror for optical projection displays". Master's thesis, University of Twente, 2009.

[9] M. J. de Boer, R. W. Tjerkstra, J. W. Berenschot, H. V. Jansen, G. J. Burger, J. G. E. Gardeniers, M. Elwenspoek, and A. van den Berg. "Micromachining of Buried Micro

Channels in Silicon". *Journal of Microelectromechanical Systems*, **9**(9):94–103, March 2000.

[10] P. Smeys. *Local Oxidation of Silicon for Isolation*. PhD thesis, Stanford University, 1996.

[11] H. Jansen, M. de Boer, R. Wiegerink, N. Tas, E. Smulders, C. Neagu, and M. Elwenspoek. "RIE lag in high aspect ratio trench etching of silicon". *Microelectronic Engineering*, **35**:45–50, 1997.

[12] Schott. "Schott Borofloat 33 – The versatile floated borosilicate glass", 2009.

[13] A. Pawlowski, A.Sayah, and M. Gijs. "Microfabrication of Powder Blasting". *Institute of Microelectronics and Microsystems*, 2002.

[14] T. T. Veenstra, J. W. Berenschot, J. G. E. Gardeniers, R. G. P. Sanders, M. C. Elwenspoek, and A. van den Berg. "Use of Selective Anodic Bonding to Create Micropump Chambers with Virtually No Dead Volume". *Journal of The Electrochemical Society*, **148**(2):68–72, 2001.

Chapter 6

Fabrication

To achieve a working sensor, the fabrication process is important. In this chapter the fabrication process is analyzed using information obtained by inspection with both optical microscopy and scanning electron microscopy (SEM). From these results can be determined whether the chosen fabrication process is useful for producing a MEMS accelerometer for geophysical applications and to investigate what the critical parts of the process are.

6.1 Introduction

In order to determine whether the chosen fabrication process is giving the outcome as predicted, some test devices were fabricated using the process flow described in chapter 5. The differences between the used process flow and the one discussed in the previous chapter are the thickness of the SU-8 (5 μm instead of 4 μm) and the fact that only one side of the wafer is used. In other words, lithography has only been done for the top side combined with a deep etch into the wafer instead of a wafer-through etch using DRIE. The results of the test after wet etching in TMAH are given in figure 6.1. Note that in this figure the (sidewall) coating is still present.

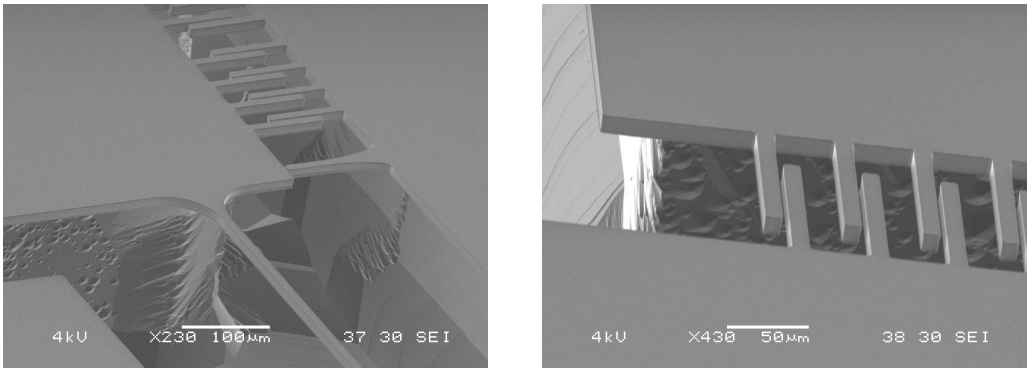

(a) *Beam.* **(b)** *Sense fingers.*

Figure 6.1: *Results of TMAH etch of test structures.*

From these SEM-images can be seen that the technology in principle works. The release of the finger structures and the beams can be seen quite well, together with the underetch of the proof mass and the substrate by TMAH. One can also see that the angle of the etched silicon with respect to the top side is not 90 degree, but a little less, which is explained by the silicon crystal orientation in a <111>-wafer (see also figure 5.2). Now, the fabrication of the devices itself needs to be investigated.

6.2 Device fabrication

Using the experience gained during the fabrication of the test structures, the devices could be fabricated. Now, the complete process flow from chapter 5 is used, meaning that both sides of the <111>-wafer are used. First, some results are given concerning the wafer-through etch to investigate the profile of the silicon in the wafer after DRIE and to get an idea about the alignment of the top side with respect to the bottom side of the wafer.

After this DRIE step, the wafer is etched in TMAH for the release of the proof mass, the fingers and the beams. Given the results of the previous fabrication tests, no serious problems were expected. However, it turns out that technology for the used process is at some points critical, which is discussed in detail.

6.2.1 Wafer-through etching

Using the Adixen AMS100SE for DRIE the wafer-through etching of the device wafers was performed. This wafer-through etching was performed in such a way that the top side of the wafer was etched relative long (etching about 300–400 μm), and the bottom side was etched with the time required for wafer-through. In figure 6.2 the results after wafer-through etching are given. In this figure can be seen that the profile of the etched silicon is not completely straight, but shows a little tapering. This effect can be seen very well beneath the beams, because they are 'released' already. Remark that this tapering effect is not (very) important for the resulting devices, because the (tapered) silicon beneath the beams will be etched by TMAH.

Regarding the position of the beams on top and at the bottom of the wafer, the alignment of the wafer during the second lithography part was done in a correct way. However, it is hard to determine the exact misalignment, because the wafer has a thickness of about 500 μm, and typical alignment errors (misalignment) during lithography are in the order of 1–3 μm. This means that typical misalignment compared to mutual distances between the springs is very small. So, probably the influence of misalignment on the performance of the sensor is (very) small, either because the dimensions of the springs and the proof mass are not changed. To check whether such misalignment is indeed of low influence on the sensor behavior, several sensors from different batches should be characterized and its mutual differences in behavior should be investigated.

Another result from wafer-through etching is the release failure of the finger structures for capacitive sensing. Although the beams and bumps[1] are free (see figure 6.2), the fingers are not, when looking at the images given in figure 6.3.

[1] See sections 3.5 and 4.1 for more information.

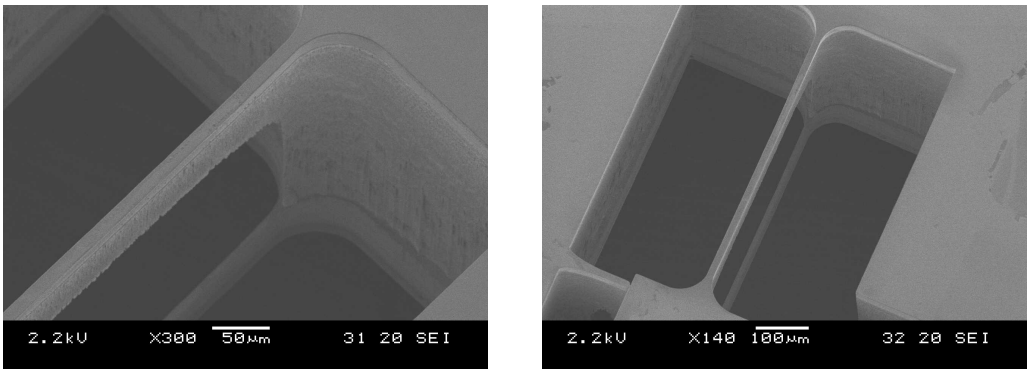

(a) *Tapering by DRIE.* **(b)** *Top and bottom beams visible.*

Figure 6.2: *After wafer-through etching using DRIE.*

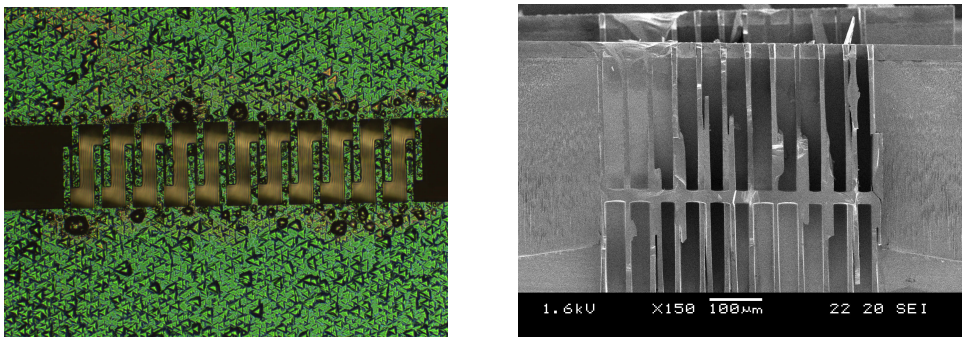

(a) *Fingers not released (top view).* **(b)** *Not wafer-through everywhere (cross-section).*

Figure 6.3: *Wafer-through etching using DRIE at finger structures.*

Looking at the non-polished side of the <111>-wafer, the large gaps near the finger structures are released (see figure 6.3a), but between the fingers there is still silicon present. Using the Scanning Electron Microscope (SEM) a cross-section of the finger structures is given in figure 6.3b, from which can be seen that the fingers are about to be released. From this, the etch rate of silicon in the trenches around the fingers is lower than in the trenches around the beams and bumps. This difference in etch rate by DRIE for wafer-through etching can be explained by the aspect ratio of the trench (gap), also known as RIE lag [1]. So, although a set of fingers (gap 5 μm) was already separated by larger gaps (25 μm), these gaps are probably still not wide enough (see figure 6.3a).

6.2.2 TMAH etching

After wafer-through etching, the next step in the process is wet etching of silicon using TMAH as etchant. The result of this wet etch should be the release of the beams, bumps and finger structures. In figure 6.4 several images by SEM are given after TMAH etching.

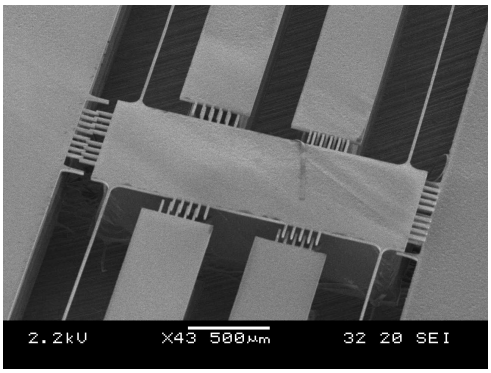

(a) *Sensor overview.*

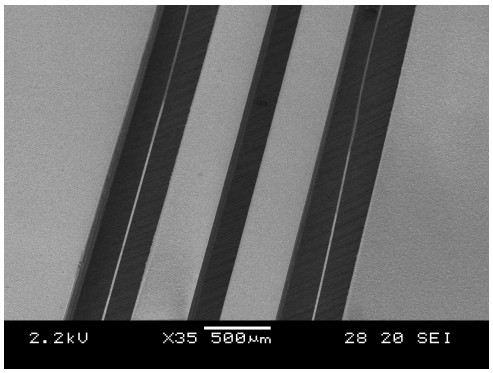

(b) *Beam buckling.*

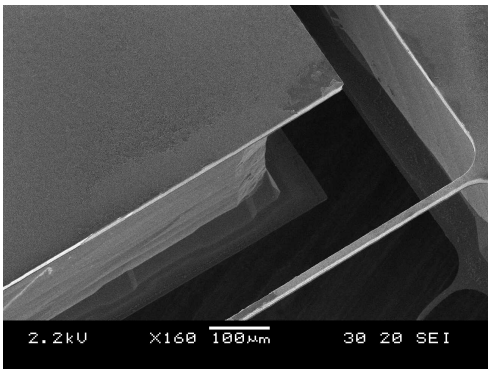

(c) *Proof mass underetch.*

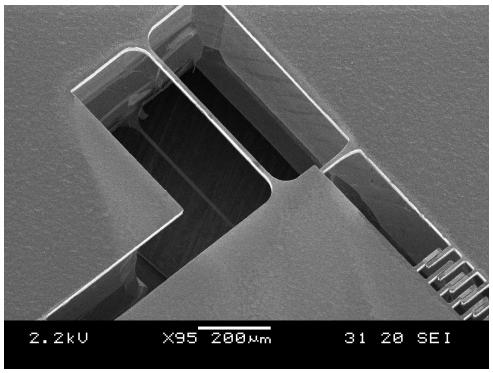

(d) *Beam, bump and fingers.*

Figure 6.4: *Devices after TMAH etching (top side).*

In figure 6.4a an overview of a released sensor is given. Although the fingers are not released by DRIE, the TMAH has enough etching time to release the finger structures for a small set of fingers. When the amount of fingers for a set increases, the required etch time for releasing them increases, causing the proof mass to reduce in size, which is not desired.

Looking carefully one can observe that the proof mass is indeed capable of moving, since the sensor is shifted a bit to the right. It is even a little bit twisted, since on the right hand side the fingers of the proof mass are moved over the fingers of the substrate. Note also that some beams at the bottom are broken/destroyed.

From figure 6.4b it appears that the beams are buckled a little, although this should not be the case according to theoretical analysis. Probably the sidewall coating is causing this, since SiO_2 by wet thermal oxidation of silicon contains a lot of tensile stress (about 300 MPa, see appendix A.1). When the coverage of SiO_2 is not uniform, buckling can be expected. A solution to remove this effect is to strip the coating, which is even necessary for wafer bonding. The underetching by TMAH of the proof mass and the substrate can be seen in figure 6.4c. Note that etching for 2 hours is sufficient, comparing the underetch of the proof mass and the thickness of a beam. The alignment of the lithography steps can be partly deduced from figure 6.4d, wherein both beams on top and at the bottom are present.

Although these results look promising, different results are observed when investigating the other side of the wafer. Two interesting images made using SEM of this side are given in figure 6.5.

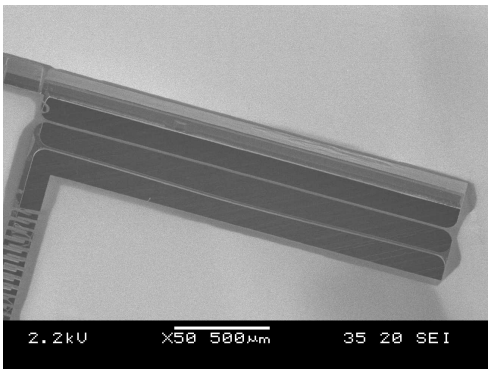

(a) *Bottom side beam is different from the top side beam.*

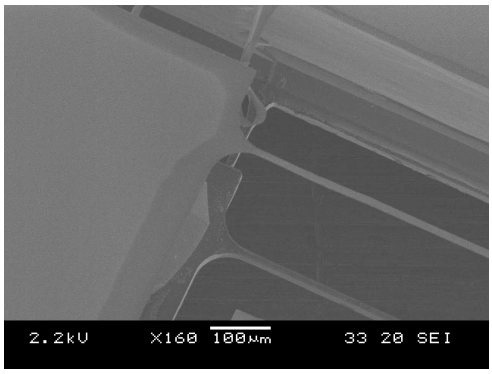

(b) *Undercut by TMAH visible.*

Figure 6.5: *Devices after TMAH etching (bottom side).*

Considering the overview of the beams at both the top and bottom side in figure 6.5a, it appears that the thickness of the beam at the top side differs from the one on the bottom side. It seems also that there is a small undercut present at the top side, regarding the difference in color at the edges of the substrate (i.e. the beams and fingers have a different color with respect to the large substrate around it). This effect can be seen more clearly in figure 6.5b, wherein the undercut of silicon by TMAH is well visible. However, from this figure can be induced that the beam on top is very thin with respect to the lower beam. Comparing this to the absence of silicon at the edges of the substrate, which seems to be the case due to the color difference, it is possible that on a certain way the sidewall coating failed at some point, allowing the TMAH to etch at undesired places. Using optical microscopy, the same problem is observed (figure 6.6).

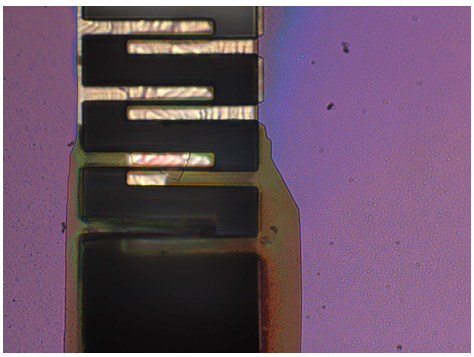

Figure 6.6: *Undesired etching by TMAH.*

In this figure the etching of silicon becomes visible at the finger structures, which should not be the case. Apparently the etchant is allowed to move in between the SiO_2 on top and the silicon of the beam. Since this is an undesired effect and will destroy the sensor, this problem needs to be investigated.

6.2.3 Sidewall coating

To determine whether the sidewall coating fails at certain points, this coating is investigated in more detail. First, two SEM images are given in figure 6.7, which are images of a test wafer (see section 6.1) after wafer-through etching by DRIE but before wet etching by TMAH.

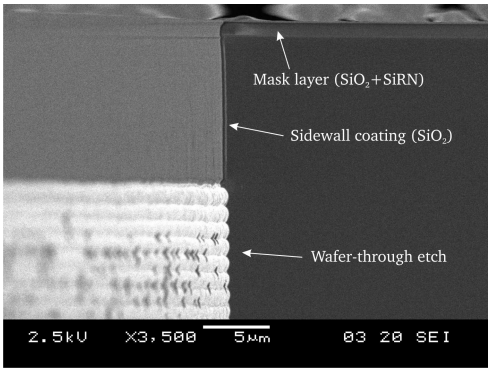

(a) *Good sidewall coating.*

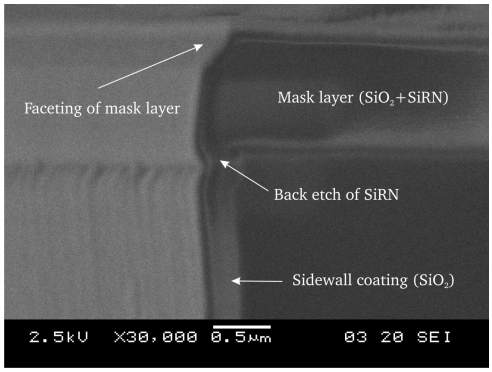

(b) *Good corner protection.*

Figure 6.7: *After wafer-through etching using DRIE.*

Regarding figure 6.7a the sidewall coating looks very good (see chapter 5). The mask layer of SiO_2 (with a small layer of SiRN beneath) is present with a thickness of at least 1 μm. The sidewall coating itself, consisting of SiO_2, is in agreement with the predictions by the process flow and shows good coverage. The scalloping below the sidewall coating is a result of the DRIE Bosch process. It becomes even more interesting when enlarging this image by means of figure 6.7b.

Again the mask layer and sidewall coating are clearly visible. The small notch by the backetch of SiRN can be also noticed, as is explained in chapter 5. Most important detail of this picture is the presence of a tapered profile at the corner. This tapered profile is known as faceting, which is a side-effect by directional etching, which causes sharp corners to become flattened under a certain angle (about 60 degree) with a higher etch rate than the average etch rate of the used process [2]. Faceting could also be the result of a problem with the mask layer, leading to larger facets during DRIE processes. When faceting is occurring too much, it could destroy the protection of the corner and allowing the TMAH to move in for undesired etching. Therefore, the sidewall coating, especially around the corner, needs to be further investigated.

6.2.4 Failure of corner protection

When the sidewall coating of a wafer with devices is investigated in more detail after wafer-through etching, the failure of the corner protection becomes clearly visible. Four images by SEM of this problem are given in figure 6.8.

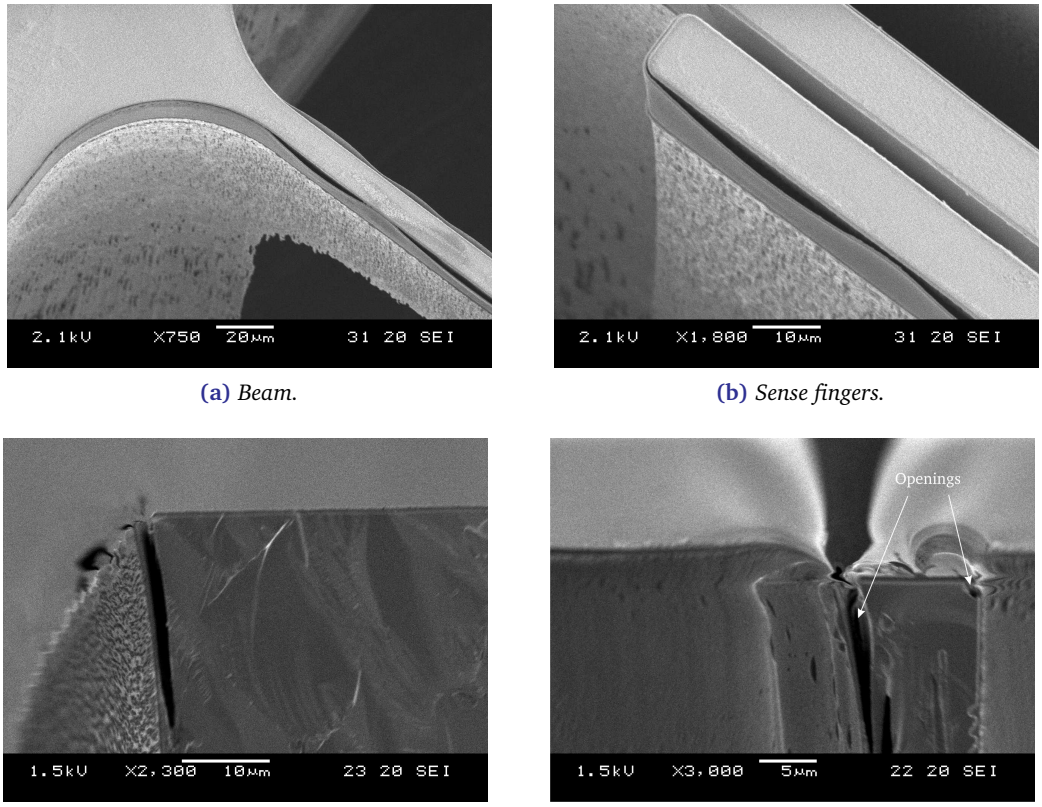

(a) *Beam.*

(b) *Sense fingers.*

(c) *Proof mass.*

(d) *Sense finger (left and right side).*

Figure 6.8: *Significant openings in the sidewall coating.*

In figure 6.8a the failure of the sidewall coating at a beam is illustrated well. The black small gaps between the silicon beam and the thin sidewall coating indicate that there are unwanted openings present. A similar problem is observed at the finger structures (figure 6.8b). Regarding a cross-sectional view of the sidewall coating of such a wafer, the effect is even better observed when looking at figure 6.8c. Here, a very thin but long gap is visible between the sidewall coating and the silicon, indicating that serious problems are present concerning protection of the sidewalls. Considering a finger structure, openings of the protection are also visible, but are not the same everywhere (figure 6.8d).

Since the openings are occurring at the corners of the structures, the protection at these corners deserves close attention. Therefore, some images by SEM are given in figure 6.9, for determining the shape and condition of the corners at different process steps in order to determine what is causing the problem.

Regarding the shape of the corner after sidewall coating by wet thermal oxidation and

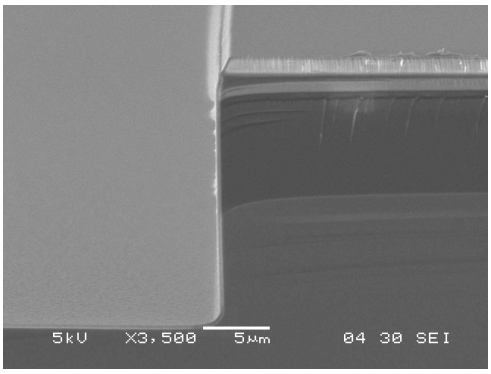

(a) *After sidewall coating.*

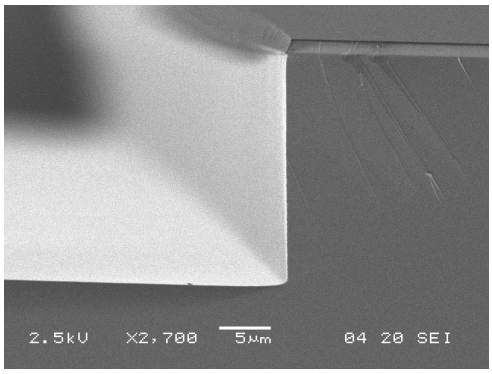

(b) *Before sidewall coating.*

Figure 6.9: *Faceting present with and without sidewall coating.*

TEOS by figure 6.9a, a facet in the corner is present. Although the protection of the corner is still intact, the protection is not as thick as it should be. To determine when this effect starts to occur, have a look at figure 6.9b. It seems that faceting of the corner already starts to occur before the sidewall coating is applied. Probably every DRIE step is increasing the size of the cornet facet, but it is important to determine where these facets starts, because once they are present, it is hard to remove them.

There are also examples available of corner protection failure during fabrication. In figure 6.10 an image by SEM is given wherein the corner is faceted too much, causing a little opening into the silicon below.

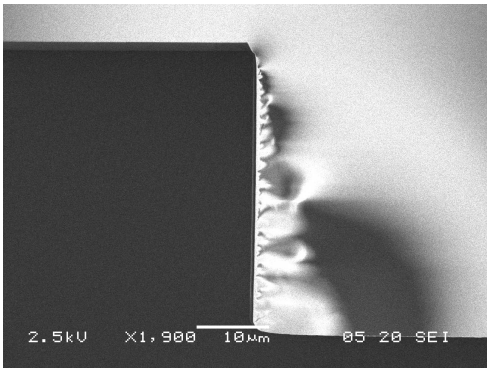

Figure 6.10: *Corner protection failed due to faceting.*

Since these images give rather more overview than detail, two close-ups are given in figure 6.11. In figure 6.11a the faceting effect with a measured angle of about 60 degree can be seen clearly, together with the small opening created into the silicon. One can imagine that during wafer-through etching this silicon will also starts to etch into the vertical direction, as is confirmed by the images from figure 6.8. In figure 6.11b it can be seen that the bottom removal was done properly.

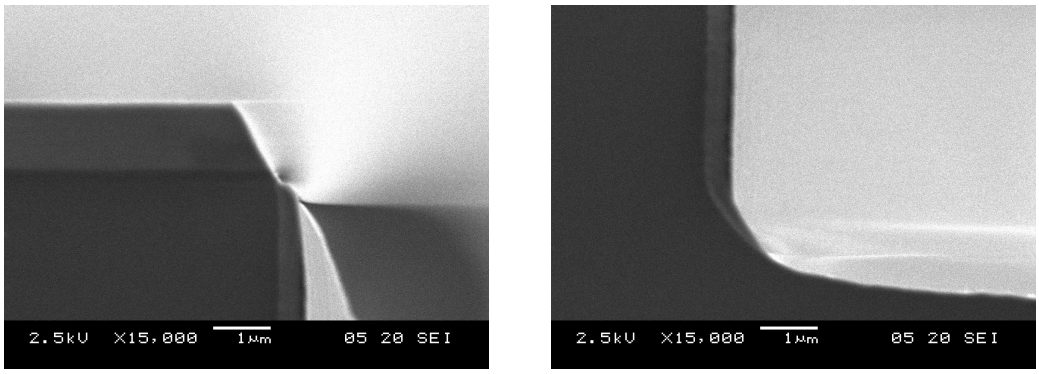

(a) *Small part not coated anymore.* **(b)** *Bottom is removed properly.*

Figure 6.11: *Close-up of corner protection failure by faceting.*

The problem with sidewall coating leading to corner protection failure is summarized schematically in figure 6.12. First, the faceting problem is already present before applying the sidewall coating (figures 6.12a and 6.12b). During the bottom removal the corner is also attacked and shows more faceting, as is depicted in figure 6.12c. During wafer-through etching by DRIE the corner protection starts to fail, allowing directional etching of silicon within the protected structures (figures 6.12d and 6.12e). Once these directional etches have occurred, the former protected silicon is removed during wet etching, regarding figure 6.12f.

6.2.5 Cause of tapered profile

To determine what is causing the tapered profile of the structures, testing several steps of the process flow of the silicon wafer is required. Since such tapered profile is often a result of faceting of photoresist during directional etching [2], the profile of the SU-8 photoresist before and after directional etching should be determined. Doing so, this lead to the results given in figure 6.13.

In figure 6.13a the SU-8 photoresist is showing a straight sidewall profile, which was expected [3]. Measuring the thickness of the SU-8 in the SEM image gives a thickness of about 4.8 μm. According to the used process and its details, this is a bit higher than the predicted 4.1 μm.

After directional etching for SiO_2 removal, the profile of SU-8 is changed, visible in figure 6.13b. Both the SU-8 photoresist and the SiO_2 layer (about 1 μm thick) below show faceting, since the sidewall profile is not vertical anymore, but shows an angle of about 80 degree. In addition, the thickness of the SU-8 has decreased to 3.7 μm, which is about 23% of its initial thickness. So, photoresist is removed, but there are apperently more mechanisms present than only faceting, since the visible angle is not equal to the typical faceting angle of 60 degree. It is possible that also the presence of a little bit SU-8 photoresist in the concave corners (corners of sidewall and bottom) and redeposition effects are contributing to the observed tapered profile.

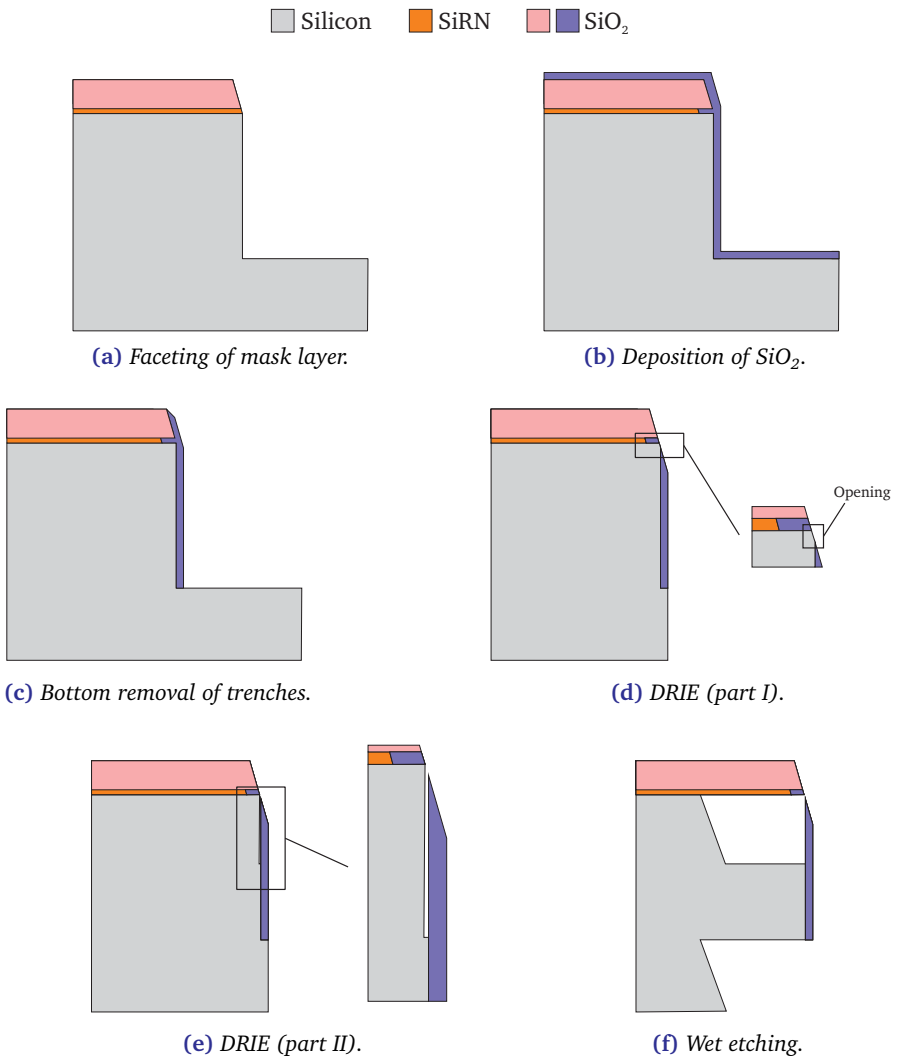

(a) *Faceting of mask layer.*

(b) *Deposition of SiO_2.*

(c) *Bottom removal of trenches.*

(d) *DRIE (part I).*

(e) *DRIE (part II).*

(f) *Wet etching.*

Figure 6.12: *Result when corner protection of sidewall coating fails.*

6.3 Discussion

Although the used process for fabrication of bulk micromachined accelerometers for geophysical applications looks promising and gives useful information, the process itself needs to be optimized. The sidewall coating fails under certain circumstances, leading to problems when releasing the structures using anisotropic wet etching.

From tests regarding the effect of directional etching on the mask quality, it appears that the chosen SU-8 photoresist is attacked significantly during such etch steps. The resulting tapered profile weakens the sidewall coating at the corners, leading eventually to failure of the protection mechanism. Therefore, the quality of the mask needs to be improved. A possible solution for improving the mask is using a chromium mask, since such a mask will not be eroded (thus tapered) by directional etching [4].

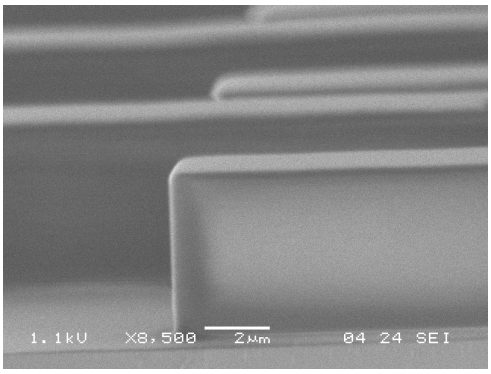

(a) *Before DRIE.*

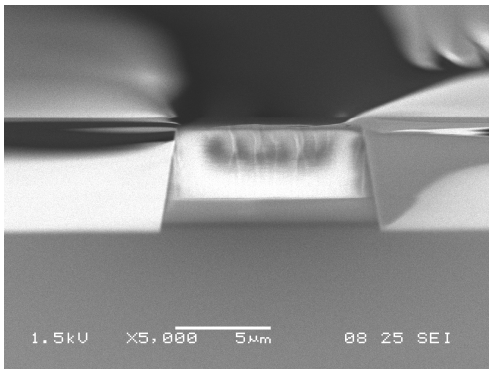

(b) *After DRIE.*

Figure 6.13: *Profile of SU-8 before and after DRIE.*

6.3.1 Reproducibility

Despite the encountered problems with sidewall protection, some statements can be given about reproducibility of the devices. Especially when these accelerometers are used for gravity gradient sensing, the sensors should be identical as much as possible. Small deviation in its mutual behavior will result in undesired measurement errors.

To achieve best uniformity of sensors, a set of sensors should be chosen from one specific wafer. During fabrication it appeared that especially the thickness of a beam might vary while processing several wafers. This causes a distribution in spring constant of the system in the total sensor yield, resulting in a variance of measured values.

6.3.2 Measurements

When the fabrication of the devices is optimized and working sensors for geophysical applications are realized, these need to be characterized by doing measurements. Although characterizing such a sensitive accelerometer is quite challenging, several measurement methods and associated setups are proposed in appendix D.

6.4 Conclusions

According to the results from fabrication of the bulk micromachined accelerometer for geophysical applications the proposed process and associated technology in principle works. However, the SiO_2 sidewall coating starts failing at several points, especially at the corners, leading to undesired TMAH wet anisotropic etching, which damages or destroys vital parts of the sensor.

The probable cause of the sidewall coating failure is faceting during directional etching. Before starting directional etching the SU-8 lithography shows a straight sidewall profile, but after (several steps of) etching it shows a tapered profile. Once this tapering is present, the coating of the corners becomes weakened, leading eventually to small unwanted open-

ings. To prevent this from happening, the mask layer (now SU-8) should be optimized in order to prevent it from eroding and leading to unwanted tapered profiles.

References

[1] H. Jansen, M. de Boer, R. Wiegerink, N. Tas, E. Smulders, C. Neagu, and M. Elwenspoek. "RIE lag in high aspect ratio trench etching of silicon". *Microelectronic Engineering*, **35**:45–50, 1997.

[2] M. J. Madou. *Fundamentals of Microfabrication*. CRC-Press, 1998.

[3] J. Liu, B. Cai, J. Zhu, G. Ding, X. Zhao, C. Yang, and D. Chen. "Process research of high aspect ratio microstructure using SU-8 resist". *Microsystem Technologies*, **10**:265–268, 2004.

[4] M. J. de Boer, R. W. Tjerkstra, J. W. Berenschot, H. V. Jansen, G. J. Burger, J. G. E. Gardeniers, M. Elwenspoek, and A. van den Berg. "Micromachining of Buried Micro Channels in Silicon". *Journal of Microelectromechanical Systems*, **9**(9):94–103, March 2000.

Chapter 7

Discussion

In this chapter conclusions are drawn and recommendations are given about the design and fabrication of the treated bulk micromachined accelerometer for geophysical applications. Although characterization of the fabricated sensor was not performed during this assignment, some recommendations about it are given.

7.1 Conclusions

During this research the possibilities for a bulk micromachined (MEMS) accelerometer for geophysical applications were investigated. Therefore, gravity itself was discussed and it is concluded that measuring either gravity or its gradient is very challenging, since gravitational effects are quite small (typically lower than 1:100.000 [1]) compared to gravity by earth itself (9.81 m/s^2).

Several techniques for gravity (gradient) measurements have been discussed. For gravity measurements commercial state-of-the-art measurement devices are available based upon a zero-length spring system, giving a resolution of about 1 μgal [2]. High performance (commercial) systems for measuring gravity gradient are based upon a torsion balance or a vibrating string, leading to measurement resolutions between 1–5 E [1, 3].

When a MEMS device can be designed and fabricated yielding comparable resolutions, this would be a break-through in miniaturization of gravity (gradient) measurement systems.

7.1.1 Design

Since measuring of gravitation effects is normally based upon the displacement of a proof mass [1], it is quite straightforward to realize a system in MEMS with a large proof mass, sensitive for very small (gravitational) accelerations. Therefore, a mass-spring system has been chosen with a very large proof mass, supported on every corner by very long and thin beams, allowing the proof mass to displace for very small accelerations. The design of the system is done is such a way that it is symmetric over three axes, making it more robust for fabrication and transportation and to give reliable behavior for applied accelerations.

The possibilities for such a design within a 4" silicon wafer are investigated using a theoretical approach. From this followed that restraints like buckling, maximum allowed stress and orientation dependence limit the performance of the sensor. To determine the optimum design of the accelerometer, a Figure of Merit has been defined. From this can be deduced which design will be a 'good' design.

Using this approach together with FEM simulations, some conclusions can be given about achieving of the requirements. Considering the measurement of gravity itself, a device with proper dimensions should be capable of measuring accelerations with a resolution of about 1 mgal. With very good read-out techniques and a 'critical' design someone might reach a resolution of several μgal. However, such a design will be on the edge of buckling and/or breaking, meaning it will not be very reliable.

Measuring gravity gradient using two accelerometers within one wafer, it will be very hard to deal with existing gravity gradient systems. Even using the most critical design (see chapter 4), it will be a challenge to measure a gradient of 10 E. Of course, increasing the baseline and taking two separate accelerometers (thus two separate wafers) increases the gradient resolution, but then the total system will not be a microsystem anymore.

Considering read-out mechanisms, it is convenient to use capacitive read-out techniques for MEMS accelerometers, capable of measuring small displacement and giving a electrical signal right away. It also allows the use of force feedback, to influence the performance of the sensor. To protect the sensor for extreme movements, a series of bumps was added.

7.1.2 Fabrication

Exploring available methods for fabricating an accelerometer with a very large proof mass, long and thin beams, and a three-axes symmetric design, lead to the use of bulk micromachining. Combining the use of a <111>-wafer and sidewall coating technology, it was possible to realize the proposed system from designing.

However, during fabrication some problems were encountered concerning the sidewall coating. It seemed that during processing some openings were created in the corners of the protected structures, allowing eventually the wet etchant to move in and etch the desired structures.

Although the protection of the sidewall coating failed at certain places and not all structures were released after fabrication, the chosen technology proved useful for creating a MEMS accelerometer for geophysical applications, since some devices survived and could move when applying random accelerations.

7.2 Recommendations

Although design and technology regarding the proposed accelerometer for geophysical applications are discussed, the yield of fabricated sensors is low and these sensors are not ready for testing and characterization. Therefore, some future works needs to be done and improvements have to be made and implemented.

7.2.1 Design

During fabrication was observed that some sensors were not released after wafer-through etching. It seems that the gap between sets of fingers are not large enough. Therefore, these gaps should be made larger in order to release all sensor structures.

Other improvements in the design should be made using the results obtained after packaging and characterization of the device. It is possible that important results will be obtained during fabrication of the whole packaged sensor and/or when performing measurements.

7.2.2 Fabrication

Since the sidewall coating of the devices is often damaged at the corners, the fabrication process needs to be optimized. Despite the straight sidewall profile of the SU-8, the transition on the bottom causes the sidewall coating to fail after directional etching eventually. Therefore, it is advised to apply a chromium mask, since chromium will not be attacked during directional etching. Note that a chromium mask can be created using a positive photoresist layer, requiring new (inverted) masks, since SU-8 is a negative photoresist.

In order to package the wafer, the glass process should be tested and eventually applied. Especially the bonding procedure needs to be investigated, to determine whether the sensor structures survive during (anodic) bonding and how well the bonds are established. It is also recommended to order and use a DSP <111>-wafer, to obtain a fully packaged sensor.

7.2.3 Characterization

When the sensor will be realized using the optimization steps described in the previous paragraphs, it needs to be characterized. Although there are some suggestions for characterization given in appendix D, characterization methods for accelerations smaller than 1 mgal need to be found, in order to determine whether the sensor is capable of measuring gravitational accelerations.

A similar problem is present concerning the response on gradients in gravity. Applying accelerations is described in appendix D, but applying gradients in accelerations is rather difficult. Therefore, some methods to realize this have to be found.

In case of a fully packaged and working sensor, the effect of force feedback should be determined on the sensor. In chapter 3 several types of feedback are described. It is interesting to investigate whether feedback improves the sensor performance and how it could be used for doing (more) accurate geophysical measurements.

References

[1] M. Nabighian, M. Anders, V. Grauch, R. Hansen, R. LaFehr, Y. Li, W. Pearson, J. Peirce, J. Phillips, and M. Ruder. “Historical development of the gravity method in exploration”. *Geophysics*, **70**(6):63–86, 2005. 75th Anniversary.

[2] J. van Popta and S. Adams. “Reprint of Gravity Gains Momentum”. Technical report, Micro-g LaCoste, 2008.

[3] H. Golden, W. McRae, and A. Veryaskin. “Description of and Results from a Novel Borehole Gravity Gradiometer”. In *ASEG*, Perth, Western Australia, 2007.

Appendix A

Process details

In this appendix details are given about the used process, making it possible to execute the described process in chapter 5 under the given conditions and with the appropriate information.

A.1 Device wafer (silicon)

Step	Process	
1	**Substrate selection – Silicon <111> OSP** (*#subsxxx*)	CR112B / Wafer Storage Cupboard Supplier: Okmetic Orientation: <111> Diameter: 100 mm Thickness: 525 μm $\pm$ 25 μm Polished: Single side Type: p
2	**Wafer thickness measurement** (*#char012*)	CR112B-1 / HeidenHahn
3	**Cleaning standard** (*#clean003*)	CR112B / Wet-bench 131 HNO_3 (100%) Selectiepur: MERCK HNO_3 (69%) VLSI: MERCK • Beaker 1: fumic HNO_3 (100%), 5 min • Beaker 2: fumic HNO_3 (100%), 5 min • Quick Dump Rinse < 0.1 μS • Beaker 3: boiling (95°C) HNO_3 (69%), 10 min • Quick Dump Rinse < 0.1 μS • Spin drying

Step	Process	
4	**LPCVD SiRN – low deposition rate** (*#depo002*)	CR125C / Tempress LPCVD new system 2007 Program: SiRN01/N2 Tube:G3 • Use 5–8 boat fillers in front and back of the boat to achieve specifications • SiH_2Cl_2 flow: 77.5 sccm • NH_3 flow: 20 sccm • Temperature: 820/850/870°C • Pressure: 150 mTorr • Deposition rate: ± 4 nm/min • N_f: ± 2.18 • Stress (range): 200–280 MPa • Boat position 12: 200 MPa (centre of the boat) • Boat position 1: 280 MPa (front of the boat) • Uniformity of the wafer: < 2% • Uniformity over the boat: (20 wafers): < 8% **Deposition time: 25 min**
5	**Ellipsometer measurement** (*#char007*)	CR118B / Plasmos Ellipsometer
6	**Cleaning standard** (*#clean003*)	CR112B / Wet-bench 131 HNO_3 (100%) Selectiepur: MERCK HNO_3 (69%) VLSI: MERCK • Beaker 1: fumic HNO_3 (100%), 5 min • Beaker 2: fumic HNO_3 (100%), 5 min • Quick Dump Rinse < 0.1 μS • Beaker 3: boiling (95°C) HNO_3 (69%), 10 min • Quick Dump Rinse < 0.1 μS • Spin drying
7	**LPCVD TEOS** (*#depo004*)	CR112B / Tempress LPCVD B4 Tube: B4-TEOS Bubbler: 40°C Temperature: 700°C Pressure: 400 mTorr • Program: TEOS05 • Deposition rate: 10.7 nm/min (25 wafers) • Uniformity/wafer: 3% • N_f: 1.44 • Stress after deposition: -5 MPa • Stress after two weeks: -20 MPa • Stress after anneal of 700°C: +5 MPa **Deposition time: 2 hr 30 min**

Step	Process	
8	**Ellipsometer measurement** (*#char007*)	CR118B / Plasmos Ellipsometer
9	**Cleaning standard** (*#clean003*)	CR112B / Wet-bench 131 HNO_3 (100%) Selectiepur: MERCK HNO_3 (69%) VLSI: MERCK • Beaker 1: fumic HNO_3 (100%), 5 min • Beaker 2: fumic HNO_3 (100%), 5 min • Quick Dump Rinse $< 0.1\ \mu S$ • Beaker 3: boiling (95°C) HNO_3 (69%), 10 min • Quick Dump Rinse $< 0.1\ \mu S$ • Spin drying
10	**Lithography – Dehydration bake SU-8 2005** (*#lith062*)	CR112B / Hotplate • Dehydration bake (120°C): 10 min
11	**Lithography – Coating SU-8 2005 (Delta 20)** (*#lith076*)	CR112B / SüssMicroTec Spinner Delta 20 Microchem NANO SU-8 2005 TST Bottle Contact: Meint/Jeroen Experimental results: 1 – 1000 rpm – 13.6 μm 2 – 1500 rpm – 8.4 μm 3 – 2000 rpm – 7.4 μm 4 – 2500 rpm – 6.0 μm 5 – 3000 rpm – 5.2 μm 6 – 3500 rpm – 4.6 μm 7 – 4000 rpm – 4.1 μm **Use program: 7 (4.1 μm)**
12	**Lithography – Softbake SU-8 2005** (*#lith077*)	CR112B or CR117B / Hotplate • 1 min @ 65°C • 2 min @ 95°C
13	**Lithography Alignment & Exposure SU-8 2005** (*#lith078*)	CR117B / EVG 620 Electronic Vision Group 620 Mask Aligner • Exposure time 10 sec • Hard contact
14	**Lithography Exposure Bake SU-8 2005** (*#lith079*)	CR112B or CR117B / Hotplate • Start @ 65°C • Ramp to 95°C • Cool down to 25°C • Time ca. 90 min

Step	Process	
15	**Lithography Development SU-8 2005** (*#lith080*)	CR102A / Wet-bench 9 TCO Spray Developer Developer: PGMEA (RER600, ARCH Chemicals • Time: 30 sec with spray gun, **5 cycles** • Time: 5 sec rinse with PGMEA bottle • Time: 5 sec rinse with IPA • Spin drying
16	**Optical microscopic inspection** (*#char002*)	CR112B / Nikon Microscope CR117B / Olympus Microscope CR102B / Olympus Microscope
17	**Lithography – Hard bake SU-8** (*#lith068*)	CR112B or CR117B / Hotplate • 2 hr @ 120°C
18	**Optical microscopic inspection** (*#char002*)	CR112B / Nikon Microscope CR117B / Olympus Microscope CR102B / Olympus Microscope
19	**Surface profile measurement** (*#char005*)	CR118B / Veeco Dektak 8
20	**Plasma etching of SiO_2 (and SiRN)** (*#etchrob*)	CR 125C / Adixen AMS 100 SE Program: TWIN3 + TESTROBERT • CHF_3: 100 sccm • Ar: 100 sccm • ICP: 1200 W • CCP: 150 W • Electrode: -40°C • Etch-rate: ± 250 nm/min **Etch-time: 6 min 30 sec**
21	**Plasma etching of Si C-Cryo-SF_6** (*#etch077*)	CR 125C / Adixen AMS 100 SE Program: C.CRYO500 • SF_6: 100 sccm • O_2: 10 sccm • ICP: 500 W • CCP (pulsed LF): 10 W • On/off: 20/80 (ms) • SH: 200 mm • APC: 100% • He: 10 mbar • Electrode: -100°C • Etch-rate: ± 2 μm/min **Etch-time: 15 min**

Step	Process	
22	**Cleaning "Piranha"** **H_2SO_4/H_2O_2** (*#clean008*)	CR112B / Wet-bench 130 H_2SO_4 (96%) VLSI: MERCK H_2O_2 (31%) VLSI: MERCK Only use dedicated wafer carriers and rod! H_2SO_4:H_2O_2 (3:1) vol% • Add H_2O_2 slowly(!) to H_2SO_4; be careful → exothermic process! • Adjust the hotplate temperature to 85°C, the temperature will increase to 130°C • Cleaning temperature: 130°C • Cleaning time 10–15 min • Quick Dump Rinse < 0.1 μS • Spin drying
23	**Lithography –** **Dehydration bake** **SU-8 2005** (*#lith062*)	CR112B / Hotplate • Dehydration bake (120°C): 10 min
24	**Lithography –** **Coating SU-8 2005** **(Delta 20)** (*#lith076*)	CR112B / SüssMicroTec Spinner Delta 20 Microchem NANO SU-8 2005 TST Bottle Contact: Meint/Jeroen Experimental results: 1 – 1000 rpm – 13.6 μm 2 – 1500 rpm – 8.4 μm 3 – 2000 rpm – 7.4 μm 4 – 2500 rpm – 6.0 μm 5 – 3000 rpm – 5.2 μm 6 – 3500 rpm – 4.6 μm 7 – 4000 rpm – 4.1 μm **Use program: 7 (4.1 μm)**
25	**Lithography –** **Softbake SU-8 2005** (*#lith077*)	CR112B or CR117B / Hotplate • 1 min @ 65°C • 2 min @ 95°C
26	**Lithography** **Alignment &** **Exposure SU-8 2005** (*#lith078*)	CR117B / EVG 620 Electronic Vision Group 620 Mask Aligner • Exposure time 10 sec • Hard contact
27	**Lithography** **Exposure Bake** **SU-8 2005** (*#lith079*)	CR112B or CR117B / Hotplate • Start @ 65°C • Ramp to 95°C • Cool down to 25°C • Time ca. 90 min

Step	Process	
28	**Lithography Development SU-8 2005** (*#lith080*)	CR102A / Wet-bench 9 TCO Spray Developer Developer: PGMEA (RER600, ARCH Chemicals • Time: 30 sec with spray gun, **5 cycles** • Time: 5 sec rinse with PGMEA bottle • Time: 5 sec rinse with IPA • Spin drying
29	**Optical microscopic inspection** (*#char002*)	CR112B / Nikon Microscope CR117B / Olympus Microscope CR102B / Olympus Microscope
30	**Lithography – Hard bake SU-8** (*#lith068*)	CR112B or CR117B / Hotplate • 2 hr @ 120°C
31	**Optical microscopic inspection** (*#char002*)	CR112B / Nikon Microscope CR117B / Olympus Microscope CR102B / Olympus Microscope
32	**Surface profile measurement** (*#char005*)	CR118B / Veeco Dektak 8
33	**Plasma etching of SiO_2 (and SiRN)** (*#etchrob*)	CR 125C / Adixen AMS 100 SE Program: TWIN3 + TESTROBERT • CHF_3: 100 sccm • Ar: 100 sccm • ICP: 1200 W • CCP: 150 W • Electrode: -40°C • Etch-rate: ± 250 nm/min **Etch-time: 6 min 30 sec**
34	**Plasma etching of Si C-Cryo-SF_6** (*#etch077*)	CR 125C / Adixen AMS 100 SE Program: C.CRYO500 • SF_6: 100 sccm • O_2: 10 sccm • ICP: 500 W • CCP (pulsed LF): 10 W • On/off: 20/80 (ms) • SH: 200 mm • APC: 100% • He: 10 mbar • Electrode: -100°C • Etch-rate: ± 2 μm/min **Etch-time: 15 min**

Step	Process	
35	**Cleaning "Piranha"** **H_2SO_4/H_2O_2** (*#clean008*)	CR112B / Wet-bench 130 H_2SO_4 (96%) VLSI: MERCK H_2O_2 (31%) VLSI: MERCK Only use dedicated wafer carriers and rod! H_2SO_4:H_2O_2 (3:1) vol% • Add H_2O_2 slowly(!) to H_2SO_4; be careful → exothermic process! • Adjust the hotplate temperature to 85°C, the temperature will increase to 130°C • Cleaning temperature: 130°C • Cleaning time 10–15 min • Quick Dump Rinse < 0.1 μS • Spin drying
36	**Etching HF (1%)** **Native Oxide** (*#etch027*)	CR112B / Wet-bench 3-3 HF (1%) VLSI: MERCK 112629.500 • Etch time: > 1 min • Quick Dump Rinse < 1 μS • Spin drying
37	**Etching of SiRN** **(Hot H_3PO_4)** (*#etch053*)	CR112B / Wet-bench 3-1 Hot H_3PO_4 85% Merck VLSI 1.00568.2500 Etch-rate: ± 4 nm/min High-selective for SiO_2 layers (±1:10) • Temperature: 180°C (caution!) • Quick Dump Rinse < 1 μS • Spin drying **Etch-time: 15 min**
38	**Cleaning standard** (*#clean003*)	CR112B / Wet-bench 131 HNO_3 (100%) Selectiepur: MERCK HNO_3 (69%) VLSI: MERCK • Beaker 1: fumic HNO_3 (100%), 5 min • Beaker 2: fumic HNO_3 (100%), 5 min • Quick Dump Rinse < 0.1 μS • Beaker 3: boiling (95°C) HNO_3 (69%), 10 min • Quick Dump Rinse < 0.1 μS • Spin drying

Step	Process	
39	**Wet Oxidation at 900°C of Silicon** (*#depo015*)	CR112B / Furnace B2 Standby temperature: 800°C Check water level of bubbler • Program: WET900 • Temperature: 900°C • Gas: $H_2O + N_2$ (Bubbler) **Deposition time: 10 min**
40	**LPCVD TEOS** (*#depo004*)	CR112B / Tempress LPCVD B4 Tube: B4-TEOS Bubbler: 40°C Temperature: 700°C Pressure: 400 mTorr • Program: TEOS05 • Deposition rate: 10.7 nm/min (25 wafers) • Uniformity/wafer: 3% • N_f: 1.44 • Stress after deposition: -5 MPa • Stress after two weeks: -20 MPa • Stress after anneal of 700°C: +5 MPa **Deposition time: 25 min**
41	**Ellipsometer measurement** (*#char007*)	CR118B / Plasmos Ellipsometer
42	**Plasma etching of SiO_2 (and SiRN)** (*#etchrob*)	CR 125C / Adixen AMS 100 SE Program: TWIN3 + TESTROBERT • CHF_3: 100 sccm • Ar: 100 sccm • ICP: 1200 W • CCP: 150 W • Electrode: -40°C • Etch-rate: ± 250 nm/min **Etch-time: 1 min 30 sec**

Step	Process	
43	**Plasma etching of Si** **A-pulsed-CHF_3** (*#etch077*)	CR125C / Adixen AMS 100 SE Program: A.PULSEDCHF3 • SF_6: 400 sccm • CHF_3: 200 sccm • ICP: 2500 W • CCP (pulsed LF): 20 W • On/off: 20/180 (ms) • SH: 110 mm • APC: 15% • He: 10 mbar • Electrode: -100°C • Etch-rate: ± 16 μm/min **Etch-time: 30 min (total)**
44	**Cleaning "Piranha"** **H_2SO_4/H_2O_2** (*#clean008*)	CR112B / Wet-bench 130 H_2SO_4 (96%) VLSI: MERCK H_2O_2 (31%) VLSI: MERCK Only use dedicated wafer carriers and rod! H_2SO_4:H_2O_2 (3:1) vol% • Add H_2O_2 slowly(!) to H_2SO_4; be careful → exothermic process! • Adjust the hotplate temperature to 85°C, the temperature will increase to 130°C • Cleaning temperature: 130°C • Cleaning time 10–15 min • Quick Dump Rinse < 0.1 μS • Spin drying
45	**Etching HF (1%)** **Native Oxide** (*#etch027*)	CR112B / Wet-bench 3-3 HF (1%) VLSI: MERCK 112629.500 • Etch time: > 1 min • Quick Dump Rinse < 1 μS • Spin drying
46	**Etching of Silicon by** **TMAH – Standard**	CR116B / Wet-bench 2 TMAH (25%): MERCK 8.14748.1000 Etch-rate: ± 60 nm/min • Temperature: 70°C • Stirrer • Rinse in beaker glass(es) with DI-water • Rinse in beaker with IPA • Dry (no spin-drying!) **Etch-time: 2 hr**

Step	Process	
47	**Optical microscopic inspection** (*#char002*)	CR112B / Nikon Microscope CR117B / Olympus Microscope CR102B / Olympus Microscope
48	**Etching HF (50%) user made** (*#etch030*)	CR116B / Wet-bench 2 HF (50%) VLSI: MERCK 100373.2500 • Temperature: 20°C • Rinse in beaker glass(es) with DI-water • Rinse in beaker with IPA • Dry (no spin-drying!) **Etch-time: 2 min**
49	**Optical microscopic inspection** (*#char002*)	CR112B / Nikon Microscope CR117B / Olympus Microscope CR102B / Olympus Microscope

A.2 Carrier wafer (silicon)

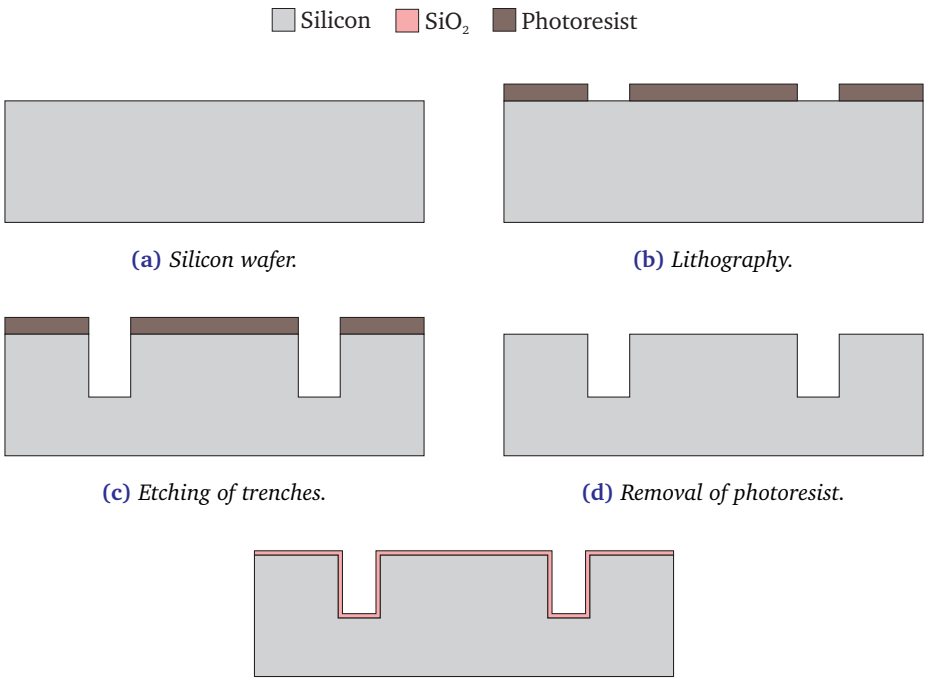

(a) *Silicon wafer.*

(b) *Lithography.*

(c) *Etching of trenches.*

(d) *Removal of photoresist.*

(e) *Thermal oxidation of silicon.*

Figure A.1: *Process flow for the carrier wafer.*

Step	Process	
1	**Substrate selection – Silicon <100> OSP** (*#subs001*)	CR112B / Wafer Storage Cupboard Supplier: Okmetic Orientation: <100> Diameter: 100 mm Thickness: 525 μm $\pm$ 25 μm Polished: Single side Type: p
2	**Wafer thickness measurement** (*#char012*)	CR112B-1 / HeidenHahn
3	**Cleaning standard** (*#clean003*)	CR112B / Wet-bench 131 HNO_3 (100%) Selectiepur: MERCK HNO_3 (69%) VLSI: MERCK • Beaker 1: fumic HNO_3 (100%), 5 min • Beaker 2: fumic HNO_3 (100%), 5 min • Quick Dump Rinse < 0.1 μS • Beaker 3: boiling (95°C) HNO_3 (69%), 10 min • Quick Dump Rinse < 0.1 μS • Spin drying
4	**Lithography – Priming (liquid)** (*#lith001*)	CR112B / SüssMicroTec Spinner Delta 20 Hotplate 120°C HexaMethylDiSilizane (HMDS) • Dehydration bake (120°C): 5 min • Spin program: 4 (4000 rpm, 20 sec)
5	**Lithography – Coating Olin 907-17** (*#lith005*)	CR112B / SüssMicroTec Spinner Delta 20 Hotplate 95°C Olin 907-17 • Spin program: 4 (4000 rpm, 20 sec, 1.7 μm) • Prebake (95°C): 90 sec
6	**Lithography – Alignment & Exposure Olin 907-17 (EV 620)** (*#lith021*)	CR117B / EV620 Electronic Vision Group 620 Mask Aligner • Hg-lamp: 12 W/cm^2 • Exposure time: 4 sec

Step	Process	
7	**Lithography – Development Olin Resist** (*#lith011)*	CR112B / Wet-bench 11 Developer: OPD4262 Hotplate 120°C (CR112B or CR117B) • After exposure bake (120°C): 60 sec • Time: 30 sec in beaker 1 • Time: 15–30 sec in beaker 2 • Quick Dump Rinse $< 0.1\ \mu S$ • Spin drying
8	**Lithography – Postbake 150°C** (*#lith010*)	CR112B Postbake for Cryogenic DRIE to avoid cracking of resist Hotplate 120°C • Time: 30 min Heraeus Convection Furnace • Temperature: 150°C • Time: > 15 min
9	**Plasma etching of Silicon – standard (Oxford)** (*#etch013*)	CR102A / Oxford Plasmalab 100ICP Structure width 20–200 μm, depth up to 150 μm Load: 10–50% • Temperature: -110°C • SF_6 flow: 120 sccm • O_2 flow: 0–10 sccm • CM pressure: 10 mTorr • ICP power: 600 W • He pressure: 20 mbar • Etch-rate: $\pm$ 2 μm/min **Etch-time: 20 min**
10	**Wet Oxidation at 900°C of Silicon** (*#depo015*)	CR112B / Furnace B2 Standby temperature: 800°C Check water level of bubbler • Program: WET900 • Temperature: 900°C • Gas: $H_2O + N_2$ (Bubbler) **Deposition time: 20 min**

A.3 Top wafer (glass)

Step	Process	
1	**Substrate selection – Borofloat BF33 – 500 μm** (*#subs014*)	CR112B Supplier: Schott Glas Diameter: 100.0 mm ± 0.3 mm Thickness: 0.5 mm ± 0.025 mm Roughness: < 1.0 nm Surface: DSP
2	**Wafer thickness measurement** (*#char012*)	CR112B-1 / HeidenHahn
3	**Lithography – Lamination of BF405 foil** (*#lith033*)	HO7143 / GBC 3500Pro Laminator Ordyl BF405 dry resist foil • Temperature: 130°C ('Carry' preset) • Speed: 2 ('Carry' preset)
4	**Lithography – Alignment and Exposure BF 405** (*#lith044*)	CR 117B/EVG 620 Electronic Vision Group 620 Mask Aligner • Hg-lamp: 12 W/cm^2 • Exposure time: 20 sec (BF 405)
5	**Lithography – Development BF405 foil** (*#lith037*)	HO7143 / HCM Spray Developer Na_2CO_3: MERCK 1.06392.0500 Na_2CO_3:H_2O = 15 g : 7.5 L (+ 1 cup Antifoam) • Temperature: 32°C • Time: 2 min • Rinsing • Spin drying Due to non-uniform development turn sample by 180° after half the time – small features might need longer development time

Step	Process	
6	**Powderblasting of Glass – High resolution** (*#etch022*)	HO10156 / Powderblaster For feature size > 30 μm • Particles: 9 μm Al_2O_3 • Pressure: 4.6 bar • Massflow: 3-12 g/min • Etch-rate appr. 29 μm per g/cm^2
7	**Stripping of BF 405** (*#lith039*)	HO7143 Stripping BF 405 foil and removal of Al_2O_3 particles Na_2CO_3 p.a. Aceton: technical IPA VLSI: MERCK 107038 • For BF 33 glass substrates strip foil in Na_2CO_3 solution, the foil will delaminate after 15 min • Beaker 1: Aceton, > 30 min , ultrasonic (removal of Al_2O_3 particles) • Beaker 2: Isopropanol > 30min, ultrasonic (removal of Al_2O_3 particles) • Beaker 3: DI water > 10min, ultrasonic (removal of Al_2O_3 particles) • Rinse • Spin drying
8	**Lithography – Lamination of BF405 foil** (*#lith033*)	HO7143 / GBC 3500Pro Laminator Ordyl BF405 dry resist foil • Temperature: 130°C ('Carry' preset) • Speed: 2 ('Carry' preset)
9	**Lithography – Alignment and Exposure BF 405** (*#lith044*)	CR 117B/EVG 620 Electronic Vision Group 620 Mask Aligner • Hg-lamp: 12 W/cm^2 • Exposure time: 20 sec (BF 405)
10	**Lithography – Development BF405 foil** (*#lith037*)	HO7143 / HCM Spray Developer Na_2CO_3: MERCK 1.06392.0500 Na_2CO_3:H_2O = 15 g : 7.5 L (+ 1 cup Antifoam) • Temperature: 32°C • Time: 2 min • Rinsing • Spin drying Due to non-uniform development turn sample by 180° after half the time – small features might need longer development time

Step	Process	
11	**Powderblasting of Glass – High resolution** (*#etch022*)	HO10156 / Powderblaster For feature size > 30 μm • Particles: 9 μm Al_2O_3 • Pressure: 4.6 bar • Massflow: 3-12 g/min • Etch-rate appr. 29 μm per g/cm^2
12	**Stripping of BF 405** (*#lith039*)	HO7143 Stripping BF 405 foil and removal of Al_2O_3 particles Na_2CO_3 p.a. Aceton: technical IPA VLSI: MERCK 107038 • For BF 33 glass substrates strip foil in Na_2CO_3 solution, the foil will delaminate after 15 min • Beaker 1: Aceton, > 30 min , ultrasonic (removal of Al_2O_3 particles) • Beaker 2: Isopropanol > 30min, ultrasonic (removal of Al_2O_3 particles) • Beaker 3: DI water > 10min, ultrasonic (removal of Al_2O_3 particles) • Rinse • Spin drying

A.4 Wafer bonding

Step	Process	
1	**Cleaning standard** (*#clean003*)	CR112B / Wet-bench 131 HNO_3 (100%) Selectiepur: MERCK HNO_3 (69%) VLSI: MERCK • Beaker 1: fumic HNO_3 (100%), 5 min • Beaker 2: fumic HNO_3 (100%), 5 min • Quick Dump Rinse $< 0.1\ \mu S$ • Beaker 3: boiling (95°C) HNO_3 (69%), 10 min • Quick Dump Rinse $< 0.1\ \mu S$ • Spin drying
2	**Cleaning Glass** (*#clean005*)	CR112B / Wet-bench 133 HNO_3 (100%) Selectiepur: MERCK • Beaker 1: HNO_3 (100%), 5 min • Beaker 2: HNO_3 (100%), 5 min • Quick Dump Rinse $< 0.1\ \mu S$ • Quick Dump Rinse $< 0.1\ \mu S$ • Spin drying
3	**EV501 Anodic bonding** (*#bond005*)	CR112B/EVG EV501 Bond tool Electronic Visions Group EV501 Bond tool • Temperature: 400°C • Vacuum: better then 10^{-1} mbar • High voltage: 1000 Volt • Pressure: 300 N • Total process time: 2 hours • First wafer: Silicon • Second wafer: Borofloat glass • Alignment can be done with EV620 maskaligner

Appendix B

Spring stiffening

Although in chapter 3 a brief description was given about the spring stiffening effect of the sensor for relative large accelerations, this effect and its consequences are investigated a bit more in detail.

B.1 Proof mass displacement

Although one might think according to figure 3.8 the system is limited when the proof mass is displaced over a distance equal to the width of the beam, it is possible for the proof mass to move even further. The displacement of the proof mass can be related to the gravitational acceleration g by equating the gravitational force F_g to the spring force F_{tot} (see equation 3.41).

$$F_g = mg = F_{tot} = \frac{3nE\delta(20I + \delta^2 A)}{5L^3(1-\nu^2)} \tag{B.1}$$

Visualizing this relation in figure B.1, the movement of the proof mass is not limited by its displacements, but it needs relative more force/acceleration to at a certain point to obtain the same displacement.

B.2 Sensitivity

Although the movement of the proof mass is limited by finger structures for electrical capacitive read-out and is generally smaller than the thickness of a beam and thus neglecting the effect of spring stiffening, a so-called sensitive area of the sensor can be defined when assuming that the sensor can move into the area of spring stiffening. For example, when someone would use optical read-out, capacitive finger structures (and bumps) are not necessary anymore and the mass can deflect about several times the beam width.

Therefore, it is interesting to define the sensitivity S of the system, where F_{tot} is defined in equation B.1.

$$S = \frac{d\delta}{dg} = \frac{1}{m}\frac{d\delta}{dF_{tot}} \tag{B.2}$$

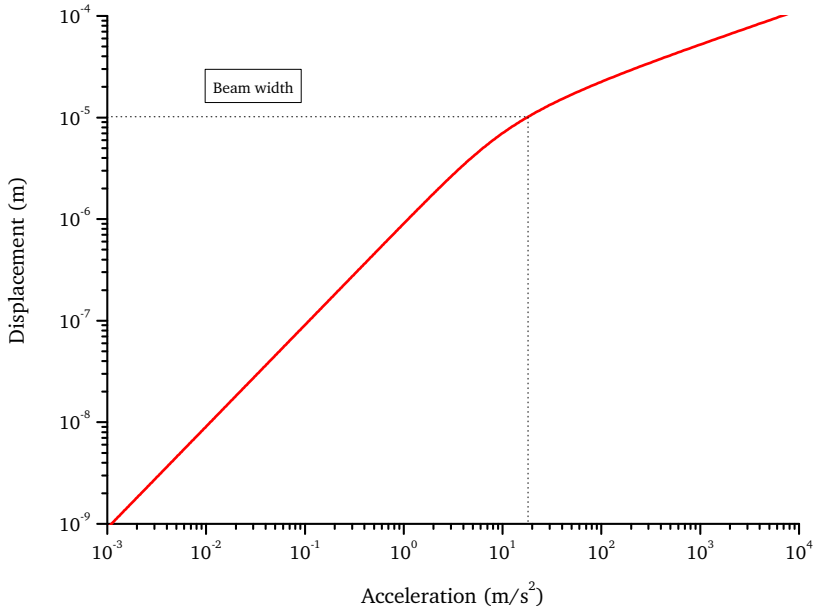

Figure B.1: *Displacement of the proof mass versus the applied acceleration.*

Graphing the sensitivity S for a range of applied gravitational accelerations g in figure B.2, a so-called working range for the sensor can be determined, due to the effect of spring stiffening, since in that case the spring will become stiffer and sensitivity S is reduced.

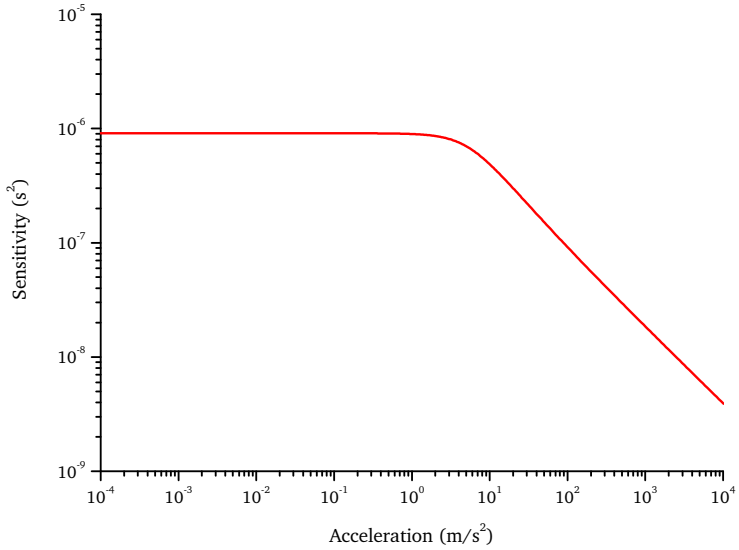

Figure B.2: *Sensitivity of the sensor for applied accelerations.*

Appendix C

Voltage to force conversion

A basic description and first order approximation about the voltage to force conversion using a changing gap configuration were already given in chapter 3. However, it is interesting to extend this for large movements of the proof mass with respect to its initial position.

C.1 Capacitive forces using changing gap

Before investigating the voltage to force conversion in more detail, the capacitors with a changing gap configuration are given (again) in figure C.1.

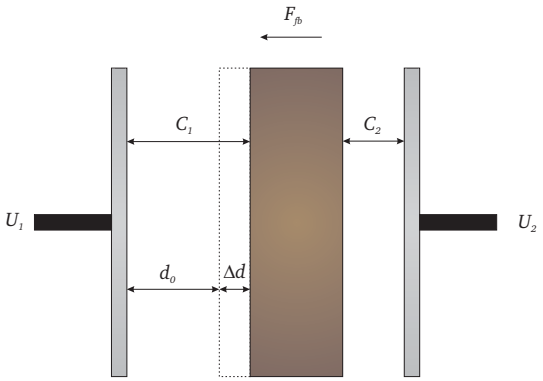

Figure C.1: *Electrostatic force-feedback by changing gap.*

From equation 3.136 (repeated below) can be seen that the (feedback) force depends on both the displacement d_Δ of the proof mass and the feedback voltage U_b.

$$F_{fb} = F_1 - F_2 = -\frac{1}{2}\frac{\epsilon A(U_b - U_f)^2}{(d_0 - d_\Delta)^2} + \frac{1}{2}\frac{\epsilon A(U_b + U_f)^2}{(d_0 + d_\Delta)^2} \tag{C.1}$$

To protect the system from pull-in (collapse of the plates) a series of bumps are prevent the mass from extreme movements. Suppose the position of this bump d_{bmp} is a factor R of

the gap d_0 by

$$d_{bmp} = Rd_0 \qquad 0 < R < 1 \tag{C.2}$$

From this a relation can be found for the total feedback force F_{fb} when the proof mass is displaced over a distance d_{bmp}.

$$F_{fb} = \frac{1}{2}\frac{\epsilon A(U_b - U_f)^2}{(d_0 - Rd_0)^2} - \frac{1}{2}\frac{\epsilon A(U_b + U_f)^2}{(d_0 + Rd_0)^2} \tag{C.3}$$

When the feedback force for displacements between the initial position of the proof mass and the position of the bumps are investigated, it turns out that the rate of feedback (i.e. the value of the feedback voltage) determines whether the feedback will work or not. This is illustrated by the graph in figure C.2.

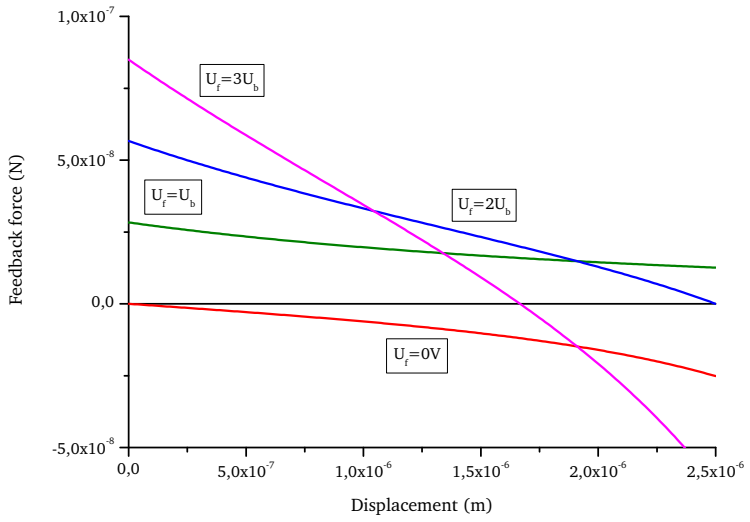

Figure C.2: *Feedback force with respect to the position of the proof mass.*

In this figure can be seen that for only a bias voltage the feedback force is zero at the initial position, but is 'helping' the mass to move to the plates in case of a gravitational acceleration in that direction. Not surprising, because this is known as spring softening under a bias voltage, which has already been seen in section 3.5.

When the feedback voltage U_f is increased to the bias voltage U_b, the feedback force is working in the opposite direction, causing the mass to move back. However, when the feedback voltage is too large, the force becomes non-linear and eventually negative (again) when the mass is near the bump. In this (undesired) case, the mass will never move back to its initial position. Note that in this consideration arbitrary values are used for explaining this aspect. A similar case exists for varying the bias voltage U_b, whereby a too high bias voltage U_b can also lead to pull-in near the bump, which is explained by Beeby et al. [1].

The feedback force F_{fb} at the bump-position can also be investigated with respect to the feedback voltage U_b. Doing so, the associated graph results in figure C.3.

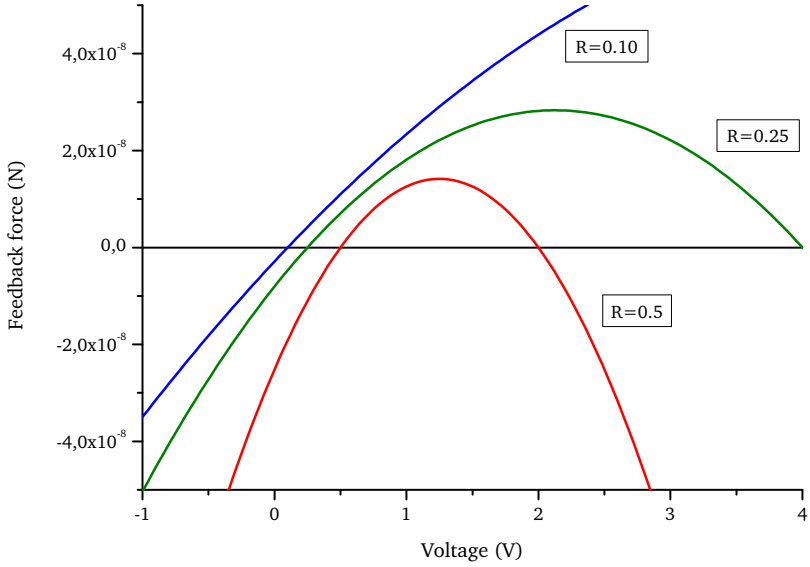

Figure C.3: *Feedback force versus voltage at the limitation of the displacement.*

From this figure should be determined that the value of R determines the width of the voltage band for U_b which can be used for appropriate feedback in case when the proof mass is situated around the bump. Using equation C.3, the voltages $U_{f,1}$ and $U_{f,2}$ can be calculated which form the edges of the voltage band (calculate when the feedback force becomes equal to zero).

$$U_{f,1} = \frac{U_b}{R} \quad \vee \quad U_{f,2} = RU_b \tag{C.4}$$

Using these values for the voltages, the resulting voltage band ΔU_f is given by

$$\Delta U_f = U_{f,1} - U_{f,2} = U_b \left(1 - \frac{d_{bmp}}{d_0}\right) \tag{C.5}$$

So, increasing the distance d_{bmp} of the bump with respect to the initial position, the smaller the voltage band ΔU_f for moving the proof mass back to the center for large displacements.

C.2 Forces by capacitive read-out

In section 3.5 the effects of spring softening by capacitive read-out were considered. However, as can be seen in figure C.3 for a feedback voltage U_b of 0 Volt, the first order approximation for the resulting force by capacitive read-out is only valid around the initial position (d_Δ=0) of the proof mass. Taking a similar approach as described in the previous section, one can calculate the force at the maximum displacement d_{bmp} of the proof mass when

there are bumps present for preventing extreme movements. This force F_m can be deduced from equation C.3 under the given conditions, leading to

$$F_m = \frac{1}{2}\frac{\epsilon A u_m^2}{(d_0 - R d_0)^2} - \frac{1}{2}\frac{\epsilon A u_m^2}{(d_0 + R d_0)^2} = \frac{2\epsilon A u_m^2 R}{d_0^2(1-R)^2(1+R)^2} \tag{C.6}$$

where u_m is the (amplitude) of the modulation voltage and R is the ratio between the distance to the bump d_{bmp} and the distance to one of the plates d_0 with respect to the initial position of the proof mass.

Since the mass should always return to its initial position when there are no gravitational accelerations present, the force by the spring F_k (see chapter 3) should always be larger than the modulation force F_m.

$$F_m < F_k \tag{C.7}$$

where

$$F_m = \frac{2\epsilon A u_m^2 R}{d_0^2(1-R)^2(1+R)^2} \qquad F_k = \frac{12nEIRd_0}{L^3(1-\nu^2)} \tag{C.8}$$

Here, E is the Young's modulus of silicon, I is the moment of inertia of a beam, L is the length of a beam and ν is Poisson's ratio. From this equation a restraint can be found for the amplitude of the applied harmonic voltage V_m, which is given below.

$$V_m < \sqrt{\frac{12nEIRd_0^3(R^2-1)^2}{\epsilon AL^3(1-\nu^2)}} = \left(1-R^2\right)\sqrt{\frac{Kd_0^3}{\epsilon A}} \qquad 0 < R < 1 \tag{C.9}$$

Comparing this to the result found in chapter 3 and given below by $V_{m,0}$, it seems that the position of the bump determines the maximum amplitude for the modulation voltage V_m. This seems reasonable, because for small movements R goes to zero and the expression becomes equal to the one by a first order approximation (equation C.10).

$$V_{m,0} < \sqrt{\frac{Kd_0^3}{\epsilon A}} \tag{C.10}$$

References

[1] S. Beeby, G. Ensell, M. Kraft, and N. White. *MEMS Mechanical Sensors*. Artech House, Norwood, 2004.

Appendix D

Characterization

To investigate whether the sensor behaves as expected and if the theoretical analysis and simulated information by ANSYS^{TM} 11 is valid, several sensor properties need to be determined. In this appendix a few methods are proposed for characterizing this accelerometer for geophysical applications.

D.1 Dynamic response

Although the proposed accelerometer is designed for accelerations with a low frequency, it is interesting to determine the dynamical response of the sensor. From such experiments the resonance frequencies of the three described modes can be determined and these can be compared to the calculated and simulated values. It is also possible to calculate the spring constant K from it, since the resonance frequency ω_r is (already) measured and the mass m can be determined by using the density of silicon and measuring the dimensions of the proof mass, as given by

$$K = m\omega_r^2 \tag{D.1}$$

From chapter 3 three modes were found for the proposed accelerometer, namely translation in both x- and y-direction and rotation in the xy-plane. The third mode is more difficult to measure and is also not important for measurements, since gravity (gradient) is only considering in cartesian coordinates (x, y and z). Therefore, the first and second mode should be characterized. This can be done when the sensor is mounted either in horizontal or vertical mode, as given in figure D.1.

D.1.1 Mode 2 – Translation in y-direction

For a dynamic response of the sensor in y-direction (*out-of-plane* movement) a chirp signal can be applied to a piezo-element mounted onto the substrate of the sensor. Measuring the difference in vibration between the substrate and the proof mass, the harmonic response of the sensor can be determined. These kind of measurements can be performed using the Polytec MSA-400 Micro System Analyzer (available at floor 7 within the Hogekamp building at the University of Twente), whereat the sensor can be mounted both in horizontal mode and vertical mode (see figure D.1).

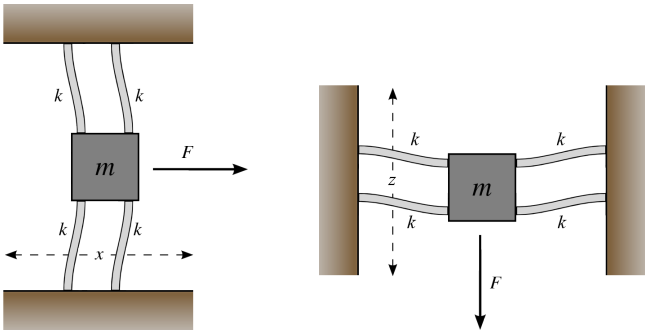

(a) *Horizontal mode.* **(b)** *Vertical mode.*

Figure D.1: *Orientation of the sensor during characterization.*

Although the vertical mode is most easy for doing measurements, the proof mass is however subjected to earth's gravity. Especially for weak springs this might cause to perform measurements on a so-called spring-stiffened sensor, giving false results when using it to characterize for measuring small gravitational accelerations into the x- and y-direction. Therefore, performing these measurements in horizontal mode is recommended. Since *Scanning Laser-Doppler Vibrometry* is used for determining the dynamic behavior of the system and this laser beam is projected in the z-direction, a mirror construction is necessary to achieve a successful measurement.

Note that such measurements are based on *out-of-plane* movement, meaning only the second mode (translation in y-direction) of the system can be characterized using this method.

D.1.2 Mode 1 – Translation in x-direction

To determine the first mode (*in-plane* movement), which is the base of the design, a packaged sensor with electrical connections can be required. Using feedback fingers it is possible to actuate the sensor in x-direction, and using sense fingers the position of the proof mass can be determined. Note that the transfer function of both electrical input and output should be as constant as possible, because otherwise the measurements are giving wrong results.

Another possibility for finding the dynamic response of the sensor in x-direction is to use *Stroboscopic Video Microscopy* by the Polytec MSA-400 Micro System Analyzer, making it possible to perform *in-plane* measurements. Using imaging and comparing images the displacement of the proof mass can be determined. Again, this requires a piezo-element to move the entire wafer into the x-direction, applied with a chirp signal from the measurement system.

Adding to this, using the data obtained by finding the second mode (y-direction), the spring constant K_y in that direction can be calculated and the resonance frequency in the x-direction ω_r can be estimated using the approximation from equation 3.76.

D.2 Static deflection

A possibility to determine the spring constant K_x of the sensor in the x-direction is to use the expression for bending of a clamped-clamped beam, found in chapter 3 and given below.

$$\delta(x) = \frac{P_b x^2(3L-2x)(1-\nu^2)}{12nEI} \qquad P_b = mg \qquad I = \frac{tw^3}{12} \tag{D.2}$$

Here, P_b is the applied force, L is the length of the beam, ν is Poisson's ratio, E is the Young's modulus for silicon, t is the thickness of the beam, w is the width of the beam, m is the mass size and g is the applied gravitational acceleration. When mounting the sensor in horizontal mode (see figure D.1), making it possible to measure in the direction of earth's gravity, it is possible to determine the spring constant K by defining

$$\delta(x) = \frac{mgx^2(3L-2x)}{K} \qquad K = \frac{12nEI}{L^3(1-\nu^2)} \tag{D.3}$$

Since earth's gravity g is known (9.81 m/s^2), the length L can be measured, the mass m can be measured by using the density of silicon and measuring the dimensions of the proof mass, and the deformation of the entire beam can be measured optically, it is possible to calculate the associated spring constant K.

$$K = \frac{mgx^2(3L-2x)}{\delta(x)} \tag{D.4}$$

Although a dynamic response shows also the spring constant without the need for knowing all parameters except the size of the proof mass m, static deflection allows a relative simple measurement setup. Using the Polytec MSA-400 Micro System Analyzer it is possible to determine the surface topography $\delta(x)$ by *White Light Interferometry*.

D.3 Sensitivity

Despite the expected interesting results from dynamical response and static deflection, most important characteristic of the sensor is the sensitivity. Therefore, the displacement of the proof mass has to be measured given a range of applied accelerations. Such accelerations can be applied using a piezo-element or equivalent actuator combined with a calibrated accelerometer, since it is important to know for reference which acceleration is applied to the system.

Using the techniques described in the previous sections this method should work for moderate accelerations of the accelerometer. However, when small accelerations are applied, it will be difficult to measure the appropriate displacement of the proof mass, as is explained in the next section.

D.3.1 Environmental noise

Since the designed accelerometer is quite sensitive for accelerations, it is challenging to determine which small accelerations can be measured. An important limitation when characterizing the device in the Hogekamp building at the University of Twente is the seismic

noise of the building. Because of the wind and other aspects the building is moving at a lot of frequencies, causing an undesired environmental noise.

This noise has been investigated a couple of years ago and is described in [1]. From these measurements it turns out that measuring on the place where these measurements are carried out seismic noise is larger than the thermal noise floor of the designed sensor (see chapter 4). Since most sensors will have a resonance frequency larger than 10 Hz, the environmental noise is between 1–10 mgal/$\sqrt{\text{Hz}}$. When a sensor is fabricated using a lower resonance frequency, the environmental noise is showing 1/f noise behavior, increasing to more than 10 mgal/$\sqrt{\text{Hz}}$.

Therefore, using the Polytec MSA-400 Micro System Analyzer at floor 7 within the Hogekamp building at the University of Twente, it will be very hard to characterize the sensor for accelerations below 10 mgal (measuring noise by building movement). This means that other measurement techniques need to be investigated to determine the sensor behavior for very small accelerations.

D.4 In the field

To get an idea about the capabilities of the sensor when it is operating in the so-called field, meaning that no accelerations are applied using a piezo-element or an equivalent actuator, the effect of a test mass and tidal effects are described briefly.

D.4.1 Test mass

In chapter 3 Newton's law of universal gravitation was given. Since the proposed sensor should eventually measure these kind of accelerations, it is interesting to calculate the gravitational acceleration g_m when a certain test mass is used.

$$g_m = G\frac{m}{r^2} \tag{D.5}$$

For instance, one could use a test mass of 1 kg (sugar) and place it on a distance of 8 cm from the sensor. From the expression above this will result in a gravitational acceleration of about 1 μgal. Therefore, using a test mass it will be very difficult to notice its gravitational effect. Even with state-of-the-art gravimeters it is almost impossible to measure such accelerations, since best resolutions are about 1 μgal.

D.4.2 Tidal effects

Instead of using a small test mass one could decide to look at the tidal effects, caused by the sun and moon. According to [2], tidal forces by moon and sun are in the order of 0.2 mgal. Although these gravitational accelerations are quite static (orbit related) and below 1 mgal, it should be possible to measure them. Especially when measuring for several weeks, one should be able to determine the orbits of the moon and earth.

References

[1] A. de Simone. "Design and Realization of a Setup for Mechanical Tests on a MEMS-based Micro Gravity-Gradiometer". Master's thesis, Delft University of Technology, 2008.

[2] A. Wolf. "Tidal Force Observations". *Geophysics*, **V**:317–320, 1940.

Index